Imperial College London

Molecular Functionalisation of Nanocrystalline Mesoporous Metal Oxide Films

Xiaoe Li

Department of Chemistry

Imperial College London

Submitted for the Degree of Doctor of Philosophy

March 2012

Except where specific reference is made, the material contained in this thesis is the result of my own work. This dissertation has not been submitted in whole or in part for a degree at this or any other university, and does not exceed 100,000 words in length.

X. Li

March 2012

Acknowledgements

I have to admit that it was very hard for me to make the decision to do a PhD. I would not be here writing my thesis without the support from all the people I have met here at Imperial who worked/works in James' and Brian's group.

Big thanks to my supervisors, Prof. James Durrant, Prof. Ramon Vilar and Dr. Brian O'Regan, for their thorough guidance, encouragement and excellent support during my PhD study. In particular, I would like to thank James for giving me this opportunity to do a PhD.

I am very grateful to Dr. Piers Barnes who has had such a profound effect on improving my work including the derivation of model used in hole percolation and insightful discussion in iodine binding studies. Special thanks to Dr. Emilio Palomares for his help on cation sensing, Dr. Ana Peiro for her help on metal oxide synthesis and Dr. Nélida Gimeno for her help on anion sensing. Also thanks to Dr. Tracey Clark and Dr. Rui Guo for their help on DFT calculation. Thanks to Dr. Saif Haque for his helpful discussion on optical sensing and to Dr. Yeni Astuti for her help on spectroelectrochemistry. Also thanks Jasper, Andrea L. and Andrea M., Anna R. and Ana M., Steph, Sara, Alice, Joe, Florent, Pedro, John, Alex and Tracy for providing a pleasant working atmosphere. Many thanks to people in JD group, BOR group, SH group and JDeM group for making my life at Imperial enjoyable.

Thanks to Prof. Muku Thelakkat at Bayreuth University, Germany for providing me HW456 dye and Dr. Md. K. Nazeeruddin at EPFL, Switzerland for N621 dye. Financial support from the Fluming funding (Imperial College London), EU project HETEROMOLMAT, EPSRC Materials for Energy and the EU Robust DSC project are gratefully acknowledged.

Finally, I am deeply thankful to my parents for all their support and encouragement they have given me, and would like to thank my husband Hongbin Wang and my son Ziyue Wang for their support and understanding.

Abstract

Mesoporous, nanocrystalline, metal oxide films exhibit a broad range of attributes attractive for technological applications, including high surface area, semiconducting behaviour, optical transparency in the visible region of the electromagnetic spectrum and excellent mechanical properties. They can be functionalised by the attachment of metal complexes and organic molecules to the metal oxide surface through ligating groups such as carboxylic acids. This thesis addresses the interaction of such functionalised metal oxide films with redox species and ions in solution for applications including dye-sensitised solar cells (DSSCs) and heterogeneous sensing and scavenging of pollutants.

The first study reported in this thesis employs a thiourea based organic molecule to functionalise a mesoporous Al_2O_3 film, and demonstrates that this functionalised film can be used as a heterogeneous colorimetric cyanide sensor in aqueous solution. This strategy is extended to a series of ruthenium based metal complexes which are employed to functionalise mesoporous TiO_2 films. These functionalised films are shown to bind mercury ions, enabling them to function as selective mercury scavengers. This mercury binding is also shown to disrupt lateral cation percolation between adjacent dye molecules. Electrochemical studies are employed to analyse this cation percolation in detail for two different transition metal complexes, with the introduction of a secondary acceptor group shown to result in an order of magnitude increase in the kinetics of cation percolation. The cation percolation results are discussed in relation to their importance in dye-sensitized solar cells. The last two results' chapters of this thesis address the interaction of functionalised mesoporous metal oxide films and iodine in solution, and the importance of this interaction for the function of dye-sensitised solar cells. Based upon these studies, an enhancement of cell performance is expected through modification of dye structure and the electrolyte composition.

Contents

List of Figures

Abbreviations

BET	Brunau-Emmett-Teller (BET) measurement
CV	Cyclic voltammetry
CVA	Cyclic voltabsorptometry
DCVA	Derivative cyclic voltabsorptometry
DSSC	Dye-sensitised solar cell
FTO	Fluorine doped Tin Oxide
HOMO	Highest Occupied Molecular Orbital
ICP-AES	Inductively Coupled Plasma-Atomic Emission Spectroscopy
LOD	Limit of detection
LUMO	Lowest Unoccupied Molecular Orbital
MCL	Maximum Contaminant Level
MLCT	Metal to Ligand Charge Transfer
ppm	part per million
ppb	part per billion
PZC	Point of Zero Charge
SEM	Scanning Electron Microscope
SMM	Scavenging molecular materials
TBAP	Tetrabutylammonium perchlorate
XRD	X-ray powder diffraction

Key to dye nomenclature used in this thesis

Compound 1 azo-phenyl thiourea compound

N621 *cis*-di(thiocyanato)(2,2′-bipyridyl-4,4′-dicatboxylic acid)-(2,2′-bipyridyl-4,4′-tridecyl) ruthenium(II)

HW456 *cis*-di(thiocyanato)(2,2′-bipyridyl-4,4′-dicarboxylic acid)-(2,2′-bipyridyl-4,4′-bis(vinyltriphenylamine) ruthenium(II)

N719 *cis*-di(isothiocyanato)-bis-(2,2’-bipyridyl-4,4’-dicarboxylato)-ruthenium(II) bis(tetrabutylammonium)

AR24 cis-di(isothiocyanato)(2,2’-bipyridyl-4,4’-dicarboxylato)-(5-amino-1,10-phenantroline) ruthenium(II)

C101 NaRu(4,4’-bis(5-hexylthiophen-2-yl)-2,2’-bipyridine)(4-carboxylic acid-4’-carboxylate-2,2′-bipyridine)$(NCS)_2$

Z995 (2,2’-bipyridyl-4,4’-dicarboxylato)-di(2,2’-bipyridyl-4,4’-dimethyl) ruthenium(II)

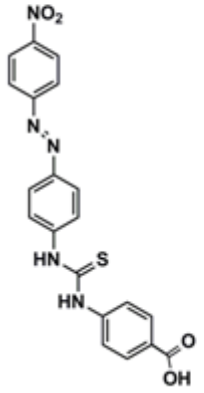

Compound **1**

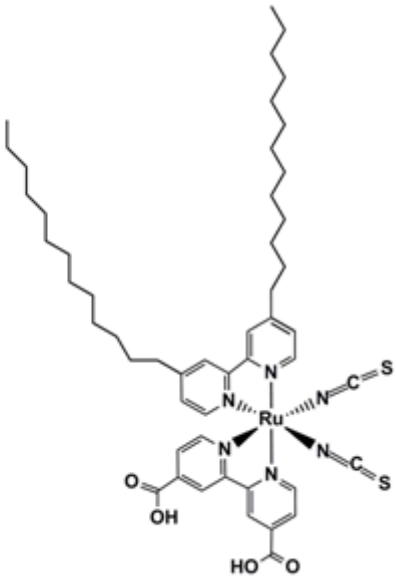

N621

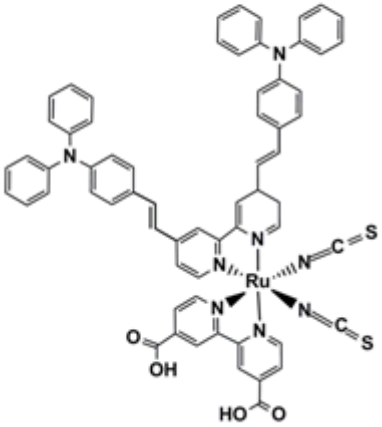

HW456

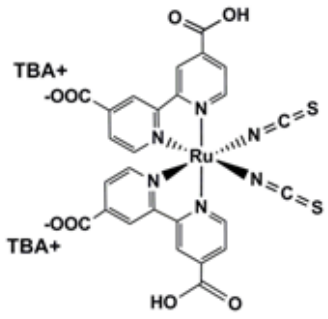

N719

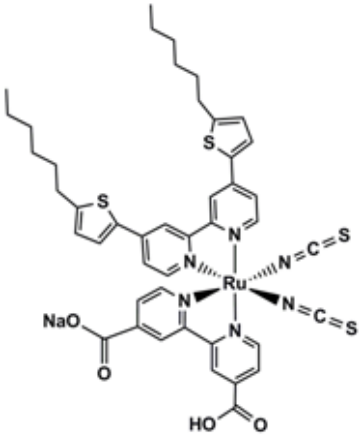

C101

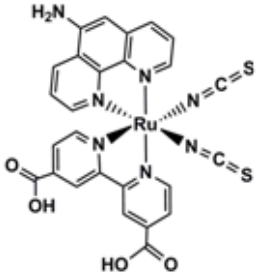

AR24

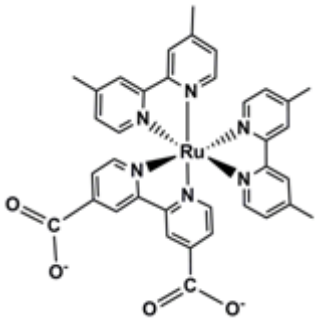

Z995

Chapter 1 Introduction

1.1 Motivation

World energy consumption is increasing. At present, approximately 80% of the energy consumed is provided by the burning of fossil fuels such as coal, gas and oil. However, these fuels are non-renewable and their combustion is causing an increase in carbon dioxide concentrations in the atmosphere, potentially leading to global warming and climate change. In addition, coal-burning can produce toxic heavy metals which pollute groundwater and contaminate soil.[1] These contaminants can directly affect plant and animal life, and then eventually enter the human food chain. This has a detrimental effect on public human health and ecosystems, causing diseases such as cancers and neuropsychiatric disorder. To address these problems, one solution is to increase the use of solar energy. This abundant, renewable and clean source of energy has the potential to reduce substantially our dependence upon fossil fuels. Meanwhile, current existing pollution could be monitored by sensing toxic pollutants, and strategies could be found to remove these pollutants from the natural environment. Strikingly, functionalised nanocrystalline, mesoporous metal oxide films have shown capabilities to address both of these issues.

Nanocrystalline, mesoporous metal oxide films can be fabricated with well-defined nanostructures and display excellent thermal and chemical stability. They possess a number of useful properties including semiconducting behaviour, ease of processing on a large scale, low production cost, non-toxicity, high surface area (a 10 μm thick titania (TiO_2) film may have a geometric-to-inner surface area ratio of 1:1000), high porosity (≥50 %), optical transparency in the visible region of the electromagnetic spectrum ($\lambda > 400$ nm) and can exhibit excellent mechanical properties.

The function of mesoporous metal oxide films can be substantially enhanced by the adsorption of molecular species to their surface. Such molecular functionalisation of nanocrystalline, mesoporous metal oxide films has been employed for applications including photovoltaic devices (e.g dye-sensitised solar cells),[2] light emitting

diodes)[2,3], electrochromic displays[4], chemical and biological sensors[5,6], heterogeneous photocatalysts for the degradation of organic pollutants and water splitting[7,8], and light-driven oxygen scavenging[9]. This thesis focuses upon the interaction of such functionalised metal oxide films with a range of analytes in solution, including mercury ions, cyanide and iodine, and the relevance of these interactions to applications including the sensing and scavenging of environmental pollutants and dye sensitized solar cells.

1.2 Background

1.2.1 Nanocrystalline, mesoporous metal oxide films

Nanocrystalline, mesoporous metal oxide films fabricated from oxides such as TiO_2, ZnO, SnO_2, ZrO_2 and Al_2O_3 have been extensively studied over the past two decades. These films are typically fabricated by either doctor-blading or screen-printing of nanoparticle colloidal solutions, which are synthesised by sol-gel process, on solid substrates such as transparent conducting oxide coated glass. The resulting films are mesoporous with pore sizes typically in the range of 10-50 nm and high surface area (> 100 m^2/g).

Due to their wide band gaps, shown in **Figure 1-1**, such metal oxide films are optically transparent (non-absorbing for wavelengths > 400 nm) and electrically semiconducting – insulating for applied potentials within bandgap but conductive at potentials above the conduction band edge. As such, these films can be used as insulating or semiconducting support substrates for studying the interaction between molecular species in solution (analytes) and receptor molecules attached to the metal oxide surface.

The fabrication of metal oxide nanoparticles influences their surface properties. The coordination number of surface oxygens is less than that within the solid. This results in the formation of surface hydroxyl groups.[10] A typical surface structure of TiO_2

films is shown in **Figure 1-2**. The point of zero charge (PZC), which defines the pH of the medium where the surface charge becomes zero, indicates the surface acidity, *i.e.*, the surface charge is positive for pH < PZC and negative for pH > PZC. Its value can vary for the same material synthesised by different synthetic methods, which form different crystal structures and particle morphologies, following different heat treatments. Typical PZC are 5.5 for TiO_2 and 9.2 for Al_2O_3.[11]

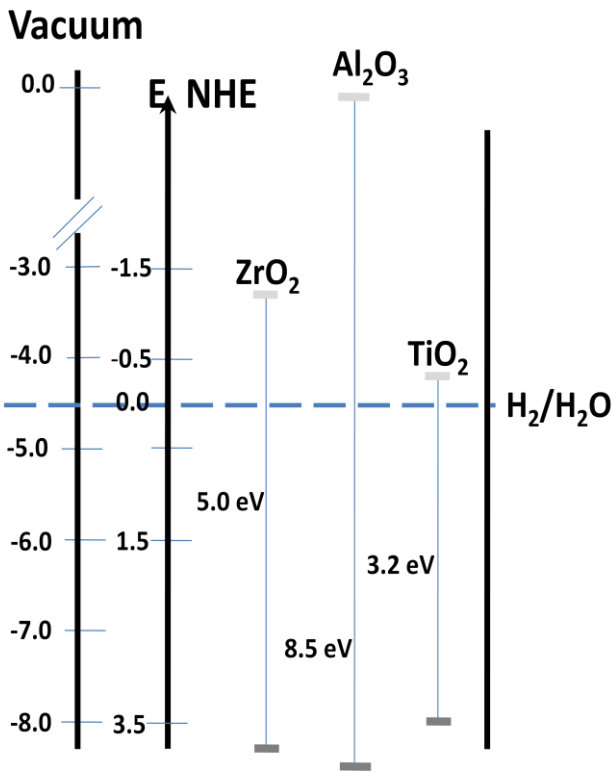

Figure 1-1. Band edge positions of several semiconductors employed in this study in contact with aqueous electrolyte at pH1. Reproduced from reference[3].

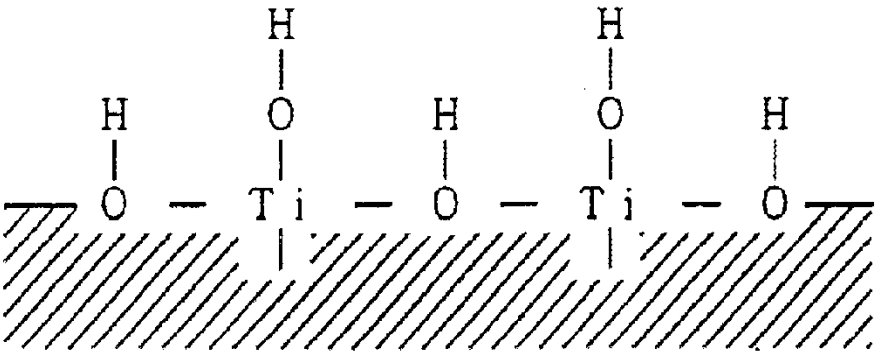

Figure 1-2. The schematic structure of TiO_2 showing strained Ti-O-Ti bonds with surface hydroxyl groups. Reproduced from reference[10].

Conventional supporting materials employed in adsorption technologies, such as activated carbon (amorphous), although exhibiting high surface area (e.g.: ~500 m^2/g), are often limited by bottlenecks and dead volumes in closed pores that can prevent the diffusion of ions and large molecules[12], and exhibit poor optical transparency. As such, they are not suitable for the functionalisation strategies addressed in this thesis. In contrast, nanocrystalline, mesoporous metal oxide films often exhibit nanopores (diameters between 2~100 nm) which are open, well-structured and thus show a fast diffusion of ions and small molecules between the pores and external solution[13]. As is shown herein, this is important in applications such as heterogeneous catalysis and sensing.

Of the metal oxides listed, sol-gel fabricated n-type nanocrystalline, mesoporous TiO_2 is of particular interest in DSSCs because of its higher stability (than ZnO) and slower recombination (than SnO_2). Among the three crystallographic structures of TiO_2: rutile, anatase and brookite, the anatase phase of TiO_2 film is widely used for applications in photocatalysis[9] and dye-sensitised solar cells (DSSCs)[3]. Anatase n-type TiO_2 is effectively insulating when the Fermi level is within the bandgap between the TiO_2 conduction and valence band edges (corresponding to -0.1V and + 3.1V versus normal hydrogen electrode (NHE) in aqueous electrolyte at pH 1, see in **Figure 1-1**[14], and -0.9V and 2.3V versus ferrocene/ferrocenium in tetrabutylammonium perchlorate (TBAP) in acetonitrile solution measured in chapter 5, respectively). Such TiO_2 film provides a high surface area compared to a flat TiO_2 film and its roughness factor η, defined as the ratio of the effective surface area of the nanocrystalline, mesoporous film to its projected area (1 cm^2 in this case), is estimated to be typically 450 for films studied in this thesis (film thickness is *ca.* 4 μm). Such high surface area enables the film to adsorb a large amount of dye molecules that enhances the light harvesting and thus increases the photocurrent in the external circuit in DSSC.

1.2.2 Functionalisation of nanocrystalline, mesoporous metal oxide films

Nanocrystalline, mesoporous metal oxide films can be functionalised with molecular species including dyes or molecular receptors. Such molecular species have included metal complexes and organic compounds, such as ruthenium dyes, fullerenes and aromatic amines, and biomolecules including redox proteins[6]. Examples include dyes which are employed only for light harvesting in dye-sensitised solar cells[15], organic molecules for electron transport[16,17], or molecular receptors which display molecular recognition properties to bind cations or anions in chemical sensing or/and scavenging[5,18]. Some of the dyes also have receptor ligands. The molecular species that have been studied in this project are either metal-based dyes or molecular receptors for anionic species based on organic molecules.

The structure of these dyes and molecular receptors used in this project can be considered sensitizer/molecular receptor – bridge - anchor arrays (**Figure 1-3**). They are bound to the surface of metal oxide nanoparticles through the linker (bridge (b) + anchoring group (A)).

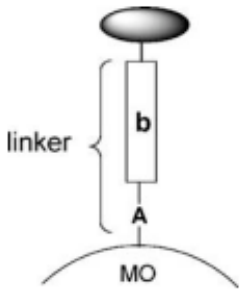

Figure 1-3. Schematic representation of linkers (bridge (b) + anchoring group (A)) used to attach molecular receptors to the surface of metal oxide (MO) nanoparticle. Reproduced from reference[19].

The most commonly used anchoring groups are carboxylic acids (-COOH), phosphonic acids ($-P(O)(OH)_2$), hydroxyl (-OH) and amino ($-NH_2$) groups.[15,20,21] Monolayers of these dyes molecules can be assembled via the ionization of the anchoring groups in solution followed by formation of covalent bonds to the surface

active sites of the metal oxide by reacting with surface hydroxyl groups. For example, carboxylic acid head-groups attach tightly to the TiO_2 by chelating Ti^{4+} sites at the TiO_2 surface through a variety of possible attaching modes as shown in **Scheme 1-1**. Mostly, the two accepted modes are a bidentate chelating or a bidentate bridging type linkage.[15]

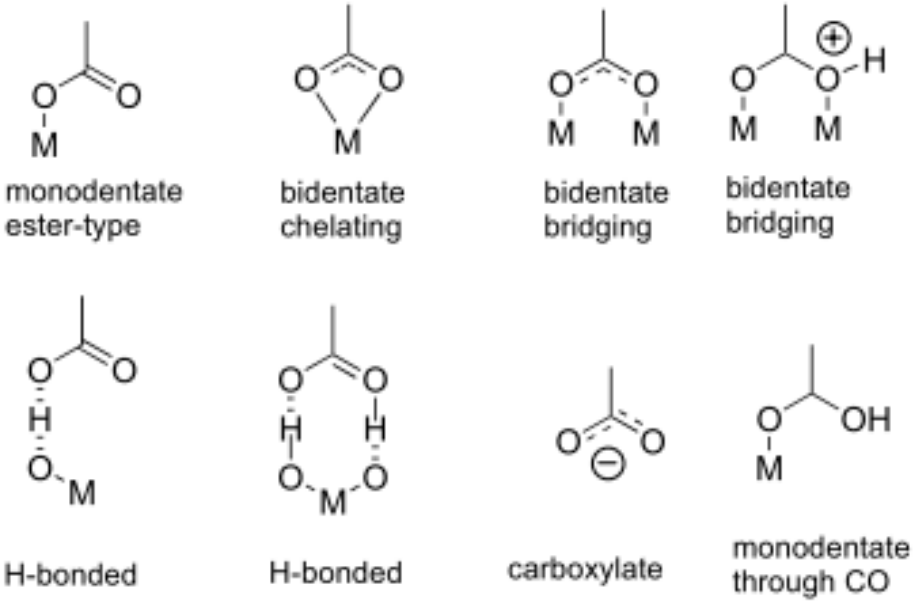

Scheme 1-1. Possible modes of carboxylic acid head-groups attach to metal oxide film. Reproduced from reference[19].

1.2.3 Applications of functionalised metal oxide films

1.2.3.1 Dye-sensitised solar cell (DSSC)

The most established application of functionalised nanocrystalline TiO_2 films is in dye-sensitised solar cells (DSSC) (**Figure 1-4**). DSSCs have been considered to be one of the most promising new solar cell technologies due to their potential advantages of low cost materials, ease of manufacturing in ambient conditions and reasonably high efficiencies[22]. Efficient DSSC was first reported in 1991[2], and are now undergoing extensive commercial development (including companies such as G24i and Tata in the UK) utilizing roll-to-roll processing, and could be used in energy deficient but sunlight rich countries.

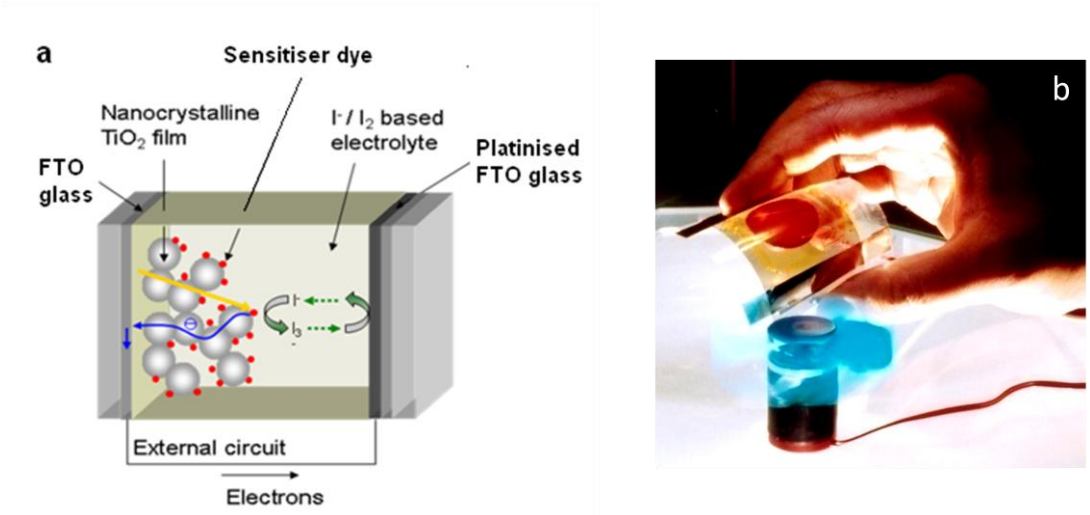

Figure 1-4. (a) Typical dye-sensitised solar cell (DSSC) in a sandwich structure. It employs dye sensitized TiO_2 films on FTO glass substrates used as the working electrode, platinised FTO glass as the counter electrode, and an electrolyte containing the iodine/iodide redox couple. The photoexcitation of a sensitiser dye, results in the injection of an electron into the conduction band of the TiO_2, generating the dye cation that is regenerated by iodide in the electrolyte. Reproduced from reference[23]. **(b)** A picture of demo fan driven by a flexible DSSC employing dye/TiO_2 films on conducting plastic as the working electrode and sputtered Pt on conducting plastic as the counter electrode. Reproduced from reference[24].

1. Background

Since the pioneering study by O'Regan and Gratzel in 1991, approximately 13,281 scientific papers and patents have been published and registered on DSSCs so far (February 23rd, 2012; source: web of science). These studies have mainly focused on the optimisation of working electrodes, new dye syntheses, new stable redox-couple syntheses and the development of new types of substrates for flexible DSSCs. To date, the most widely studied dye-sensitised solar cells employ a ruthenium dye called 'N719' (*cis*-bis(isothiocyanato)bis-(2,2'-bipyridyl-4,4'-dicarboxylato)-ruthenium(II) bis-tetrabutylammonium) to sensitise a mesoporous TiO_2 film and iodine/iodide redox couple, showing high stability and yielding an optimum cell efficiency of ~11.2%.[25]

2. Materials commonly used in DSSC

Dyes commonly used in DSSC. DSSCs are available in a range of colours from red to blue employing different colour dyes such as ruthenium complexes[26,27],

porphyrins[28], phthalocyanines[29], coumarin[30], tetrahydroquinoline dyes[31] and indoline dyes[32].. These dye molecules are bound to the metal oxide to form a donor–acceptor system, in which the dye molecule is the electron donor and the acceptor is the metal oxide. The design of dye structure should consider: a) increasing the distance between the donor and acceptor to reduce the recombination; b) preventing dye aggregation by using rigid linkers with large footprints such as phosphonic acids or introducing long alkyl chain; c) controlling the dye orientation on metal oxide surface by tuning the dye ligands. The best cell performance in DSSC's is achieved with ruthenium complexes of polypyridines dyes, such as N719. These dyes strongly absorb light in the visible region (λ_{max}=530~540 nm, ε~14,000 $M^{-1}cm^{-1}$), show fast electron injection and little aggregation. In addition, their photophysical and electrochemical properties can be finely tuned by varying the metals (e.g. Cu replaces Ru) and the ligands (e.g. replacement of alkyl chain with triphenylamine).

Electrolytes in typical DSSCs. The optimised electrolyte used in DSSCs is typically prepared by adding the iodine/iodide redox couple and other salts such as 4-*tert*-butylpyridine (tBP) and guanidinium thiocyanate (GuSCN) in either organic solvent such as acetonitrile[33] or water[34]. It is often assumed that this electrolyte is a mixture of all the components and the intermolecular complexations between these components can be neglected (**Scheme 1-2**). However, in reality, there are complex interactions between dye/TiO_2 surface and electrolyte components that will impact upon device performance, as will be discussed further in Chapters 6 and 7 in this thesis.

3. Working principle

The function of DSSC has been the subject of several recent reviews.[22,35,36] **Figure 1-5** shows an energy level diagram of a typical DSSC. The sensitizer dye in its ground state absorbs sunlight, generating an excited state, with the dye cation being generated by the injection of an electron into the conduction band of the metal oxide (normally TiO_2). The dye cation is subsequently regenerated by electron donation from the electrolyte (e.g. iodide) back to dye ground state, forming triiodide. Triiodide diffuses to the counter electrode and is reduced to iodide. Key loss pathways include

the recombination of electrons in the TiO_2 conduction band with either dye cation or iodine/triiodide in the electrolyte.

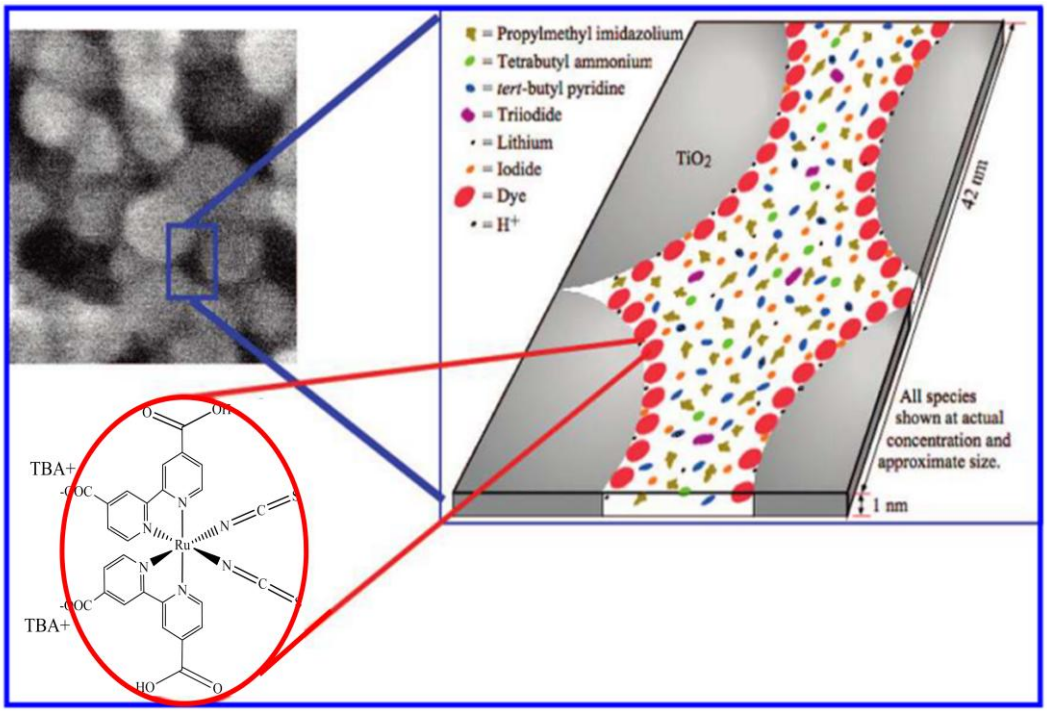

Scheme 1-2. Schematic of the Chemical Composition of a Typical Pore in a Complete DSSC Filled with Redox Electrolyte. Also shown are a HRSEM image of such a pore and the molecular structure of the N719 sensitizer dye. Reproduced from reference[37].

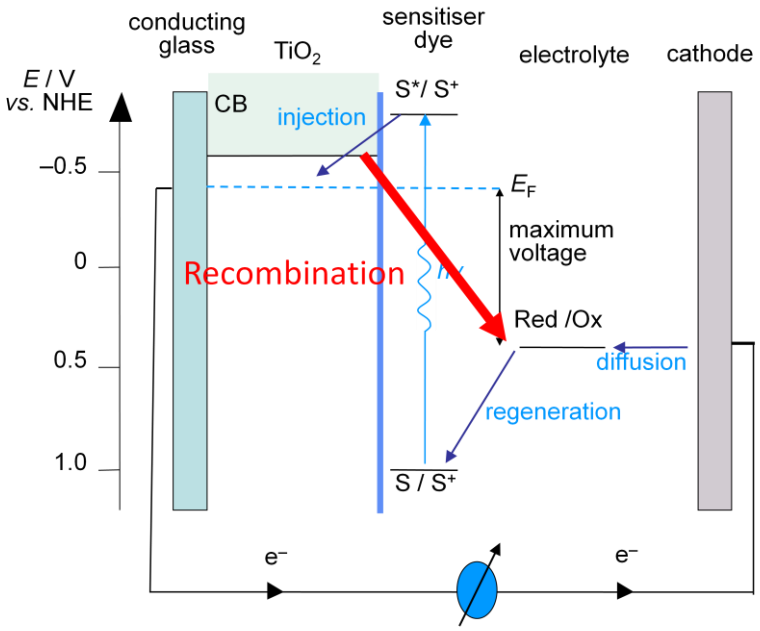

Figure 1-5. Energy band diagram of a typical DSSC employing an iodide/triiodide-based redox eletrolyte in acetonitrile and N719 as a sensitizer.

To drive DSSCs to work, the following reactions occur in the cell on electrodes or in the electrolyte.

On the working electrode (anode):

1. Photoexcitation (absorption) $D + h\nu \rightarrow D^*$ (Equation 1-1)
2. Electron Injection $D^* \rightarrow D^+ + e^-_{CB}\ (TiO_2)$ (Equation 1-2)
3. Regeneration $2D^+ + 3I^- \rightarrow 2D + I_3^-$ (Equation 1-3)
4. Recombination to dye (CRD) $D^+ + e^-_{CB}\ (TiO_2) \rightarrow D$ (Equation 1-4)

On the counter electrode (cathode):

$$I_3^- + 2e^-\ (Pt) \rightarrow 3I^- \qquad \text{(Equation 1-5)}$$

In the electrolyte:

1. Redox couple (Keq=10^7 M^{-1} in acetonitrile[38]) $I_2 + I^- \rightleftharpoons I_3^-$ (Equation 1-6)
2. Recombination to electrolyte (CRE, 'dark current')

$$I_3^- + 2e^-_{CB}\ (TiO_2) \rightarrow 3I^- \qquad \text{(Equation 1-7)}$$

Overall, the whole cell: $e^-\ (Pt) + h\nu \rightarrow e^-_{CB}\ (TiO_2)$ (Equation 1-8)

Water is always present in cells as they are normally constructed under ambient conditions.[33] In addition, water vapour can penetrate through the sealing materials with time. Possible reactions occurring between iodine and water produce hypoiodite, OI^-, proton and iodide, in Equation 1-9 ($K = 5.4\times10^{-13}$).[39] This could further produce triiodide.

$$I_2 + 2H_2O \rightleftharpoons HOI + 2H_3O^+ + I^- \qquad \text{(Equation 1-9)}$$

DSSCs work efficiently because all the above reactions occur in the cells at different time scales. The kinetic diagram of DSSC function employing an iodide/triiodide-based redox electrolyte and dye N719 as a sensitizer is shown in **Figure 1-6**.

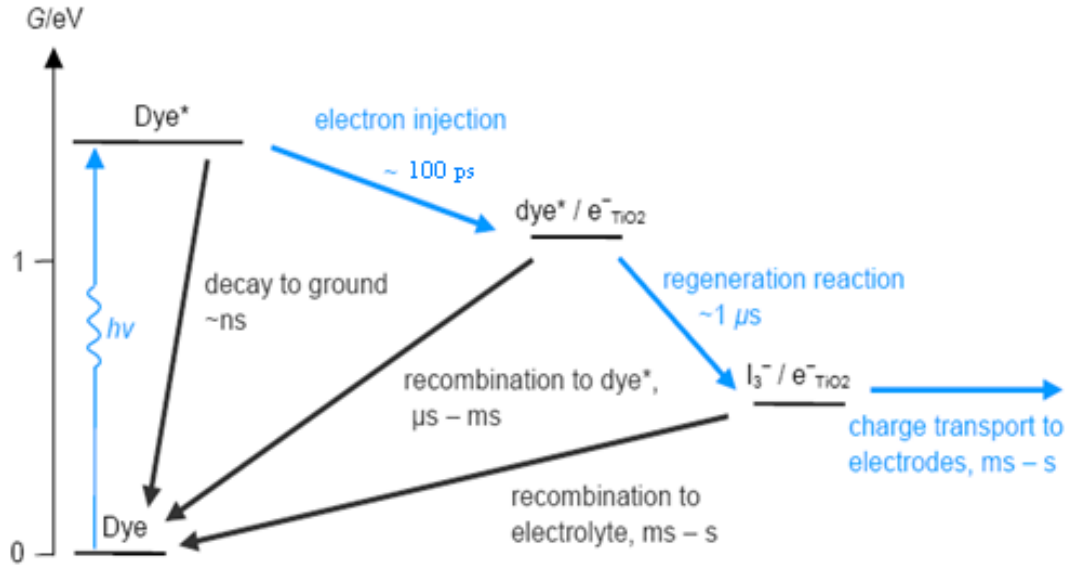

Figure 1-6. Kinetic diagram of a typical DSSC employing an iodide/triiodide-based redox eletrolyte and N719 as a sensitizer. Reproduced from reference[40].

The cell's overall efficiency (η) is defined as

$$\eta = \frac{Pw}{Pin} = \frac{JscVocFF}{Pin} \qquad \text{(Equation 1-10)}$$

where *Jsc* is short-circuit photocurrent density, mA/cm^2; *Voc* is the open-circuit photovoltage, V; *FF* is the fill factor, which is dependent on the series resistance and charge recombination; and the incident solar irradiance under AM1.5 sunlight is *Pin* = 1000 W/m^2.

To optimise a cell's performance, all *Jsc*, *Voc* and *FF* need to be increased. The cell's *Jsc* can be increased by improving light harvesting with red and near-infrared dyes[41] , cosensitisation of two dyes[42] and scattering layers[43] which broadens the steady-state incident photon-to-electron conversion efficiency (IPCE). The cell's *Voc* can be increased by decreasing the recombination by using a backing layer on FTO glass[44] and an insulating metal oxide layer to coat TiO_2 particles[45]. Of particular relevance to this thesis, previous works in my group have shown that the interaction between the iodine in the electrolyte and dyes such as phthalocyanines and some ruthenium dyes can increase recombination kinetics, decreasing cell's *Voc* and thus decreasing the

device efficiency. Chapter 7 will focus on the iodine binding and its effect on cell performance.

1.2.3.2 Heterogeneous sensing

General sensing strategies aim to detect and quantify analytes selectively and sensitively (i.e. with a low limit of detection (LOD)). Chemical sensors also need to be reversible, long-lived and have a fast response time.[46,47] They transduce a chemical signal into a signal which can be read optically or electrically by an observer or by an instrument, and can be used to detect analytes in either organic or aqueous solutions based on the interaction/reaction between the species of interest and the molecular receptor.

The idea of heterogeneous sensing is to overcome some of the disadvantages associated with homogeneous (e.g solution) sensing, including irreversibility and non-reusability without further solution separation.[46] It is also called 'dip-in sensing' and often employs molecular receptors immobilised on solid supports.[48] It can be more convenient than homogeneous sensing and has been suggested to enable quicker and easier detection of, for example, toxic heavy metals such as mercury, or anions such as cyanide in wastewater - either optically or electrochemically, thus accomplishing 'real' sample ease of detection.[49-51]

Heterogeneous sensors can be constructed by using a range of immobilization techniques, such as trapping, electrostatic interactions and covalent bonding, to attach a sensing probe/receptor (consisting of a cation/anion receptor, a binding site, which selectively recognises the ion of interest) onto a solid surface, such as polymer matrix or metal oxide.[49,50,52] It has recently been shown that functionalised mesoporous metal oxide films with molecular receptors can achieve colorimetric heterogeneous sensing for mercury ions and cyanide.[5,53]

1. General concept of molecular recognition

One possible approach for the development of heterogeneous sensors is to use molecular recognition where a chemical receptor can selectively bind (often via non-covalent interactions) to a target analyte (cationic, anionic or neutral). In supramolecular receptors, the interaction with analytes is often achieved by either hydrogen bonding or electrostatic interactions (particularly important if the analyte is positively or negatively charged).[54]

Currently, most molecular receptors/chemical sensors work only in homogeneous phase, where they are usually mixed with samples containing the target analyte.[46,55] This sensing strategy has been suggested not to be attractive for practical sensing application in real samples as it is normally difficult to regenerate and separate molecular receptors from the sample.[47] Meanwhile, these molecular receptors are normally dissolved in organic solution as they are often insoluble in water, and since the solvation energies of cations and anions in aqueous solutions are generally so high, it is difficult for a molecular receptor to overcome such energy to bind to the cations or anions.[56] This prevents their application to aqueous sensing such as in wastewater. One strategy to address this is for these molecular receptors to be modified with anchoring units so that they can attach to a surface or film for the application of heterogeneous sensing.

2. Molecular receptors

When designing a chemical receptor able to recognise a specific analyte for heterogeneous sensing, it is essential to consider some of the basic structural and electronic properties of the target analyte. Since the aim is to achieve complementarity between host (molecular receptor) and guest (analyte), several properties such as electrostatic charge, geometry, size and pH sensitivity must be considered when developing novel receptors. Furthermore, if the receptor is to be used as a chemical sensor, besides the binding site (recognition), it is necessary to introduce a signalling

subunit (sensing unit), and an anchoring unit which is needed to attach to the solid supports.

Molecular receptors can be either organic compounds or metal complexes on biomolecules. In the later, the metal centre often plays an important role in pre-organising the binding (recognition) group(s) in the molecular receptor for optimal and selective sensing. Meanwhile, the interaction between molecular receptors and anionic analytes is also enhanced due to the positively charged metal centres.[57]

One example of neutral receptors for anion sensing, based on hydrogen bonding, are well-known NH-containing compounds such as pyrroles, amides and urea/thioureas (**Scheme 1-3**).[58] Another family is the positively charged molecular receptors that use ammonium and guanidinium groups to bind anions.[58] These molecular receptors bind to anions such as $[HPO_4]^{2-}$ in aqueous solution at pH 7.4.

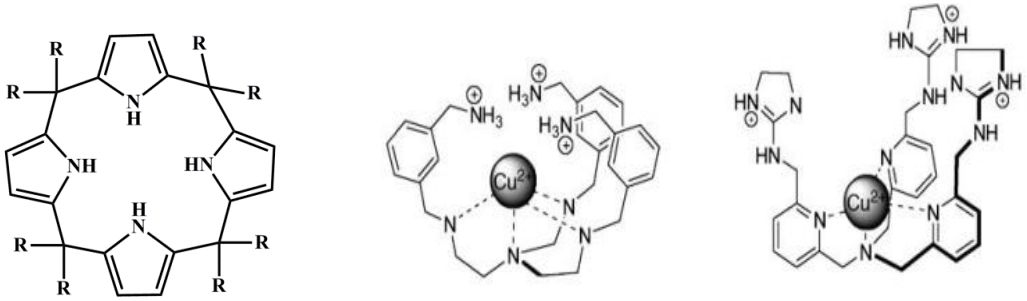

Scheme 1-3. Chemical structures of pyrrole (a) and receptors containing positive charged Cu(II) with ammonium (b) and guanidinium (c) groups. Reproduced from reference[58].

Regarding cations, an important family of receptors are those based on crown ethers and their derivatives(**Scheme 1-4**).[59] The nature of the heteroatom present in the macrocycle partly determines the affinity of the receptor for a given analyte. For example, oxygen-containing macrocycles tend to bind stronger to alkaline metal cations (such as K^+ and Na^+) while those that contain sulfur atoms have higher affinity to softer metal cations such as copper (Cu^{2+}).[59] On the other hand, polyamine chains and macrocycles bind effectively to Zn^{2+} and terpyridyl diester to Eu^{3+}, [60] and NCS ligands to mercuric ion (Hg^{2+})[5].

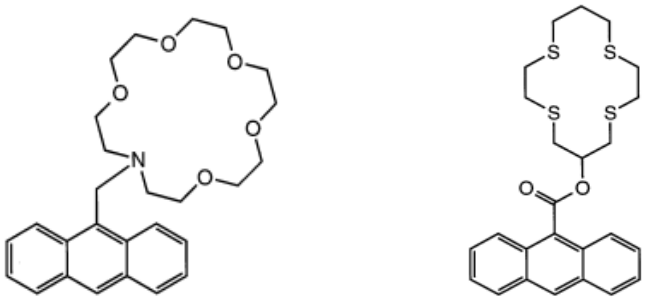

Scheme 1-4. Chemical structures of macrocyclic compounds with nitrogen atoms and sulfur atoms. Reproduced from reference[59].

Once the molecular receptor is linked to a signal group/unit, there can be a detectable optical/electrochemical signal in which case a chemical sensor is developed, as has been reviewed previously.[51,61,62] The signalling unit senses the interaction between the molecular receptor and analyte. For chemical sensing, the signal is normally either optical or electrochemical. For example, metallo-receptors often make use of the unique optical and electronic properties of the metal centre(s) so that binding to a given analyte induces a change that perturbs the metal centre. This process can then be monitored by changes in a given metal-centre property (optical, electrochemical, etc).[57]

The anchoring unit of molecular receptors can be selected from a variety of groups depending on which solid support materials the receptors will be attached to. For example, carboxylic acids[2] and phosphonic acids[63] are common anchoring units for attaching to metal oxide films, while the thiol compounds(such as 11-mercaptoundecanoic acid[64]) are generally employed to modify gold nanoparticles (forming strong S-Au covalent bonds).

In this project, developing receptors for anions and cations that pose some environmental threats are particularly targeted. As will be discussed in subsequent chapters, dip-in chemical sensors for cyanide and mercury have been developed.

3. Analyte / receptor interactions

The interaction between optically active molecular receptors and analytes can yield new complexes, changing the electronic properties and shifting the absorption

spectrum of receptors. The binding mechanism to explain the new complexes depends on the type of optically active receptor. In chemosensors, photoinduced processes determine the photophysical changes upon analyte binding[60,65]. For example, the enhancement of emission in fluoroscent chemosensors can be related to photo-induced electron transfer (PET) processes in which the fluorophore is an acceptor and the cation receptor is an electron donor (e.g. amino group), as shown in **Scheme 1-5**.[59] Cation binding to the electron donor group raises the redox potential of the donor, decreasing the HOMO energy level down below the fluorophore's HOMO. This suppresses the PET process. As such, the fluorescence intensity is enhanced.

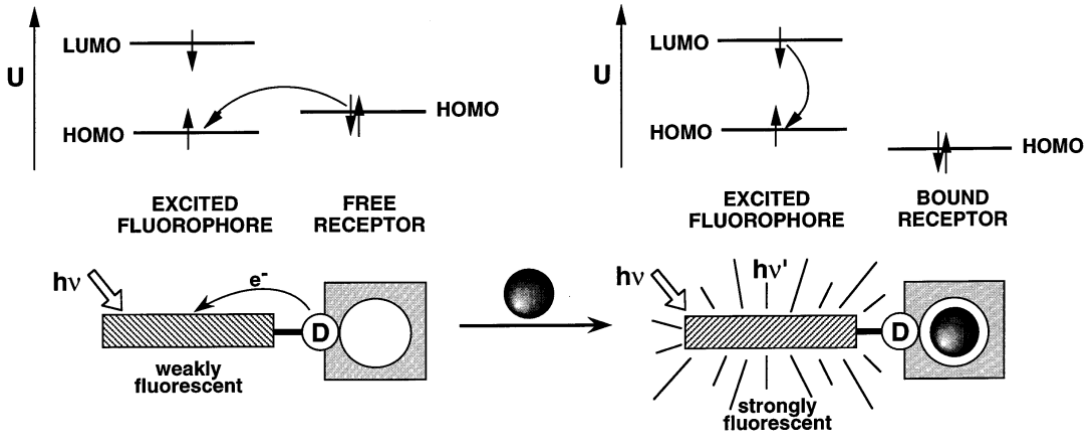

Scheme 1-5. Principle of PET process with the participation of the HOMO and LUMO of the fluorophore and an external molecular orbital (donor). Reproduced from reference[59].

Another binding mechanism comprises charge transfer (CT) processes induced by analytes, including intramolecular charge transfer (ICT) and metal–ligand charge transfer (MLCT)[65], which is more relevant to the results presented in this thesis. The HOMO and LUMO energy level of molecular receptors determines its visible light absorption peak. The cation or anion binding to the electron donor/acceptor in the molecular receptor changes its electron-accepting ability and its HOMO or LUMO level, leading to a shift in the absorption spectrum of the molecular receptor. For example, cation (Pb^{2+}) binding to the electron acceptor (pyridyl, where the LUMO is localised) increases its electron-accepting ability and decreases the LUMO of the molecular receptor.[66] This reduces the HOMO-LUMO gap, and causes red shifts in the absorption spectrum.

4. Binding constant of analyte to molecular receptors

The binding constant, *K*, is the overall equilibrium constant, defining the strength of interaction between molecular receptors and analytes. It is related to the Gibbs free energy of the binding process and is the criteria of binding affinity in homogeneous molecular recognition, although the efficient recognition of cations/anions is also dependent on how good the signal transduction and the binding selectivity are.

In solution, the equilibrium constants *K* can be determined by the Rose-Dragi (R-D) equation (Equation 1-12)[67] or Benesi-Hildebrand (B-H) equation (Equation 1-13)[68], assuming the interaction between an electron donor (D) and an electron acceptor (A) forms a 1:1 complex.

$$D + A \rightleftharpoons DA \qquad \text{(Equation 1-11)}$$

$$K = \frac{C_c}{(C_{D0} - C_c)(C_{A0} - C_c)} \qquad \text{(Equation 1-12)}$$

where C_C is the concentration of complex (DA) at equilibrium, C_{D0} and C_{A0} are the initial concentrations of the donor (D) and acceptor (A).

When only one complex (DA) is formed and the donor molecule does not absorb in the region studied, Equation 1-12 can be simplified (by ignoring the C_C^2 as C_C is normally no more than 10% of C_{A0}) to Equation 1-13, which is also called the B-H equation. The B-H equation is more often used than the R-D equation, and plotting $C_{AO}b/A_C$ versus $1/C_{DO}$ shows a linear behaviour with *K* determined from the slope.

$$\frac{C_{A0}b}{A_c} = \frac{1}{K\varepsilon_c}\frac{1}{C_{D0}} + \frac{1}{\varepsilon_c} \qquad \text{(Equation 1-13)}$$

where *b* is the path length of the cuvette and *Ac* is the absorbance of complex.

In this thesis, the equations described above for receptor-analyte interactions have been extended to solid surfaces. On solid surface, the binding constant is defined as the ratio of binding and unbinding rates of analytes bound to molecular receptors forming new complexes. It can be estimated by fitting the density of the newly formed

complex and the concentration of analytes after equilibration, following the Langmuir isotherm equation (Equation 1-14)[69].

$$\frac{\Gamma}{{}^{S}\Gamma} = \frac{K_f * C}{1 + K_f * C} = \frac{C}{(C + \frac{1}{K_f})} \qquad \text{(Equation 1-14)}$$

where Γ is the density of the new complex, in moles per cm^2 (surface area of mesoporous film) and ${}^{s}\Gamma$ is the density at full monolayer surface coverage, C is the concentration of analyte in solution.

5. Heterogeneous sensors

Supporting materials. To choose the appropriate solid supports, the charge, size and geometry, pH dependence and solvation of the analyte should be taken into account.[70] When using metal oxide films as the supporting materials, pH effects associated with the molecular recognition process should be considered because of the potential problem of protonation and desorption of molecular receptors from the surface. Molecular receptors anchored on TiO_2 films can be desorbed at basic pH values (pH > 8). Previous studies have shown that the TiO_2 film acts as a strong pH buffer in the range between 3.5 and 8.0 (the point of zero charge (PZC) of TiO_2 films is ~5).[18,53] In alkaline solution, the molecular receptors adsorbed onto the TiO_2 films are easily desorbed. This limits its usage in anion sensing as its surface charge is negative under high pH conditions, resulting in the desorption of functional molecular receptors.

Optical heterogeneous chemical sensors. Optical sensors detect analyte-induced changes of optical properties of molecular receptors, either by absorption or emission. Colorimetric sensing is an easy and simple method of sensing[5] since detection can involve the observation of colour changes by 'naked eye'. This is a potential advantage over other chemical sensors such as electrometric and fluorometric sensors which require either a potentiostat or a spectrofluorimeter, as has been reviewed previously.[46,55,71] A typical colorimetric heterogeneous sensors based on nanocrystalline mesoporous metal oxide films is shown in **Scheme 1-6**.

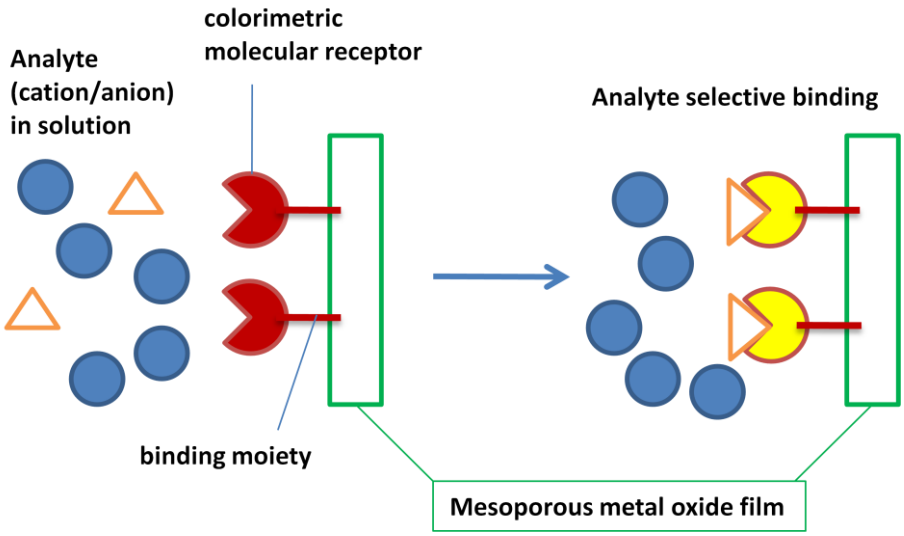

Scheme 1-6. Diagram of a colorimetric nanocrystalline metal oxide based chemical sensor.

A typical example is N719-functionalised TiO_2 films which can achieve a 20 ppb Limit of Detection (LOD) for mercury(II) sensing in drinking water[5] (**Scheme 1-7**).

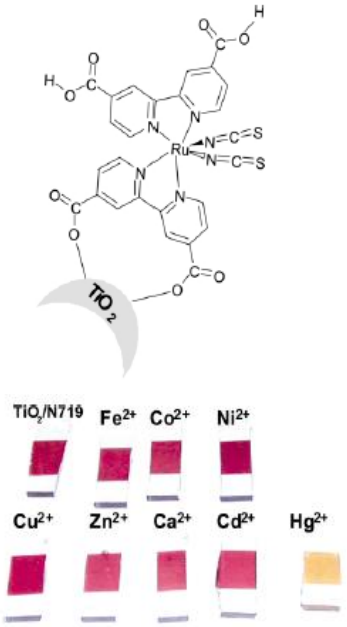

Scheme 1-7. N719/TiO_2 films dipped in different cations' solutions, only mercury shows the colour changes from red to yellow. Reproduced from reference[5].

Electrochemical heterogeneous sensors. Electrochemical heterogeneous sensors can be developed by attachment of a redox-active group to a receptor, in which the binding process must be coupled to the redox reaction[54]. This binding/interaction between molecular receptors and analytes often changes the voltammetric response through either the oxidation or reduction of the adsorbed redox species which relates

to the analyte concentration. They are chemical sensors which function by employing a potentiostat. They commonly measure either voltages (potentiometric sensor), current (amperometric sensor) or resistance (impedimetric sensor) of an electrochemical cell in response to the analytes.[51,72] These sensors are widely used to monitor gases (e.g CO, NO_x, SO_2,) and heavy metals in solution.[73-76] The main advantages of these sensors are their simplicity of construction, disposable electrodes and high sensitivity. However, the molecular receptors used have to contain a redox couple for reversible sensing. This imposes important limitations on which metal complexes can be selected to functionalise nanocrystalline, mesoporous metal oxide films for sensing cations/anions electrochemically. In chapter 5, a cation percolation electrochemical sensor is described. This was set up by using an electroactive receptor (in this case, dye molecules) attached onto the nanocrystalline, mesoporous TiO_2 film as the working electrode in a three-electrode-cell. Under application of a positive bias, in the presence and absence of analyte (in this case mercury), a voltammetric technique such as cyclic voltammetry (CV) is used to measure either the oxidation peak current of the redox receptor or the cation diffusion coefficient which is linearly proportional to the concentration of the analyte (**Figure 5-7**).

Biosensors and redox protein studies. Nanocrystalline, mesoporous metal oxide films, such as nanocrystalline SnO_2 and TiO_2, with immobilised protein/enzyme can be used not only as biosensors to detect NO (with the haemoglobin/SnO_2 film)[77], bacterial *Vibrio cholerae* (with the ssDNA/NanoZrO_2/ITO film)[78], H_2O_2 for living cancer cells (with flavin adenine dinucleotide/TiO_2 film[79] or cytochrome C/ZnO nanosheet[80]), but also for fundamental studies such as the redox enzyme thermodynamic properties[81] and kinetic analysis of redox and coupled-chemical events spectroelectrochemically[82]. A network of interconnected nanoparticles allows the study of photoinduced protein/electrode transfer reactions.[83] The advantages of protein immobilisation in nanocrystalline, mesoporous films enables large amount of protein loading and directly electrochemical measurements on immobilised proteins without the use of electron transfer mediators and promoters comparing to flat electrodes and other methods used in biosensors.[84] This strategy provides novel and powerful approaches in biosensing and studies of proteins redox chemistry.

1.2.3.3 Cation/hole **Percolation and molecular wiring**

The functionalisation of nanocrystalline mesoporous metal oxide films has been reported to result in efficient lateral cation (or hole, considered to be an unfilled HOMO orbital) percolation across the internal surface of the films when the surface coverage of some of electroactive molecules (in this case, dye loading) exceeds a threshold concentration.[17] At this threshold, the molecules rapidly switch from disconnected non-conducting 'islands' to a connected conducting network, through which charge can be transported in the film (**Scheme 1-8**a).[85] Such faster charge percolation is currently under investigation to enable the molecular wiring of otherwise insulating wide bandgap inorganic materials for applications in percolation battery by increasing the conductivity of the lithium materials, **Scheme 1-8**b[86] and in molecular nanotransistors as the gate material[87].

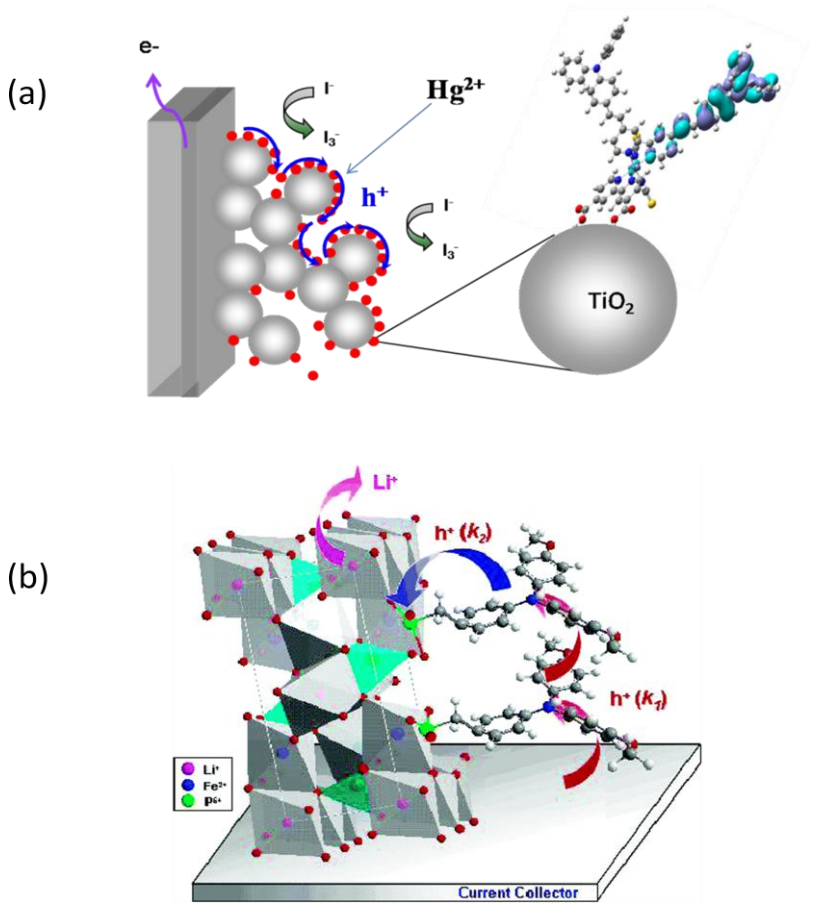

Scheme 1-8. (a) The lateral cation percolation through the molecular monolayer adsorbed on nanocrystalline, mesoporous metal oxide films. Reproduced from reference[85]. (b) Structure of LiFePO4 and the triarylamine (BMABP) substituted by a benzylic phosphonate anchoring group acting as molecular charge transport material. Reproduced from reference[86].

1.3 Aims and objectives

Although there are many publications of functionalised metal oxide films in dye-sensitised solar cell (DSSC) and some for heterogeneous sensing, there are still challenges in both basic science and new technology. These include the interaction between the molecular receptors and the metal oxide films, understanding the molecular structures of receptors *vs.* charge transfer mechanism/dynamics between receptors to analytes, the function of nanopores and their interactions with cations/anions. The issue of the interaction of dye sensitized metal oxide films with solution molecular species such as complex interactions between dye/TiO_2 surface and electrolyte, has potential importance not only for DSSC device performance, but also more generally for the development of heterogeneous sensors to improve sensing reusability. Therefore, this thesis principally focuses on coupling molecular receptors with nanocrystalline metal oxide films for applications in DSSCs, heterogeneous sensors (optical, electrochemical, electro-optical) and selective toxic metal scavenging. The objectives of the research carried out during this PhD are summarised as follows:

- To understand and develop novel optical cation and anion sensors by employing functionalised nanocrystalline, mesoporous metal oxide films;
- To evaluate the potential use of such functionalised films in pollutant scavenging;
- To evaluate cation/hole percolation across molecular monolayers adsorbed to nanocrystalline, mesoporous metal oxide films, leading to the correlation between molecular structure and the cation/hole percolation dynamics and the fabrication of electrochemical cation and anion sensors based upon these percolation processes;
- To study iodine binding to nanocrystalline TiO_2 films in the presence and absence of an adsorbed dye monolayer, and the impact of these iodine binding processes upon the efficiency of dye-sensitised solar cells.

1.4 Structure of thesis

Chapter 2 presents details of the methods used in preparation of TiO_2, Al_2O_3 and ZrO_2 pastes and nanocrystalline, mesoporous films, and the experimental techniques to characterise these films.

In **chapter 3** the functionalisation of nanocrystalline, mesoporous Al_2O_3 films by molecular receptors - an azo-phenyl thiourea based organic molecule - for optical heterogeneous cyanide sensing in aqueous solutions is reported. The functionalised nanocrystalline, mesoporous Al_2O_3 films respond by displaying a colour change from yellow to orange-red in the absence and presence of cyanide, respectively.

Chapter 4 extends the sensing strategy introduced in chapter 3 by employing functionalised nanocrystalline TiO_2 films with a more complicated structured metal complex, named 'N719', to design mercury scavenging molecular materials (SMM) to prevent environmental mercury contamination. This binding of mercury ions to the N719 molecules attached to the nanocrystalline, mesoporous TiO_2 films can be used to remove mercury ions from contaminated aqueous solutions or wastewater to remediate water pollution.

Due to the proven interaction between NCS ligands in the ruthenium dye and mercury, as described in chapter 4 and previous reports[86,88], analogous electroactive ruthenium complexes, named 'N621' and 'HW456', were considered in **Chapter 5** to develop voltammetric sensors for sensing mercury, and to study the cation charge transportation in DSSC. Changes in dye cation percolation behaviour in the presence of mercury are shown to be an effective mercury sensing strategy. The cation percolation dynamics of molecular networks of these ruthenium dyes was investigated and dye cation diffusion lengths are estimated. These results are then discussed in the context of dye cation regeneration in DSSCs.

In **chapter 6**, the formation of triiodide ions in nanopores of nanocrystalline metal oxide films in iodine acetonitrile solution is reported. This effect can be reversed by

washing the films with iodine/iodide mixture which indicates the triiodide formation is reversible. This study addresses the diffusion, reaction and mass transport of iodine and triiodide in the electrolyte in dye-sensitised solar cells.

In **chapter 7**, dye-iodine interactions have been studied. In the presence of iodine, a blue shift in absorption spectra of three analogous ruthenium dyes, named 'N719', 'C101' and 'AR24', with –NCS only and/or -NH_2 groups, is observed. This implies iodine binds to sulfur or nitrogen donor atoms in these dyes. This dye-iodine binding studies may have implications for optimizing cell performance through modification of dyes structure and the electrolyte composition, and the potential for the dye to function as an iodine receptor.

Chapter 2 Experimental Methods

This chapter describes the general procedures for the preparation of functionalised nanocrystalline, mesoporous metal oxide films and the experimental techniques used to analyse these films. For experimental techniques specific to a given study, please refer to experimental sections within relevant chapters.

All solvents and chemicals, unless otherwise stated, were purchased from Sigma-Aldrich or their subsidiaries and were used without further treatment. Substrates used in this thesis are fluorine-doped conducting glass (TEC15, purchased from Hartford, USA) and microscope slides (1 mm thick, VWR International). The sensitiser dye N719 was supplied by Dyesol. Other dyes were synthesised by collaborators as detailed in each individual chapter. All experiments were performed at room temperature.

2.1 Nanocrystalline, mesoporous metal oxide film fabrication

There are many different physical and chemical ways to prepare nanocrystalline, mesoporous metal oxide films. Following advances in the field of colloidal and sol-gel chemistry, in this thesis nanocrystalline metal oxide pastes (or colloidal solutions) were prepared in two steps: sol-gel process followed by hydrothermal treatment. A typical sol-gel process involves the hydrolysis and polycondensation reactions of metal alkoxides. Hydrothermal treatment, also called hydrothermal precipitation, involves a hydrothermal reaction in aqueous solution at a relatively high temperature (>100 C) and pressure (>1 bar) in an autoclave. Afterwards, nanocrystalline, mesoporous metal oxide films were fabricated by spreading these nanocrystalline metal oxide pastes on substrates, followed by a heat treatment to sinter the

nanoparticles. This procedure ensured the control of the morphology of nanocrystalline, mesoporous metal oxide films.[83,89]

In my thesis, nanocrystalline TiO_2 pastes were prepared starting from the titanium tetraisopropoxide (Ti(iso-$OC_3H_7)_4$) precursor, while nanocrystalline Al_2O_3 and ZrO_2 pastes were prepared using commercial colloidal dispersions supplied by Alfa Aesar.

2.1.1 Sol-Gel process

The sol-gel process is a wet-chemical technique that can be used for the preparation of metal oxide nanoparticles at a low temperature. It starts from metal alkoxides as precursors, mixed with acid (or base) to make it soluble in water, and hydrolysed to form sol (solution) and then gel (or an integrated network). A typical example using sol-gel process to prepare nanocrystalline TiO_2 pastes is the hydrolysis of titanium tetraisopropoxide, as shown in Equation 2-1.

$$Ti(iso\text{-}OC_3H_7)_4 + 4\,H_2O \rightarrow Ti(OH)_4 + 4\,C_3H_7OH \qquad \text{(Equation 2-1)}$$

Glacial acetic acid (CH_3COOH) - a chelating agent – is often used to slow down the fast hydrolysis rate of titanium tetraisopropoxide by substituting one isopropoxy group with a less-hydrolyzable group, *i.e.* acetate, thus leading to more monodisperse and smaller sols[90]. In addition, the acetate groups act as dispersing agents on the surface of the TiO_2 particles and prevent nanoparticle aggregation during the hydrothermal step.[89] The hydrolysis of titanium tetraisopropoxide was then peptized with appropriate amounts of nitric acid (HNO_3) to form a highly dispersed, stable colloidal dispersion.

As the formed titanium hydroxide ($Ti(OH)_4$) particles in aqueous suspensions have an isoelectric point (IEP) of pH = 6.8[91], the addition of nitric acid makes the particles' surface positively charged due to the adsorption of protons. Thus, the lower the pH value, the more surface positively charged. As the positive charged nanoparticles repel each other, the sols are more stable than uncharged nanoparticles. **Figure 2-1** shows that the stable sols exist in a range of 0.1~1.0 of the mole ratio of H^+ to Ti.[33,91]

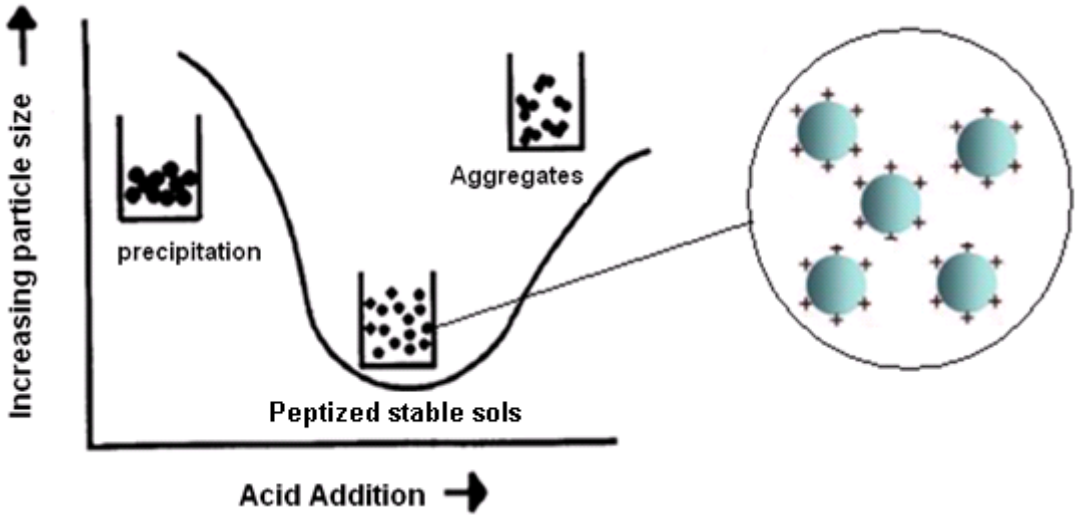

Figure 2-1. Effect of acid concentration on particle size. Reproduced from references[33,91].

2.1.2 Fabrication of nanocrystalline mesoporous TiO_2 films

Firstly, nanocrystalline TiO_2 pastes comprising of 15~25 nm-sized anatase TiO_2 particles were prepared according to reference[89] with some modifications. In detail, 40 ml of titanium tetraisopropoxide was mixed with 9.1 g of glacial acetic acid under nitrogen atmosphere to avoid the rapid hydrolysis of titanium isopropoxide in ambient conditions and stirred for 10 minutes. The mixture was then poured into a conical flask containing 240 ml of 0.1 M nitric acid solution at room temperature and subsequently stirred at 80ºC for 8 hours. Afterwards, the TiO_2 colloid containing 5~8nm TiO_2 particles was filtered using a 0.45 µm syringe filter and then autoclaved at 220ºC for 12 hours. As the particle size was increased (to ~15 nm) and sedimentation occurred during autoclaving, the TiO_2 colloid was then re-dispersed by sonicating for 2 min from a LDU Soniprobe horn and concentrated to 12.5% (in TiO_2 weight) on a rotary evaporator using a membrane vacuum pump at 45ºC. Polyethylene glycol (PEG) 20,000 (50% of TiO_2 by weight) was added to the above colloidal solution to prevent subsequent film cracking during heat treatment and to enhance film porosity. The resulting colloidal solution, or paste, was stirred slowly overnight prior to film deposition to ensure the film's homogeneity and that no air bubbles were trapped in the film.

Secondly, the paste was spread on glass substrates such as FTO glass, using a glass rod with 3M adhesive tapes (as a spacer) to fabricate nanocrystalline, mesoporous TiO_2 films. The technique to make films, commonly referred to as "doctor blading", is shown in **Figure 2-2**. After drying in air at room temperature, the films were sintered at 450ºC for 30 minutes in a furnace. The resulting film thickness, using one layer of 3M adhesive tape, was of ca. 4 µm, measured by using an Alpha-step 200 surface profilometer (Tencor Instruments, USA).

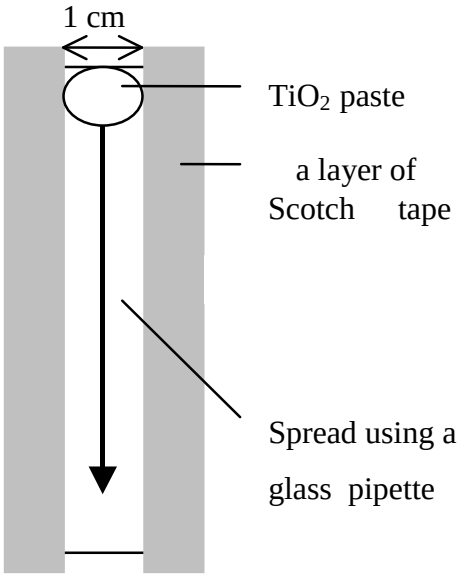

Figure 2-2. "Doctor blade" technique of preparing nanocrystalline TiO_2 films.

In chapter 3, a diluted TiO_2 paste and microscope slides substrates were employed to obtain thin TiO_2 films for cyanide sensing. The diluted paste was prepared by diluting the above TiO_2 paste with addition of distilled water (50:50 w/w to the TiO_2 paste). Typical film thickness, using one layer of Scotch tape, was of 1.4±0.1 µm.

2.1.3 Preparation of nanocrystalline mesoporous Al_2O_3 films

Commercial colloidal dispersion aluminium oxide (50 nm, 20% in H_2O, Alfa Aesar) was suspended in distilled water (50:50 w/w). Then, 2 wt% of hydroxypropyl cellulose (HPC) 370,000 was added to the above suspension. The mixture was stirred slowly for a week to allow HPC to dissolve completely to obtain the Al_2O_3 paste. The

Al_2O_3 paste was doctor bladed onto microscope slides to prepare Al_2O_3 films. The films were dried at room temperature for about 20 min and then sintered at 400°C for 30 min.

2.1.4 Preparation of nanocrystalline mesoporous ZrO_2 films

Commercial colloidal dispersion Zirconium (IV) oxide (ZrO_2) (0.1 µm, 20% in H_2O, Alfa-Aesar) was mixed with acetic acid in a Teflon beaker. This mixture was stirred for one and half days, and then autoclaved at 240^0C for 3 days. Afterwards, the ZrO_2 colloidal solution was sonicated for 1 minute. Later, a certain amount of PEG 20,000 was added and stirred slowly overnight to make ZrO_2 paste. The ZrO_2 films were obtained by doctor-blading the ZrO_2 paste, dried at room temperature for about 20 min and then sintered at 400°C for 30 min.

All nanocrystalline, mesoporous metal oxide films were cut into pieces in required sizes, and then re-sintered prior to dye sensitization.

2.2 Characterisation of nanocrystalline, mesoporous metal oxide films

Nanocrystalline, mesoporous metal oxide films were characterised by measurements including absorption spectroscopy for their optical properties, scanning electron microscopy (SEM) for film morphology, X-ray powder diffraction (XRD) for crystal structure and Brunau-Emmett-Teller surface area measurement (BET) for the internal surface area.

2.2.1 Techniques

2.2.1.1 Scanning electron microscopy (SEM)

SEM is a type of electron microscope that is well suited to investigate morphology, texture and surface features of powders or films. The morphology of nanocrystalline,

mesoporous metal oxide films were studied using a Philips XL-30 field emission gun scanning electron microscope (Natural History Museum, UK). Samples were coated with Au/Pd (~2 nm) prior to observation.

2.2.1.2 Brunau-Emmett-Teller (BET) measurements

The absorption and desorption of liquid nitrogen onto powders or mesoporous films under pressure, done by Brunau-Emmett-Teller (BET) measurements, can provide useful information of films, such as pore size and distribution. The estimated pore size distribution can be calculated by the Kelvin equation (Equation 2-2). The roughness factor η of these films, defined as the ratio of the effective surface area of nanocrystalline, mesoporous film to its projected area (1 cm^2 in this case), can be estimated.

$$\ln(P/P_0) = -2\gamma V / rR_gT \qquad \text{(Equation 2-2)}$$

where P is the actual vapour pressure, P_0 is the saturated vapour pressure, γ is the surface tension, V is the molar volume, R_g is the universal gas constant, r is the radius of the particle, and T is temperature.

2.2.1.3 X-ray powder Diffraction (XRD) measurements

X-ray powder diffraction (XRD) is a method to determine the crystal lattice of a material based on the diffraction of highly energetic X-rays. It gives information about the crystal structure of a material. The XRD of the Al_2O_3 and TiO_2 films were measured by a Bruker Advance D8. The measurements being made in the 2θ range 20-80º use CuK alpha radiation (ICIQ, Tarragona, Spain and Imperial College London, London, UK). Scherrer's Equation (Equation 2-3) can be used to estimate the particle size.

$$d = \frac{0.9\lambda}{(w - w_1)\cos\theta} \qquad \text{(Equation 2-3)}$$

where d is the particle diameter, w and w_1 are the half-intensity width of the relevant diffraction peak and the instrumental broadening, respectively, λ is the X-ray wavelength and θ is the angle of diffraction.

2.2.2 Materials Characterisation Results

A typical nanocrystalline, mesoporous TiO_2 film (anatase) used in my studies was of ca. 4 µm thick and comprises nanoparticles of ~15 nm with a pore size of 5~30 nm, as illustrated in the SEM image shown in **Figure 2-3**.

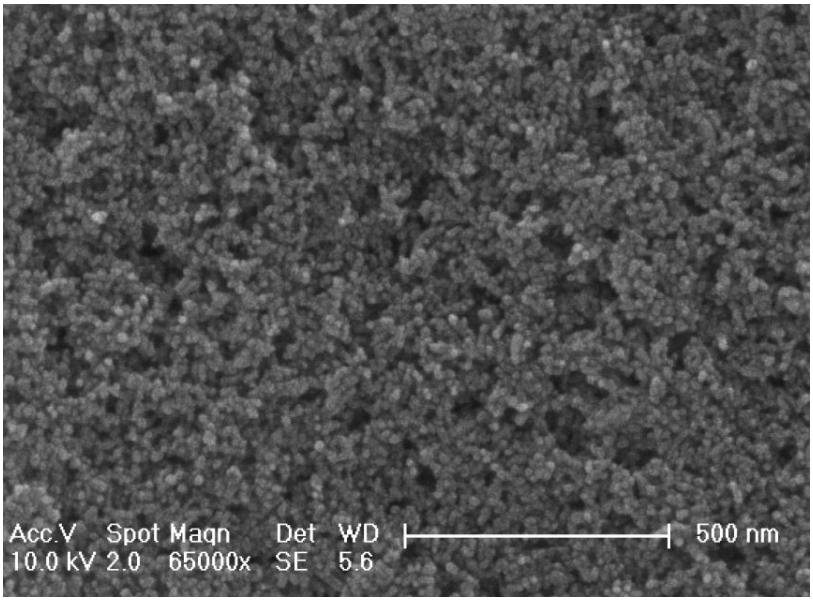

Figure 2-3. SEM image of a ~4 µm thick nanocrystalline TiO_2 film. The scale bar is 500 nm. Particle size is ~15 nm.

Figure 2-4 shows the pore size distribution of the TiO_2 and Al_2O_3 films determined from the BET measurements. The estimated pore size distribution is 20 and 5 nm of 90% pores for TiO_2 and Al_2O_3 films, respectively.

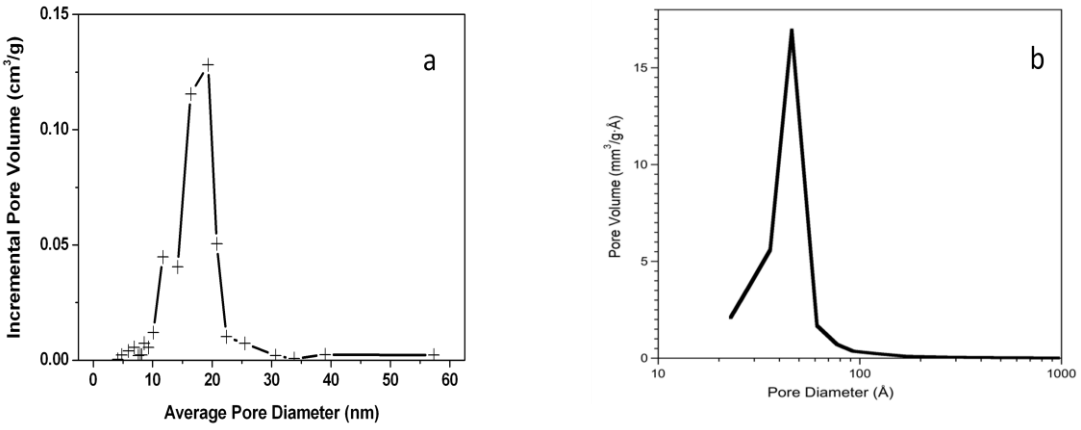

Figure 2-4. The pore size distribution of (a) TiO_2 and (b) Al_2O_3 films.

The BET surface area of the TiO_2 film is 106 m^2/g. To adsorb molecular acceptors at a high surface loading, the nanocrystalline, mesoporous films should have the pore size much bigger than the size of adsorbed metal complex molecules (normally ~1 nm).

The XRD of films shows that the TiO_2 film is anatase and the Al_2O_3 film is either γ-Al_2O_3 or the η-Al_2O_3 crystal(**Figure 2-5**). The estimated particle size calculated by Scherrer's equation is 10 nm and 50 nm for the TiO_2 and Al_2O_3 films, respectively. This particle size is slightly smaller than that estimated from the SEM measurements.

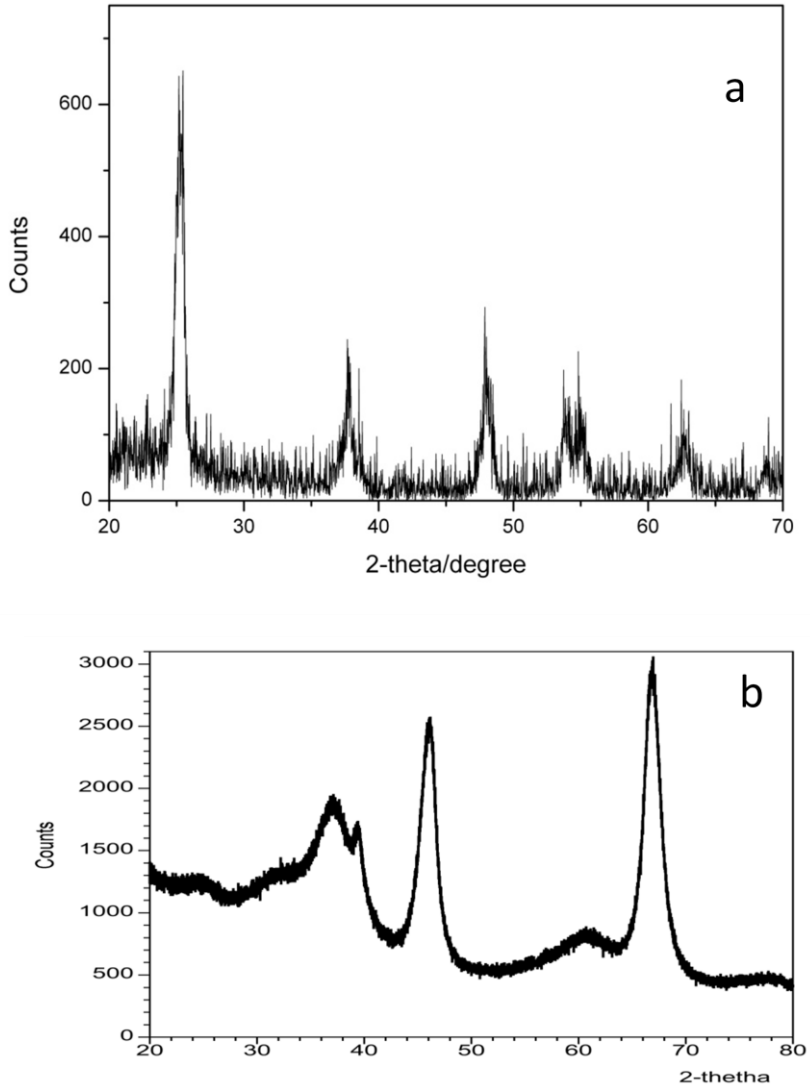

Figure 2-5. The XRD of TiO_2 film (a) and Al_2O_3 film (b).

In summary, these nanocrystalline, mesoporous metal oxide films provide a high surface area compared to flat films. Some of the parameters of metal oxide films studied in my thesis are listed in **Table 2-1**. These parameters are used to estimate films' surface loading in chapters 3-7 (details see 2.3) and the electron diffusion length/area in chapter 5.

Table 2-1 Parameters of metal oxide

Nanocrystalline metal oxide	**TiO_2**	**Al_2O_3**
Particle size	~15 nm (ICL paste, UK) 18~20 nm (DSL-18NRT paste, Dyesol)	50 nm
SEM image	**Figure 2-3**	
Surface area (BET)*	~100 m^2/g (ICL)	~274 m^2/g (measured in ICIQ, Tarragona, Spain)
Pore size (BET)	5-30 nm (ICL)	2-10 nm (ICIQ)
Pore distribution (BET)	**Figure 2-4**a (ICL)	**Figure 2-4**b (ICIQ)
Film porosity	50 ± 5%	
Crystal (XRD)	Anatase (ICL); **Figure 2-5**a	γ-Al_2O_3 or β-Al_2O_3; **Figure 2-5**b (ICIQ)
Film thickness (Alpha 200 Profilometer)	~4 μm Diluted paste: 1.4 ± 0.1 μm	3.8 ± 0.2 um
Film's roughness factor (η)	450 for a 4 μm-thick film (ICL)	

* The BET samples (~30 mg) were prepared by scratching the films off the substrates.

2.2.3 Steady-state UV-Vis Absorption Spectroscopy

UV-Vis absorption spectra of dye-sensitised metal oxide films were monitored at room temperature using Thermo Genesys 10 UV-Vis Spectrophotometer. The spectral resolution of the spectrophotometer is 2 nm and the spectrum was collected with a sampling interval of 2 nm. Steady-state UV-Vis spectra of TiO_2 and Al_2O_3 films on microscope slides are plotted in **Figure 2-6**. It shows that there is negligible

absorbance in the visible region but a very strong UV absorption (< 360 nm) of the TiO_2 film, while the Al_2O_3 film are transparent down to 300 nm, which is consistent with their reported bandgaps (3.2 eV for TiO_2 and 8.45~9.9 eV for Al_2O_3[11]). This optical transparency of nanocrystalline TiO_2 and Al_2O_3 films makes them suitable for optical and spectroelectrochemical measurements of adsorbed molecules in the visible region.

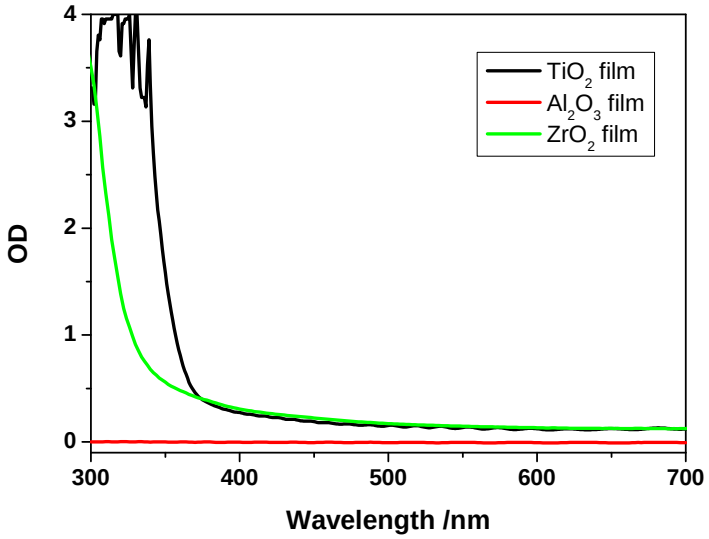

Figure 2-6. UV-Vis spectra of the TiO_2 film (**black**) and ZrO_2 film (**green**) on FTO glass, and the Al_2O_3 film (**red**) on microscope slide. Baseline is air.

2.2.4 Cyclic Voltammetry (CV) and spectroelectrochemistry

2.2.4.1 Cyclic voltammetry (CV)

Cyclic voltammetry measurement is a common technique used to study ground state redox processes. It not only provides an estimation of the redox potential, but also provides information about the rate of electron transfer between the electrode and the adsorbed redox couple (in this case dye molecules), and the stability of the dye molecules in different oxidation states. This method uses a triangular potential scan (see **Figure 2-7**), *i.e.* the potential applied to a solution is scanned first towards more positive potentials at scan rate v_1, swept at the highest voltage E_2, and then the potential comes back down at the same rate v_2 (v_2=v_1) to the starting potential E_1. On

the reverse sweep, the oxidised species, which have been generated during the forward sweep, are reduced.

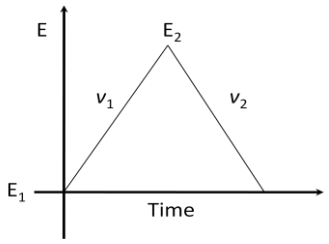

Figure 2-7. Typical voltage (E) changes during cyclic voltammetry.

Cyclic voltammetry on blank or dye-sensitised nanocrystalline, mesoporous metal oxide films were carried out in a vial with three electrodes which were connected to the potentiostat (Autolab PGSTAT12). The three electrodes are the films (as working electrode), Pt counter electrode, and quasi-reference electrode (QRE, a silver wire) which potential was found to be –0.35 V versus the ferrocene/ferrocenium redox couple. The electrolyte solution used was 0.1 M tetrabutylammonium perchlorate (TBAP) in acetonitrile predried by Molecular Sieves (5H). The scan is in the range of 0 to +1.5 V *vs* QRE at a rate of 100 mV/s and a step potential range of 0.005 V, unless otherwise stated. All CV scans were carried out at room temperature. **Figure 2-8** shows typical CVs of nanocrystalline, mesoporous TiO_2, Al_2O_3 films.

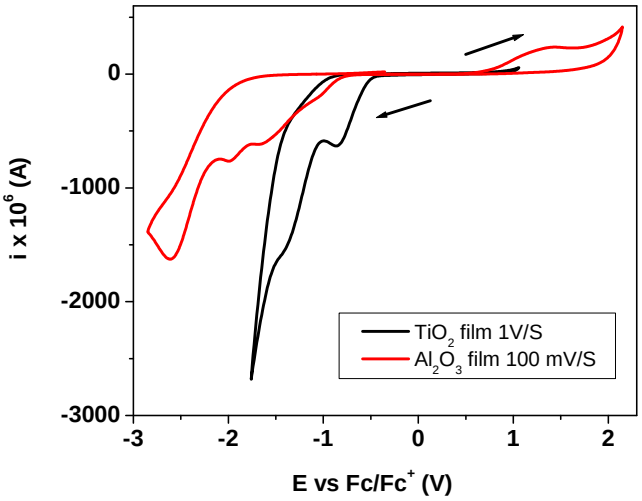

Figure 2-8. Cyclic voltammogram of nanocrystalline, mesoporous TiO_2 and Al_2O_3 films used in chapter 5. CVs were measured at scan rates of 1 V/s and 100 mV/s in acetonitrile with 0.1 M TBAP for TiO_2 and Al_2O_3 films, respectively. The initial bump of the TiO_2 film at -1V might be assigned to the filling of deep trap states[92]. The oxidation peak of Al_2O_3 film at 1V may relate to the water oxidation.

These films show a small current (<50 μA) in the range of -0.4 V to 0.8 V, which confirm their usage as insulating supporting materials for the application of redox molecules which electrical potentials lie in the centre of metal oxide bandgap. Thus, functionalisation of such films with electroactive molecular receptors or dyes can be used to investigate the lateral percolation of holes in molecular receptors or dyes across the films.

2.2.4.2 Spectroelectrochemistry

Electrochemical and in situ optical spectroelectrochemical experiments were carried out in a three-electrode spectroelectrochemical single-compartment-cell configuration (see **Figure 2-9**), which was connected to the potentiostat. The cell comprised 2.5 mL of electrolyte, sandwiched between two quartz windows. A working electrode (0.9 cm^2 dye-sensitised TiO_2 film on FTO glass for film test, FTO glass only for dye free in solution test), an auxiliary electrode (a platinum mesh flag) and a reference electrode (quasi-reference electrode (QRE) silver or platinum wire) were employed. The QRE was chosen because the aqueous Ag/AgCl (in 3.5 M KCl aqueous solution) reference electrode may introduce problems with salt leakage or junction potentials. The electrolyte contains 0.1 M TBAP in acetonitrile with and without 1 mM dye for free dye in solution and dye-sensitised films, respectively. The potential of the QRE was found to be be –0.35 V(Ag wire) and –0.4 V(Pt wire) *vs* the ferrocene/ferrocenium couple, which is in agreement with the recent report in the literature by Nazeeruddin.[93] All potentials are stated versus ferrocene/ferrocenium couple in this thesis.

Figure 2-1. Picture of the three-electrode cell.

The above three-electrode cell was incorporated in the sample compartment of a Shimadzu UV-1601 spectrophotometer and the absorption changes were monitored as a function of applied step or sweep potential. Cyclic voltammetry and cyclic voltabsorptometry (CVA, measurement of the optical absorbance as a function of

cycling potential) were conducted simultaneously with CV. CVs were obtained at a scan rate of 100 mVs^{-1}. The derivative cyclic voltabsorptometry (DCVA, dA/dE or dA/dt), the derivative of optical absorbance A with respect to potential E (or time t) at a fixed wavelength λ, is relatively free from background contributions and shows a similar shape to conventional CVs but a much cleaner signal than the corresponding CV current response. As a result, the dA/dE is related to the current, Equation 2-4, in the light of Equation 2-5 and Faraday's 1st Law of Electrolysis ($Q=zFn$).[94-96]

$$\frac{dA}{dE}=\frac{1}{\nu}\frac{dA}{dt}=\frac{1}{\nu}\frac{d(n\varepsilon\times10^3)}{dt}=\frac{1}{\nu}\varepsilon\times10^3\frac{d(\frac{Q}{zF})}{dt}=\frac{\varepsilon\times10^3}{\nu zF}i \qquad \text{(Equation 2-4)}$$

Where ν is the scan rate, V s^{-1}, z is the number of electrons participating in the redox reaction; ε is the molar extinction coefficient of dyes, M^{-1} cm^{-1}; i is the current density of a redox conversion of the molecular species, A; F stands for the Faraday constant. Consequently, the dA/dE versus E profile should exhibit a similar pattern as that of i *vs* E measured in cyclic voltammetry.

2.3 Estimation of dye loading on nanocrystalline mesoporous films

Depending on the application, nanocrystalline mesoporous metal oxide films were sensitised by different dye solutions whose solvents and concentration were varied as necessary, see each individual chapter for details. Dye-sensitised films were rinsed in acetonitrile or ethanol for 15~20 min before use, unless otherwise stated.

The dye loading on the nanocrystalline mesoporous metal oxide films was calculated by Equation 2-5, based upon the Beer-Lambert law.

$$A=\varepsilon\times\delta\times C=\varepsilon\times\delta\times[n/(0.1\times0.1\times\delta\times0.1)]=\varepsilon\times n\times10^3 \qquad \text{(Equation 2-5)}$$

Where A is the absorbance, ε is molar extinction coefficient of the dye (M^{-1} cm^{-1}), δ is the path length in cm corresponding to the thickness of the films, C is the effective dye concentration in the film which can be transformed to n, the number of moles of dye in 1 cm^2 (projected area) of film of thickness of δ (μm). Consequently, n can be

calculated using Equation 2-6. For a typical 4 um TiO_2 film sensitised with N719 dye, n is estimated to be 157 nmoles/cm^2.

$$n = A/(\varepsilon \times 10^3) \quad \text{(Equation 2-6)}$$

In addition, the surface density of surface loaded molecular receptors, Γ, can be calculated by using Equation 2-7.

$$\Gamma = n/\eta \quad \text{(Equation 2-7)}$$

Where η is the roughness factor, employing 450 for a typical 4 μm-thick TiO_2 film.

The surface area one molecular receptor or dye occupied, S_{mol}, can be calculated by Equation 2-8.

$$S_{mol} = \frac{1}{{}^s\Gamma \times N_a} \quad \text{(Equation 2-8)}$$

Where Na is Avogadro number (6.023 x 10^{23} mol^{-1}), and ${}^s\Gamma$ is the density of surface loaded molecular receptors at full monolayer surface coverage.

Thus, the dye surface coverage ($\theta = \Gamma/{}^s\Gamma$), using the value n in Equation 2-6 and the value S_{mol} in Equation 2-8, can be calculated by the Equation 2-9.

$$\theta = \frac{\Gamma}{{}^s\Gamma} = \frac{n \times Na \times S_{mol}}{\eta} \times 100 \quad \text{(Equation 2-9)}$$

2.4 Dye-sensitised solar cell

2.4.1 Cell assembly

Glass-based DSSCs were assembled in a sandwich structure by enclosing the dye-sensitised TiO_2 films with a platinised conducting FTO glass counter electrode separated by a ~25 μm Surlyn sealant (Solaronix, Aubonne, Switzerland).

Working electrode. The 1 × 1 cm^2 TiO_2 films were prepared by doctor-blading TiO_2 pastes on cleaned FTO substrates, and then sintered at 450°C for 30 min. The resulting film's porosity was estimated from mass measurements. Afterwards, a $TiCl_4$ treatment was applied to TiO_2 films by soaking them into a 80 ml 30 mM $TiCl_4$-THF aqueous solution in a glass Petri dish (covered) in oven at 70°C for 30 min, followed by a DI-water and then isopropanol rinse and leaving in air to dry (~5min) before sintering at 450°C for 30 min[97]. The post-$TiCl_4$ treatment is estimated to deposit a 1-2 nm thin TiO_2 layer on the surface of the porous film. Then, TiO_2 films were sensitised in dye solution at room temperature overnight (15~18 hours) to ensure complete surface monolayer coverage. Different dyes were dissolved in different solvents at different concentration, as detailed in each chapter. A typical N719 dye solution used in this work is 0.3 mM in a mixture of *tert*-butyl alcohol and acetonitrile (1:1 v/v).

Counter electrode. 5 mM chloroplatinic acid (H_2PtCl_6) in isopropanol solution was doctor bladed onto cleaned FTO glass in a size of 1.5 x 2.5 cm^2 with two pre-drilled holes at 1 x 1 cm^2 in diagonal in the middle. The platinised FTO glass was left to dry for 10 min under ambient conditions and then sintered at 390°C for 20 min. Fresh counter electrodes were used to assure a better cell performance.

Cell assembly. The dye-sensitised TiO_2 film (1 cm^2) was dipped and rinsed in acetonitrile for 15~20 min to remove aggregated/unbounded free dye molecules from the TiO_2 surface. Then, the solvent on films' surface was dried off with a nitrogen flow. The working electrode and the counter electrode were sealed/pressed together in X-shape using Surlyn gasket (17 x 17 mm outside and 11 x 11 square in the middle). Various electrolyte compositions and additives were used to modulate the performance of the cells. The electrolyte (2.5 µl) was injected into the DSSC via one of the two 0.4 mm holes on the counter electrode. Holes were then sealed by a cover glass (15 x 15 mm) with a piece of pre-adhered Surlyn. Once the cell was assembled, it was left overnight for equilibration. Then, the connecting edges were painted with silver paint using a cotton bud and left to dry (for 20 min) before cell characterization to reduce cell series resistance.

2.4.2 Cell I-V characterization

The current-voltage characteristics of the dye-sensitised solar cells, such as *Jsc*, *Voc*, *FF* and η, were determined by illuminating with a 150 W Xenon lamp (Sciencetech model SS150W solar simulator), equipped with an IR filter (water filter) and an AM1.5 filter (Sciencetech) which were placed in front of the cell to achieve "1 sun" substrate-electrode side (SE) and electrolyte-electrode side (EE) illumination.

Beam intensity was calibrated using a silicon photodiode with a spectral response modified to approximately match the absorption profile of the N719 dye. Current and voltage were measured and controlled using a Keithley 2400 source meter.

2.4.3 Transient measurement and charge extraction

Photocurrent and photovoltage transients and charge extraction measurements are very useful tools for understanding the transport and recombination of charge carriers in dye-sensitised solar cells (the experimental apparatus is shown in **Figure 2-10**).[98] The transient measurements were taken with the use of a pump pulse generated by an array of 1 W red light emitting diodes (LEDs) controlled by a fast solid-state switch. The duration and intensity of the pump pulse was adjusted to ensure that the perturbations were small relative to the background photovoltage or photocurrent. The quantity of charge stored within the cell under operational conditions with a particular applied voltage under light or dark conditions was estimated by charge extraction. This involves integrating the total current extracted from the cell immediately following switching the light off (if the light is on) and simultaneously setting the cell to short circuit (if the cell is not already at short circuit) using fast solid state switches. This assumes that the recombination loss during charge extraction is not significant relative to the charge extracted. The assumption appears valid in the majority of cases where the photocurrent transient time is much shorter than the photovoltage transient time. Thus, electron concentration, *n*, in the cell as a function of light intensity, voltage and current could be determined.

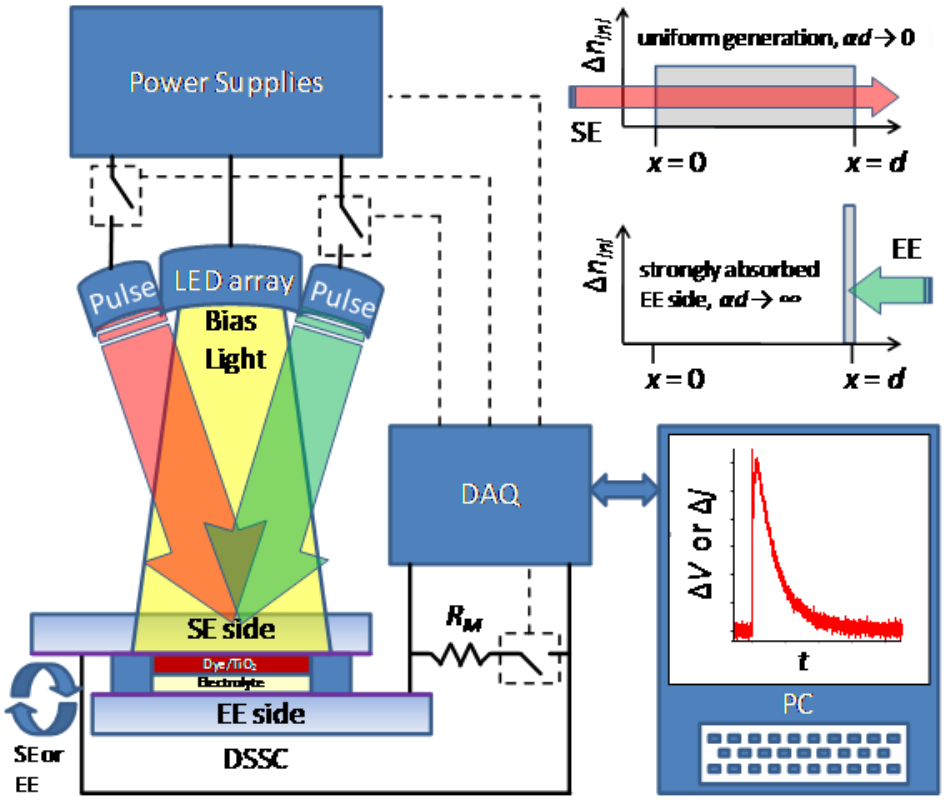

Figure 2-10. Schematic of experimental apparatus used for the collection of photocurrent and photovoltage transients and charge extraction data of a DSSC. R_M is the current measurement resistor. Illumination may be either from the substrate-electrode (SE) side or electrolyte-electrode (EE) side of the device. Also shown are idealised schematic plots (top right) of the profiles of excess electrons initially generated (Δn_{ini}) by the transient excitation pulse for two cases: uniform generation and strongly absorbed EE side illumination. Reproduced from reference [99].

Chapter 3 Functionalised Nanocrystalline Al_2O_3 Films for Optical Cyanide Sensing

The purpose of the research presented in this chapter is to demonstrate a heterogeneous optical cyanide sensor based on functionalised nanocrystalline, mesoporous Al_2O_3 films.

3.1 Introduction

Ureas and thioureas are commonly used binding groups in the development of anion receptors.[55,100] This is mainly due to the presence of relatively acidic NH groups that are well suited to form hydrogen bonding interactions with the negatively charged analytes (particularly with oxoanions, such as phosphate and sulphate). A particularly attractive anion molecular receptor contains thiourea linked to a *p*-nitrophenyl group forming a donor-acceptor molecule.[101] In such molecular receptor, the charge transfer (CT) is from the donor nitrogen of the thiourea ligand to the acceptor nitro functional group ($-NO_2$) of the *p*-nitrophenyl group.[101] This molecular receptor has shown the reversible binding to anions, such as acetate, through thiourea group, resulting in a red shift in its absorption maxima (λ_{max}). As the acetate is negatively charged, the binding of acetate to thiourea group makes the thiourea more electron donating. As such, the change transfer between the thiourea-acetate donor unit and the nitro acceptor moiety is enhanced. This reduces its HOMO-LUMO gap, leading to a red shift of λ_{max} from 340 nm to 365 nm.[101]

Of all the environmental pollutant anions, cyanide is one of the most toxic. Despite its toxicity, cyanide is widely used in the synthesis of nylon, synthetic fibres and resins as well as in gold-extraction processes, electroplating, mining and metallurgy. It also exists in cassava roots, bitter almonds and contaminated drinking water.[102] The major source of cyanide released into our environment comes from industrial waste or mining activities.[103] Cyanide is lethal to humans at concentrations of 0.5−3.5 mg per

kg of body weight.[104] This is due to the binding of this anion to iron in cytochrome oxidase which subsequently blocks the oxidative process of cells and results in damage to the brain, heart and lungs.[105] The Environmental Protection Agency (EPA) has set the maximum contaminant level (MCL) for cyanide at 0.2 ppm in order to regulate safe levels for drinking water systems.[106] Consequently, finding reliable and efficient ways of detecting the presence of this poisonous anion in water is an important challenge.

A variety of cyanide detection techniques have been previously reported, of which ion-induced changes of the optical properties (either absorption or emission) of a receptor are especially attractive.[18,88,107,108] Although some of them are very sensitive to cyanide, they are not selective, i.e. other anions (especially fluoride) usually show similar changes in optical properties which interfere with cyanide sensing. Also, most of the current cyanide sensing strategies are based on homogeneous systems. As such, they are less useful for the detection of cyanide in 'real' samples. Considering its high toxicity, it is therefore important to develop novel heterogeneous colorimetric cyanide sensors.

Current commercial cyanide detection systems include cyanide ion-selective electrodes (ELIT 8291, NICO2000 Ltd, UK) and continuous flow analyzers (Skalar, Holland). The EPA recommended method for detecting cyanide in drinking water is based on a semi-automated colorimetric sensor (EPA Method 335.4). These systems sense cyanide in low concentration ranges from 5 ppb to 260 ppm, however, they also show significant interference from anions such as Br^- and Cl^-.

In a previous study, it was shown that an anion-responsive dye (alizarin complexone) could be efficiently anchored onto mesoporous nanocrystalline TiO_2 films and used for optical sensing. This dye-TiO_2 assembly demonstrated a high selectivity for sensing fluoride and cyanide.[18] In this chapter, a new azo-phenyl thiourea compound (compound **1**)**,** shown in **Scheme 3-1**, as an anion sensor anchored onto mesoporous metal oxides is reported, and shown to have enhanced selectivity towards specific cyanide sensing. This compound was synthesized by Dr Nélida Gimeno (Imperial

College London) and full synthetic details can be found in reference[108]. Compound **1** is designed to have an anchoring group –COOH to attach it onto TiO_2, a thiourea (the binding unit) for interaction with anions via H-bonding (-NH) or soft metal cations via the sulfur-bound and azobenzene as a chromophore (the signalling unit). The thiourea ligand is a well-known group for its anion binding properties and therefore has been used as part of the anion receptors herein presented.[107] This provides a direction to modify existing organic compounds for homogeneous anion sensing to construct heterogeneous anion sensors.

Preliminary solution sensing studies in methanol and dimethyl sulfoxide (DMSO), respectively, showed that compound **1** was indeed sensitive to the presence of anionic species, and the colour changes displayed by compound **1** strongly depended on the solvent employed (shown in **Figure 3-1**).[108] In methanol, compound **1** only changes its colour in the presence of cyanide (with a limit of detection of 8 ppm) from yellow to orange/red; even when large excess of the other anions were used (5 mM), no colour changes were observed for other anions including F^-, Cl^-, Br^-, $[CH_3COO]^-$, $[H_2PO_4]^-$, $[HSO_4]^-$. In contrast, in DMSO, not only $[CN]^-$ induced a colour change (from yellow to dark purple) but also F^- (from yellow to blue), $[CH_3COO]^-$ and $[H_2PO_4]^-$ (both from yellow to violet/red).

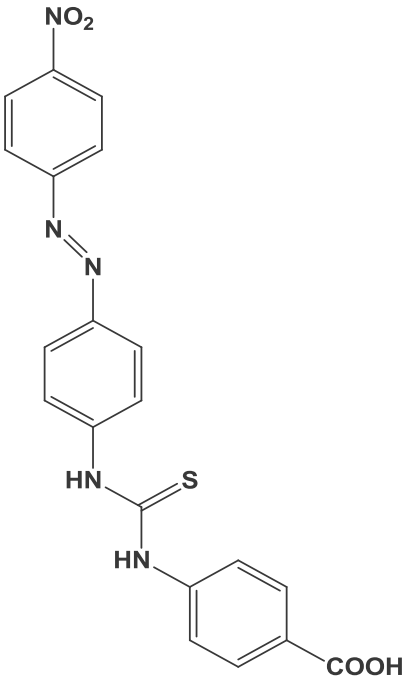

Scheme 3-1. Structures of compound **1** sensitizer.

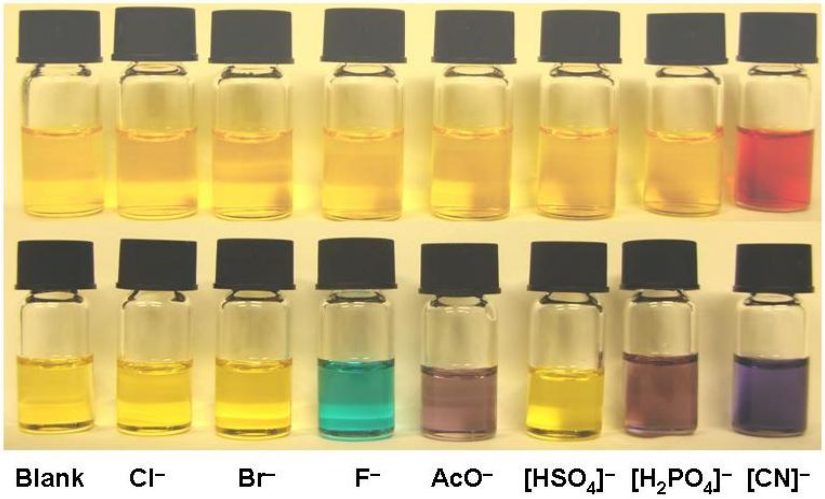

Figure 3-1. Photograph of solutions of **1** with different anions in methanol (top) and DMSO (bottom). From left to right the samples contain compound **1** plus: no anion, Cl^-, Br^-, F^-, $[CH_3COO]^-$, $[HSO_4]^-$, $[H_2PO_4]^-$, $[CN]^-$. These solution measurements were carried out by Dr Nélida Gimeno. Reproduced from reference[108].

In this study, compound **1** was anchored to nanocrystalline, mesoporous TiO_2 and Al_2O_3 films and its heterogeneous cyanide sensing was investigated. As already mentioned in 1.2.3.2, the pH of water is changed when anions dissolve in it, and pH will affect the protonation of anions if it is too acidic (forming acids), the de-protonation of the binding site (the thiourea's NH groups) and desorption of molecular receptors from the metal oxide films if it is too basic.

The pH of aqueous solutions containing cyanide or some other basic anions, are known to increase the pH of the solution, which can strongly influence the sensitivity and selectivity of the molecular receptor towards the given anion. As such, the potential pH buffer influence of the metal oxide film may play a key role in maintaining a stable sensing environment, and also in ensuring stable receptor adsorption to the metal oxide. In this regard, a comparison is made of a high PZC metal oxide film, Al_2O_3 film (PZC = 9.2[11]) versus a lower PZC metal oxide, TiO_2 (PZC = 5.5[12]). In particular, the use of **1**/Al_2O_3 films is shown to provide a promising platform for film anion sensing. It is shown, for the first time, that water insoluble receptors such as compound **1**, can be attached to Al_2O_3 films and be exposed to basic aqueous solutions of the analytes for measurement.

3.2 Experimental section

Film sensitisation. Yellow/orange **1**/TiO_2 and **1**/Al_2O_3 films for cyanide sensing were obtained by soaking TiO_2 films and Al_2O_3 films on microscope slides in 1 mM and 0.1 mM compound **1** solution in a 1:1 mixture of acetonitrile/*tert*-butanol at room temperature overnight, respectively. Dye-sensitised films were rinsed in acetonitrile for 15~20 min before sensing.

Cyanide sensing. The anions selected for the sensing studies were F^-, Cl^-, Br^-, $[CH_3COO]^-$, $[H_2PO_4]^-$, $[HSO_4]^-$ and $[CN]^-$ (as their tetrabutyl ammonium salts). The selectivity measurements were carried out by addition of 3×10^{-4} M concentration of all anions from their 2.0×10^{-2} M aqueous solutions. The titration of cyanide aqueous solution was performed into the 3 ml cuvette in the presence of **1**/TiO_2 and **1**/Al_2O_3 films. The total amount of cyanide added is much less (<0.1 ml) and the concentration factor was negligible. UV-Vis absorption spectra of **1**/TiO_2 and **1**/Al_2O_3 films were measured before and after addition of anions to detect the selectivity and sensitivity.

3.3 Results

3.3.1 Dye-sensitised TiO_2 films and cyanide sensing

Compound **1** was supported onto a TiO_2 film by immersing it in a solution of the dye, yielding an orange film with λ_{max} = 366 nm, assigned to the $\pi \rightarrow \pi^*$ transition of the 4-nitroazophenyl chromophore. From the **1**/TiO_2 film's optical density and employing a compound **1** extinction coefficient of 8,300 $M^{-1}cm^{-1}$ at 376 nm, typical **1**/TiO_2 films (2.2 μm thickness) sensitised with 0.1 mM and 1 mM solutions of compound **1** overnight were determined. The dye loadings were determined to be of 4.9×10^{16} and 8.4×10^{16} molecules per cm^2 TiO_2 film (82 nmols and 139 nmols per cm^2 TiO_2 film), respectively.

The **1**/TiO_2 films were exposed to aqueous solutions of various anions (1 mM, the same as in solution studies) and the optical changes of the corresponding film were investigated. An initial qualitative naked-eye study indicated that the film only changed colour (from yellow to a darker orange-red) in the presence of cyanide. This behaviour is analogous to that one observed for compound **1** in methanol solutions. However, a closer inspection of the system showed that in the presence of cyanide, the adsorbed dye not only changed colour, but also desorbed from the film. This was confirmed by measuring UV-Vis absorption spectra of the sensitised TiO_2 films in the presence of increasing amount of cyanide (**Figure 3-2**). The intensity of the λ_{max} band is decreased as the amount of cyanide increases. In addition, the aqueous solution in which the film was immersed turns orange, indicating the desorption of compound **1** from the TiO_2 film.

It is well established that anions in aqueous solution increase the pH of the solution. In order to use the dye-functionalised nanocrystalline metal oxide films as dip-in sensors, they need to be stable at high pH. As the PZC of TiO_2 films is pH~5[18], at high pH values its surface charge is negative, resulting in dye desorption. Therefore, at that point a basic stable metal oxide was considered to replace TiO_2 for cyanide sensing.

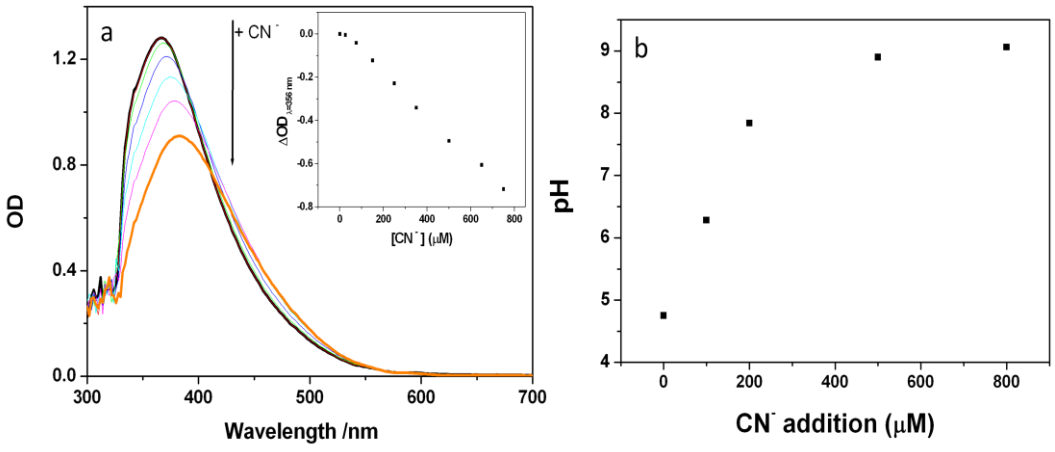

Figure 3-2 Absorption spectra of **1**/TiO_2 film upon cyanide titration. Insert is the change of optical density at 366 nm *vs* cyanide concentration.

3.3.2 pH dependence of dye-sensitised films

It is likely that the dye desorption of compound **1** from the TiO_2 film is caused by the increase in pH (more basic) of water upon addition of cyanide. In order to investigate this hypothesis, the **1**/TiO_2 films were immersed in aqueous solutions of different acidity (namely pH = 5 or 9) over a period of 20 min and the time dependence of the change of absorbance at 366 nm were monitored at room temperature using UV-Vis Spectrophotometer. As can be seen in **Figure 3-3**, a constant decrease in the optical intensity of the **1**/TiO_2 film was observed at pH 9 with time. Consequently, the **1**/TiO_2 films were not suitable for sensing anions.

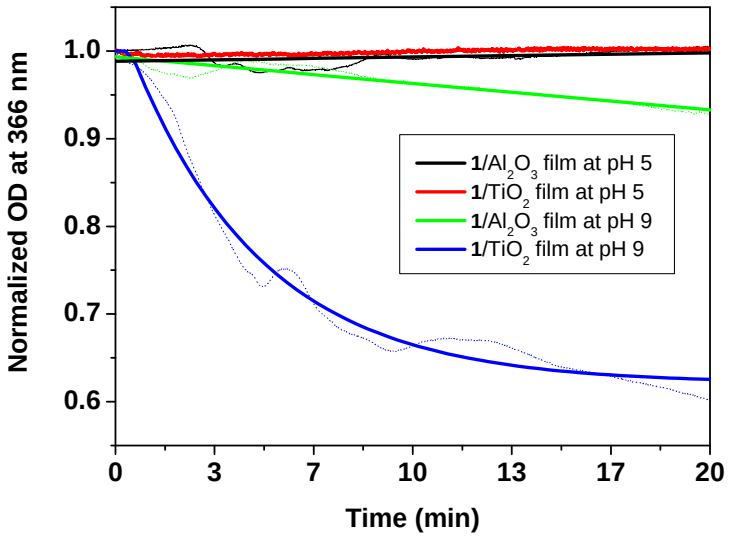

Figure 3-3. Plot showing the changes of optical density in the λ_{max} absorption for the **1**/TiO_2 and **1**/Al_2O_3 films with time as a function of pH.

Among alternative metal oxides, Al_2O_3 has a relatively high PZC resulting in stronger dye attaching to the metal oxide surface in basic solution.[109,110] This ensures the stability of nanocrystalline, mesoporous Al_2O_3 films toward anion sensing, such as cyanide sensing which can rise the pH value of aqueous solution over 9. Similar dye loading was observed for Al_2O_3 films compared to TiO_2 films. As can be seen in **Figure 3-3**, **1**/Al_2O_3 films indeed were demonstrated to be much more stable towards desorption at basic pH values even after leaving the film immersed in the basic solution for 20 minutes. Therefore, **1**/Al_2O_3 films could be investigated for cyanide sensing.

3.3.3 Anion response of 1/Al_2O_3 films

Having established the stability of **1**/Al_2O_3 films towards desorption under basic conditions, its response to different anions was studied by UV-Vis spectroscopy. The dye loading on the Al_2O_3 film was determined to be 152 nmol/cm^2.

The **1**/Al_2O_3 films were immersed in 1 mM and 5 mM aqueous solutions of different anions and the absorption spectra were recorded. In **Figure 3-4**, the immersion of the films in a 5 mM solution of cyanide cause a λ_{max} shift of the sensitised film from 366 to 406 nm. This shift was also visible by naked eye inspection of the **1**/Al_2O_3 films (see inset in **Figure 3-4**) which changed colour from yellow/orange to red/orange.

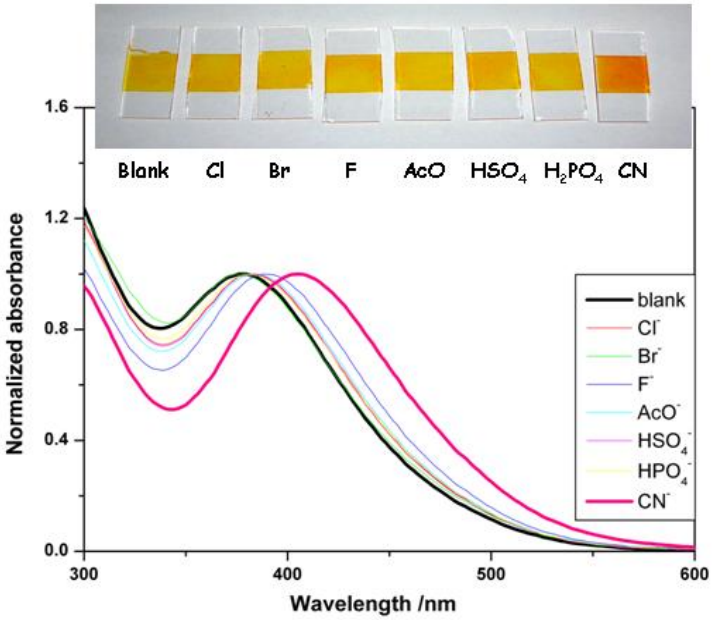

Figure 3-4. Normalized absorption spectra of **1**/Al_2O_3 films immersed in 5 mM aqueous solutions of different anions.

To establish the sensitivity of **1**/Al_2O_3 films for cyanide and the limit of detection of the system, the absorbance of the film at different cyanide concentrations was recorded, as shown in **Figure 3-5**.

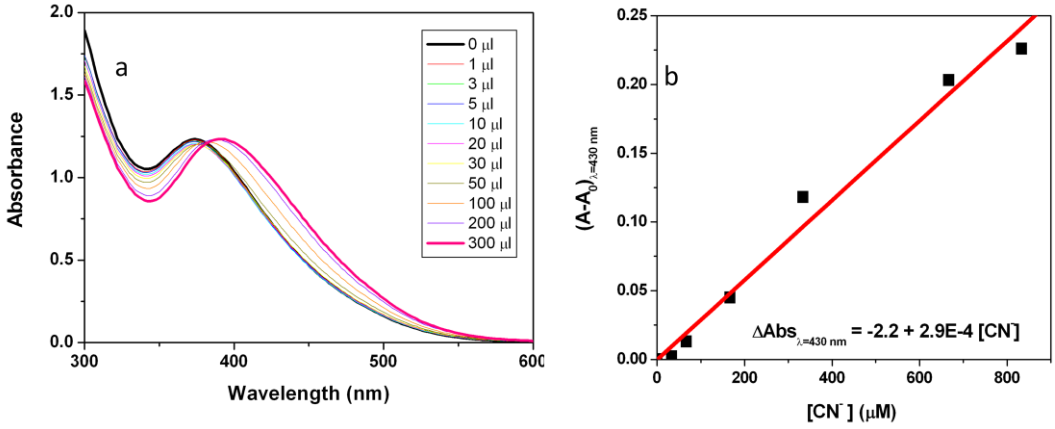

Figure 3-5. (a) Absorption spectrum shifts of a piece of **1**/Al_2O_3 film under cyanide titration in aqueous solutions at different concentrations. (b) Plotting of ΔAbs versus [CN^-].

Plotting ΔAbs versus [CN^-] **Figure 3-5**(b) gives the estimated sensitivity (namely d(ΔAbs)/d[CN^-]) as 0.3 mM^{-1} and the LOD as 0.9 ppm (using 0.01/sensitivity, which depends on the minimum change in absorbance on the instrumentation that can be reliably measured spectroscopically). Compared to available commercial systems, as mentioned in the introduction of this chapter, **1**/Al_2O_3 films show a good degree of selectivity. Although the films display a limitation of LOD, it is an easy-to-use method and will be attractive for real sample detection.

3.4 Discussion

In general, cyanide sensing studies to date have largely focused upon single phase systems, with molecular receptors dissolved in a specific organic solvent or a mixture of solvents with water solution, which is non-reversible.[88,107] The molecular receptors cannot be reused without further solution separation, are often unresponsive to cyanide in aqueous solution and are not selective. Herein, a heterogeneous cyanide sensor, based upon the adsorption of a small organic molecule to nanocrystalline, mesoporous Al_2O_3 film (as shown in **Scheme 3-2**) was developed. The **1**/Al_2O_3 film displays a colour change from yellow to orange-red upon addition of cyanide.

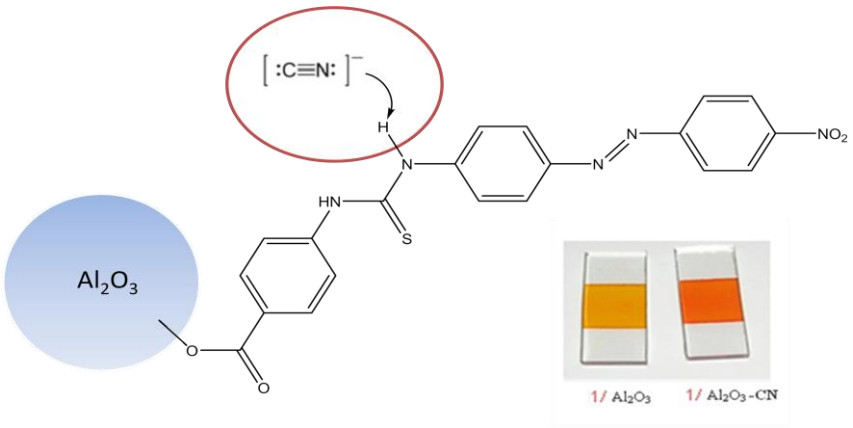

Scheme 3-2. Scheme of **1**/Al_2O_3 film in the presence of cyanide. Compound **1** undergoes deprotonation of the N-H fragments.

pH effect in anion sensing is critical because of protonation and desorption of molecular receptors. In cyanide sensing, due to the alkaline properties of cyanide ($[CN]^-$ TBA+ was chosen as HCN is extremely toxic), the pH of solution is increased upon the addition of cyanide and thus requires a high PZC nanocrystalline metal oxide as the supporting material. As Al_2O_3 is a basic stable semiconductor, it is stable in basic solution and hence was chosen for the anion/cyanide sensing studies. Additionally, due to its high bandgap (8.45~9.9 eV[11]), Al_2O_3 films show no absorption between 300 and 400 nm (see **Figure 2-6**), and is therefore background free for measuring the absorption spectrum of the **1**/Al_2O_3 film.

Regarding the sensing mechanism, solution sensing data (in DMSO) strongly suggest that the origin of the colour changes of compound **1** upon addition of cyanide, are associated to de-protonation of the thiourea's NH groups, which yields a fully conjugated species with the associated colour change.[108] It is not a simple hydrogen-bonding interaction as initially expected, but a process that involves de-protonation of the thiourea's NH groups. This is in agreement with recent reports in the literature by Fabrizzi[100,111] and Gale[62].

In the case of film, to distinguish the hydrogen-bonding interaction between compound **1** and cyanide and NH deprotonation, the UV-Vis spectra of **1**/Al_2O_3 films at different solution pH values were measured, and no changes in colour of **1**/Al_2O_3 films in the range of pH 3~9 are observed, as shown in **Figure 3-6**. The color changes

of **1**/Al_2O_3 films upon addition of cyanide are likely to be the result of a combination of hydrogen-bonding interaction and NH deprotonation.

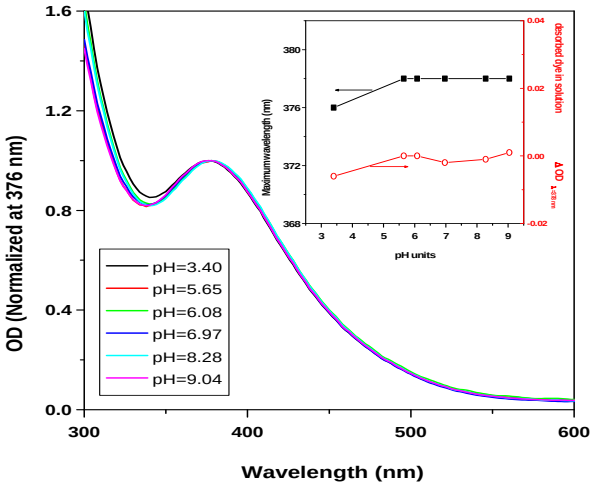

Figure 3-6. Normalized absorption spectra of **1**/Al_2O_3 films immersed in different pH solutions adjusted by adding either hydrochloric acid (HCl) or sodium hydroxide (NaOH) solution. Inset is the absorption peak of **1**/Al_2O_3 films and compound **1** desorbed in solution *vs* pH.

3.5 Summary

In this chapter, the colorimetric cyanide sensing in aqueous solutions with functionalised nanocrystalline, mesoporous Al_2O_3 films has been shown to be successful. It not only provides further evidence for the new type dip-in anion sensing method which is attractive for detecting the cyanide ions in wastewater without further treatment, but also extends the application of functionalised nanocrystalline metal oxide to anion sensing. Moreover, the detection of cyanide concentration with the sensitised Al_2O_3 films is down to 0.9 ppm.

Chapter 4 Functionalised Nanocrystalline TiO_2 Film for Mercury sensing and scavenging

The previous chapter has introduced the use of functionalised mesoporous metal oxide film for dip-in sensing and applied this methodology to cyanide sensing. The purpose of this chapter is to extend the sensing strategy to tailor the molecular materials for application in scavenging mercury from contaminated water by employing the functionalised nanocrystalline TiO_2 films with an alternative metal complex, N719.

4.1 Introduction

Cations receptors for heterogeneous cation sensing, like anions receptors, also require three units: a binding site, a signalling unit and an anchoring group. For design of cation molecular receptors, the binding site can be smaller as the cation size is smaller.

Similar to cyanide, mercury and its derivatives are acknowledged to be very poisonous metal cations. They are particularly toxic and can damage the central nervous system leading to neuropsychiatric disorders in humans.[112,113] Elementary mercury and mercury salts are released into the environment by various processes but mainly originate from the emissions of coal-fired power plants and gold mining.

Developing a chemical sensor to sense extremely low mercury concentrations down to 2 ppb in drinking water - the Maximum Contaminant Level (MCL) for mercury given by the Environmental Protection Agency (EPA) - is very difficult. Among all the published sensors, Chan et al[114] synthesised an acceptor–spacer–donor (e.g. anthracene(AN)-iminophenylmethylene-dithiocarbamate (DTC)) used as an intramolecular charge transfer emission quenching fluorescent chemical sensor

showing an estimated LOD at 10^{-8} M (2 ppb) for mercury sensing in aqueous solution; however, Ag^{+} shows similar changes which interferes with mercury sensing. Palomares et al[5] developed a novel heterogeneous colorimetric mercury sensor down to a limit of detection (LOD) at 60 ppb. The N719/TiO_2 film has been demonstrated as a novel and practical mercury sensor for the colorimetric sensing of Hg^{2+} ion in aqueous solutions at room temperature in a rapid colorimetric response, with both a high selectivity and a sub-micromolar sensitivity.[5] This is due to the binding of mercury to the –NCS ligands in N719. The structure of N719/TiO_2 film and its interaction with mercury are shown in **Scheme 4-1**, where the functionalised TiO_2 film shows a colour change from red to yellow.[88] This colour change is attributed to a transformation of the thiocyanate ligands of the Ruthenium dye induced by Hg^{2+} ions.

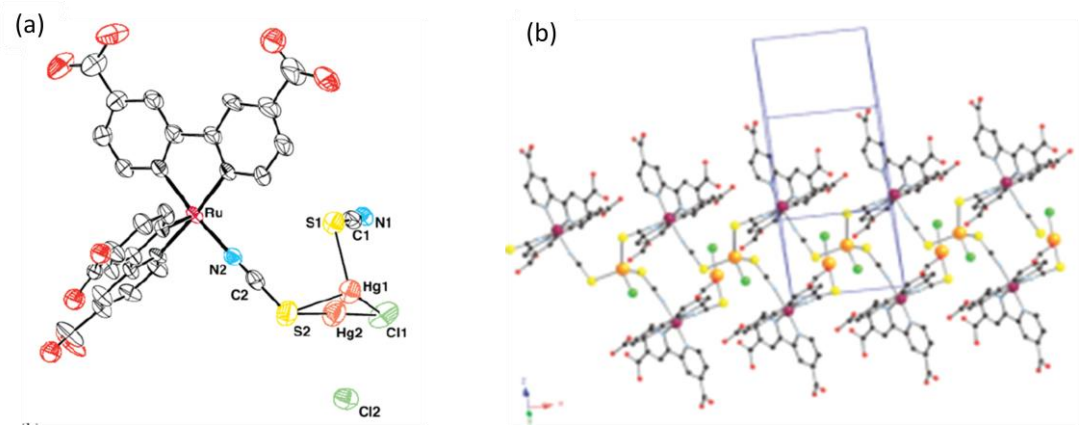

Scheme 4-1. Molecular structure of the N719-$HgCl_2$ complex. (a) The asymmetric unit which contains one mercury atom, crystallographically disordered in two positions at half-occupancy, one $[Ru(N_2C_{12}O_4H_8)_2(NCS)_2]$ complex, and two Cl^- anions. (b) A representation of the structure of the $[Ru(N_2C_{12}O_4H_8)_2(NCS)_2HgCl]_n^{n+}$ chains parallel to the axis. Reproduced from reference[88].

Despite these efforts to develop low cost methodologies to detect mercury in aqueous solutions,[5,88] the tailored design of scavenging molecular materials (SMM) to remediate environmental mercury contamination remains a key challenge.[115-120] Mercury scavenging materials should accomplish several general requirements: (1) they have to be efficient at scavenging low concentrations of mercury; (2) they have to be cheap and easily prepared on a multi-gram scale; and (3) they should be reversible so that they are reusable. To date, published mercury scavenging methods include chemical bonding by organically modified mesoporous materials,[116,117] adsorption by hydrous manganese oxides,[118] binding to dietary fibre from wheat

bran,[119] modified adsorbents containing vicinal sulfur or thiol groups,[120] photocatalysis,[121] solar irradiation with hydrogen peroxide,[122] sulfur-impregnated materials, activated carbons[123] and scavenging leeches.[124] However, these methods present several limitations. For example, neither hydrous manganese oxides nor dietary fibre adsorptions have high selectivity towards mercury. Although this problem has been solved by the use of modified adsorbents containing vicinal sulfur or thiol groups, the materials employed cannot be regenerated and their use generates further waste products that must be compressed, encapsulated, and buried.[120] Other alternative methods such as the photocatalytic removal of mercury ions from waste water using UV irradiation[121,122] are unfavourable energetically.

In this chapter, a new method for mercury scavenging is proposed. It consists of the use of a dye functionalized mesoporous, nanocrystalline TiO_2 film to perform efficient and selective mercury scavenging from mercury-contaminated aqueous solutions.

4.2 Experimental section

4.2.1 Film sensitisation

The N719 complex was adsorbed onto the 1 cm^2 TiO_2 films by soaking the film in a 1 mM solution of the dye in a 1:1 mixture of acetonitrile: *tert*-butanol at room temperature overnight. The N719/TiO_2 films were rinsed in ethanol for two hours prior to the mercury scavenging experiments.

4.2.2 Mercury scavenging studies

The pH of the tested solutions were fixed using HEPES ([N-(2-hydroxyethyl)piperazine-N9-(2-ethanesulfonic acid)]) buffer (pH = 6.6). The mercury scavenging experiments were performed by dipping the N719/TiO_2 film (1 cm^2 projected area) in different mercury concentration aqueous solutions ranging from 1 to

30 μM for 10 minutes to ensure optimum scavenging of mercury. Either Inductively Coupled Plasma-Atomic Emission Spectroscopy (ICP-AES) or the N719 molecule were used to measure the mercury concentration present in the aqueous solution after removing the scavenging film. All the experiments were repeated three times to average the results and ensure reproducibility.

Determination of the scavenged mercury by the mesoporous N719/TiO_2 film. In order to quantify colorimetrically the mercury remaining in the solution, after the scavenging process, a 12.5 μl from 2 mM N719 stock solution in ethanol was added to 1 ml of the mercury aqueous solution (in 8 vials) in range from 1 to 30 μM and the UV-Vis spectrum of the mixture was measured. 10 mM HEPES buffered aqueous solution chosen for blank experiment.

Competitive scavenging. The mercury scavenging properties of the N719/TiO_2 film in the presence of other water-soluble metal salts were studied using ICP-AES (Varian Vista-ProE, Natural History Museum, London, UK).

Reversibility of the scavenging film. The N719/TiO_2 film was first exposed to a 5 mM $HgCl_2$ aqueous solution; this interaction results in a colour change from red–purple to orange (due to the interaction of the Hg^{2+} cation with the NCS groups of N719[88]). The orange film was subsequently dipped into a 10 mM solution of HEPES buffered KI (pH=6.6) solution. This generated a colour change of the film back to the red–purple colour characteristic of the N719/TiO_2 film before exposing it to Hg^{2+} ions. When the film was subsequently dipped again into the $HgCl_2$ solution, the colour of the film changed back to orange. This procedure can be repeated several times demonstrating that the supported dye can be re-utilized by dipping it into an iodide solution.

Reusability of the scavenging film. The reusability studies of the scavenging film were carried out by dipping the N719/TiO_2 film into a mercury aqueous solution first and regenerating the film in a KI solution, and then re-dipping into the mercury aqueous solution again. Four 1 cm^2 N719/TiO_2 films were first exposed to a series of

12 μM $HgCl_2$ aqueous solutions for 10 minutes each; the resulting orange film was subsequently dipped into a 10 mM KI solution.

4.3 Results

4.3.1 Optical Mercury Sensing

To assay the scavenging of mercury ions from aqueous solutions, *i.e.*, to calculate the change of mercury concentration before and after the film scavenging, two optical absorbance sensing strategies were employed. The optical absorbance measurements are both based upon the blue shift of the metal to ligand charge transfer band (MLCT) of the N719 dye resulting from its complexation with mercury ions. One strategy is based upon monitoring the absorbance of the dye adsorbed onto the nanocrystalline mesoporous TiO_2 films, as in previous report.[5] This heterogeneous film based sensing strategy, the same optical sensing methodology as that for cyanide sensing in previous chapter, can be used to quantify directly the moles of mercury adsorbed on the N719/TiO_2 film. The second strategy is based upon the addition of a concentrated stock solution of the N719 dye to the aqueous solutions of mercury ions, followed by determination of the optical absorption spectrum of this dye. This second, homogeneous solution based sensing strategy could monitor the concentration of mercury in solution before and after the scavenging process.

Homogeneous solution based sensing. The optical absorbance changes of the mixture of mercury and addition of N719 dye solution at different mercury concentration were recorded and the linear fit of the experimental data gives a calibration equation (Equation 4-1) that relates the changes of optical density of N719 upon mercury binding to the N719 molecules in solution, as illustrated in **Figure 4-1**.

$$R = 1.76 - 0.03 * [Hg^{2+}] \qquad \text{(Equation 4-1)}$$

where $R = \frac{Abs_{\lambda 1}}{Abs_{\lambda 2}}$, λ_1 = 508 nm (maximum absorbance in the absence of Hg^{2+} ions) and λ_2 = 438 nm (maximum absorbance in the presence of Hg^{2+} ions). This N719

ethanol solution, similar to the N719/TiO_2 film, allows the detection of mercury at levels of about 20-50 ppb and exhibits a selective sensing to mercury (**Figure 4-2**).

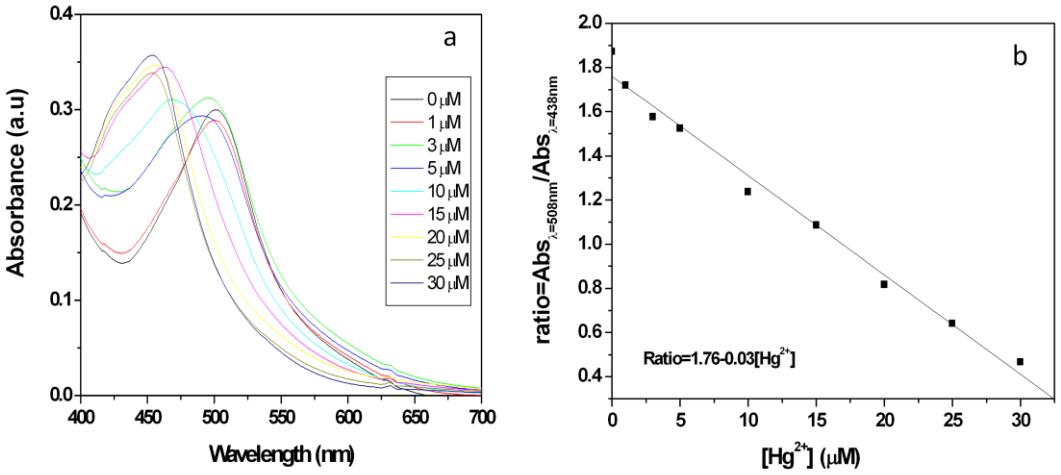

Figure 4-1. (a) The absorption spectra of a mixture of N719 ethanol solution (12.5 μl 2 mM) and $HgCl_2$ aqueous solutions (1 ml 0 ~ 30 μM); (b) Calibration curve for the N719 solution chemical sensor (in ethanol).

Figure 4-2. Color changes observed by "Naked Eye" at 12.5 μM M^+ ions (for Hg^{2+} is 2.5 ppm) aqueous solution as 2 mM N19/ethanol solution added. From left to right: No metal ions, $+Hg^{2+}$, $+Ca^{2+}$, $+Mg^{2+}$, $+Fe^{3+}$, $+Fe^{2+}$, $+Cd^{2+}$, $+Cu^{2+}$, $+Co^{2+}$, $+Ni^{2+}$, $+Pb^{2+}$, $+Zn^{2+}$, $+Li^{+}$.

Comparison of homogeneous solution-based sensing to film sensing. Figure 4-3 compares data collected for film sensing (■) and solution sensing (○) as a function of mercury concentration in aqueous solution. Both the solution and film sensing data show saturation at high mercury concentrations, indicative of saturation of the N719 mercury binding sites. The solid lines which correspond to the film and solution sensing data show the fit to a Langmuir adsorption isotherm, Equation 4-2, modified form of Equation 1-14.

$$\theta = \frac{\Gamma_{Hg}}{\Gamma_{Hg(S)}} = \frac{K_f[Hg(II)]}{1+K_f[Hg(II)]} \qquad \text{(Equation 4-2)}$$

where θ is defined as the fractional occupancy mercury binding sites on the N719/TiO_2 film, Γ_{Hg} is the density of adsorbed mercury (moles per film cm^2) and $\Gamma_{Hg(S)}$ is of the density of adsorbed mercury at saturation, [Hg(II)] is the concentration of mercury ions in solution after equilibration with the film and K_f is the mercury binding constant. The optical response is assumed to be directly proportional to θ. From these data, the film mercury binding constant is determined to be 3 x 10^5 M^{-1}. Analogous analysis of the solution data yield a solution-binding constant K_S ~ 1 x 10^5 M^{-1} within the same order of magnitude. For the control experiments, N719/TiO_2 films were immersed into distilled water, which results in θ equals to zero when mercury is not present in solutions, and θ equals to 1 when the N719/TiO_2 film is immersed in a mercury solution at saturating concentrations and the colorimetric response reaches a plateau. Equation 2-6 converts the film optical response shown in **Figure 4-3** into nanomoles of Hg^{2+}. Obviously, at high mercury concentrations, a single N719/TiO_2 film of 1 cm^2 removes 23 nanomoles of Hg^{2+}.

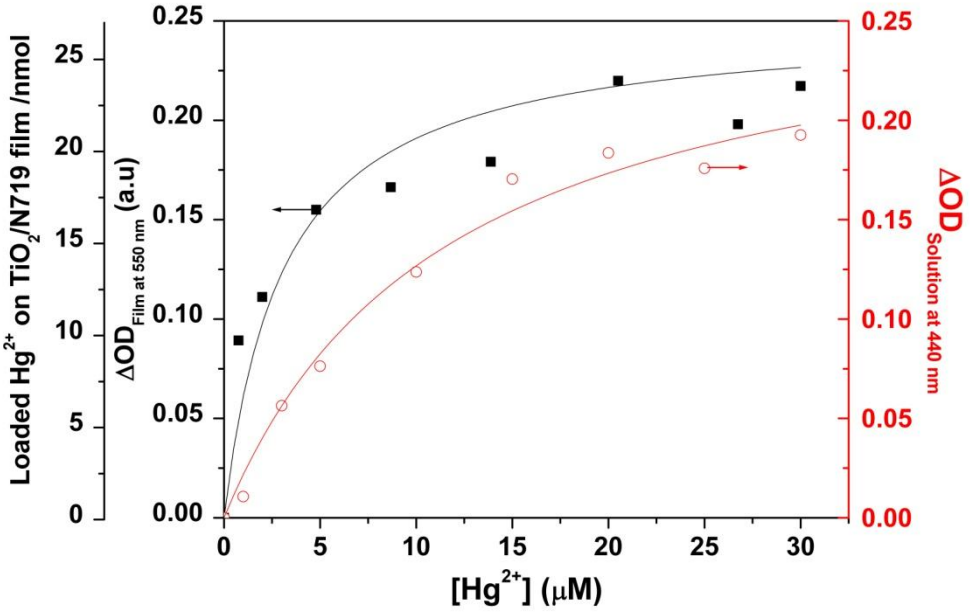

Figure 4-3. Typical data collected for heterogeneous sensing (**film,** ■) and homogeneous sensing (**solution,** ○) as a function of mercury concentration in aqueous solution. Solid lines are numerical fits to **Equation 2.3**, the correlation of estimated mercury loaded on the 1 cm^2 N719/TiO_2 film to mercury concentration (**black**) and binding mercury to N719 in solution (**red**).

4.3.2 Scavenging efficiency

To assess the scavenging processing, the scavenging efficiency (η_{MSE}) is defined as the percentage reduction in mercury concentration achieved by this scavenging procedure specified in Equation 4-3.

$$\eta_{MSE}\% = \frac{C_0 - C}{C_0} * 100\% = \frac{\theta^S \Gamma_{Hg} A}{[Hg(II)]_0 V} * 100\% \qquad \textbf{(}\text{Equation 4-3}\textbf{)}$$

Where C_0 and C are the mercury concentrations in solutions before and after N719/TiO_2 films scavenging, in parts per million (ppm) units.

A series of N719/TiO_2 films were immersed into several aqueous solutions with known mercury concentrations for 10 minutes. This scavenging should correlate directly with the moles of mercury adsorbed to the N719 functionalised nanocrystalline, mesoporous TiO_2 film, as inferred from the film sensing studies above (4.3.1) and detailed in Equation 4-3, that take into account the volume of mercury aqueous solution (V) and area of the TiO_2 film (A). Typical experiments use V = 4 cm^3 and A = 1 cm^2. The scavenging efficiency was obtained by measuring the mercury concentration in the solutions before and after the scavenging process, using the homogeneous solution sensing strategy. The results are depicted in **Figure 4-4**.

The solid red line in **Figure 4-4** shows the mercury scavenging efficiency determined from the mercury adsorbed onto the N719/TiO_2 film. An excellent agreement is obtained between the mercury concentration measured after the scavenging process using the homogeneous sensing strategy and the η_{MSE}, as illustrated in **Figure 4-4**. For the control experiments, the same nanocrystalline mesoporous TiO_2 film without the N719 dye was employed. The immersion of such ‘‘naked-films’’ in the mercury samples did not induce any change in the mercury concentration, indicating that the scavenging function of the N719/TiO_2 films is specifically derived from the mercury binding properties of the sensitizer N719 dye.

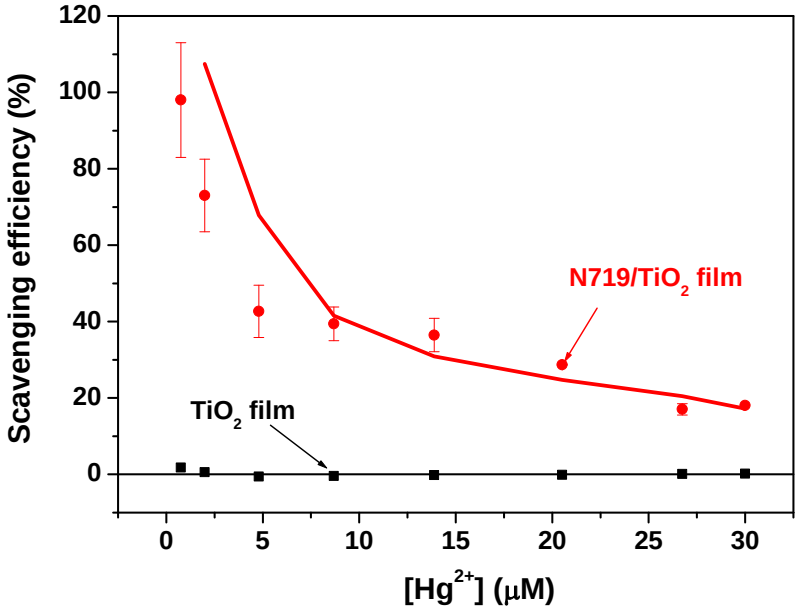

Figure 4-4. Scavenging efficiency for a 4μm thick mesoporous N719/TiO_2 film (●) and control TiO_2 film (■) in different aqueous solutions of mercury. The solid red line corresponds to the predicted scavenging efficiency using Equation 4-3.

The Environmental Protection Agency (EPA) considers 2 ppb as the maximum contaminant level goal in drinking water.[125] The N719/TiO_2 films show higher efficiency for the scavenging process in solutions containing less than 400 ppb of mercury (2 μM), which are closer to real measured mercury contaminated samples.[126] It can be seen in **Figure 4-4** that while at higher mercury concentrations, the η_{MSE} decreases, as the number of available mercury binding sites becomes saturated. Under this saturating condition, the N719/TiO_2 films adsorb ~23 nanomoles of Hg^{2+} taking into account that each TiO_2 film has a loading capacity for N719 of 157 nanomoles per cm^2 (projected area) film. The results clearly indicate that N719/TiO_2 films are an effective mercury scavenging system for the wide range of mercury concentrations that are typically found in the environment.

4.3.3 Selectivity of the scavenging film

As mentioned in the introduction, a desirable scavenging system needs also to be both selective and reversible. It has previously been demonstrated that the optical response

of N719/TiO_2 film is specific to the presence of mercury ions, and insensitive to all other metal cations identified by the EPA as water pollutants at the same concentration. Herein, ICP-AES measurement is chosen to study the selectivity of the N719/TiO_2 films as well. This well-known technique can measure the concentration of different metal ions present in solution before and after the scavenging process and validate the selective scavenging measurements. The experimental results are shown in **Table 4-1**. The mercury scavenging efficiency determined from ICP-AES data is 64.9%, which is similar to the result obtained using the colorimetric method (72% for 2.5 μM Hg^{2+} in **Figure 4-4**). This efficiency is significantly higher than that of the other metal ions (at least four times higher) indicating the film's capability for mercury scavenging even in the presence of other common metal ions in the solution. This is a very important issue towards the development of mesoporous hybrid materials to prevent mercury contamination. However, the scavenging efficiency of the soft metal ions, such as lead and copper, is bigger than the other ions due to the interaction with the soft sulfur atoms of N719. For the hard metal ions, such as lithium, they also show some scavenging which may be due to adsorption onto the TiO_2 surface.

Table 4-1 Selectivity of Mercury Scavenging

Cation	**Hg^{2+}**	Pb^{2+}	Cd^{2+}	Cu^{2+}	Zn^{2+}	Mg^{2+}	Fe^{2+}	Co^{2+}	Li^{2+}	Mn^{2+}	Ni^{2+}
Scavenging efficiency, %	**64.9**	16.2	4.7	16.4	4.4	2.7	7.9	2.9	7.4	1.7	3.1

[a] A 4μm thick N719/TiO_2 film was immersed 10 minutes into a solution containing all the cations (2.5 μM) above indicated.

4.3.4 Reversibility of the scavenging film

The reversibility of the scavenging N719/TiO_2 film is one of the most critical issues for the development of a low cost mercury scavenging system. **Figure 4-5(a)** illustrates the reversibility of the scavenging process. A cheap iodide salt was used to remove the adsorbed mercury from the scavenging film. Typically, a single N719/TiO_2 film was immersed into a vial containing 5 μM mercury aqueous solution. After removing the film, the mercury concentration was measured and it was found to

be in a range between 0.5 and 1 μM, confirming the scavenging process. The same film was reused four times using a 10 mM KI solution as the regenerating agent. In all cases, the mercury concentration was kept the same and the final mercury concentration was found to be 1 μM, indicating that the scavenging N719/TiO_2 films can be reused at least four times retaining their scavenging properties. It is believed that the iodide salt is likely to be involved in the formation of a stable mercury iodide complex that displaces the mercury from the N719 environment. The mercury iodide salts can be easily recovered as a solid precipitate by adjusting its solubility, by either changing the solvent or changing the solution pH.

Further to prove the reusability of the scavenging film, a single N719/TiO_2 film was dipped into a 4 ml 12 μM solution of mercury four consecutive times. Each time, the scavenging film was reversed using the potassium iodide solution (10 mM). The results, shown in **Figure 4-5(b)**, demonstrated that the efficiency of the scavenging process was increasing linearly with the number of reversible cycles. This is in agreement with the fact that at lower mercury concentrations, the scavenging efficiency of the scavenging film increases as observed in **Figure 4-4** where at low mercury concentrations the η_{MSE} was ~80%.

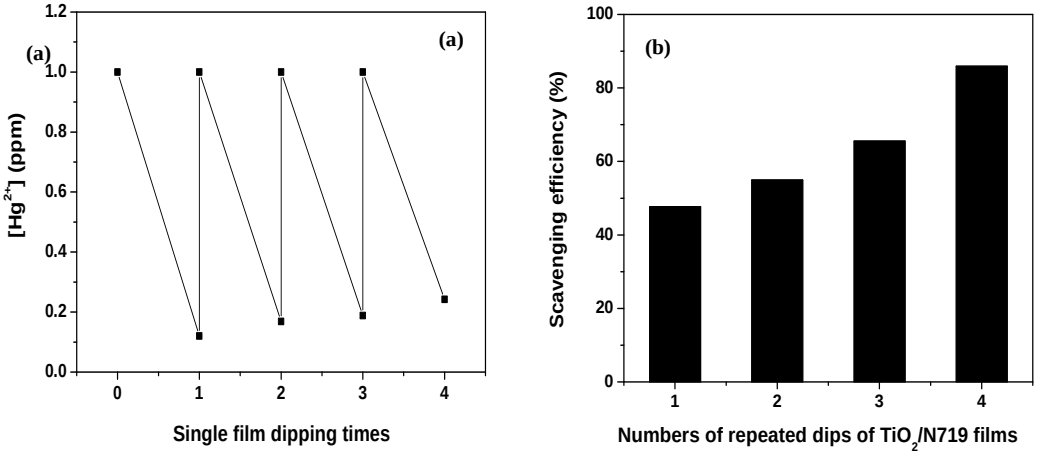

Figure 4-5. (a) The reversibility of the mercury scavenging process using a 4μm thick N719/TiO_2 film. The mercury concentration was 5μM. (b) Relationship between mercury scavenging efficiency and numbers of repeated dips of N719/TiO_2 films in a 12 μM aqueous solution of mercury.

4.4 Discussion

Due to the extreme toxicity of mercury, it is harmful to our environment (for example, water contamination reduces the fish population) and human health (neuropsychiatric disorders). Therefore, designing and developing mercury scavenging molecular materials (SMM) is very important and useful in removal of mercury from our environment to prevent environmental pollution. The key challenge in designation of SMMs is that it should be regenerated and re-useable.

The SMM developed here employing metal complex functionalised nanocrysatlline, mesoporous TiO_2 films ($N719/TiO_2$ films) shows scavenging mercury in aqueous solutions for a practical approach of mercury removal from contaminated water. The $N719/TiO_2$ film has been demonstrated as a novel and practical mercury sensor for the colorimetric sensing of Hg^{2+} ion in aqueous solutions at room temperature in a rapid colorimetric response, with both a high selectivity and a sub-micromolar sensitivity.[5] One of the possible interactions between the $N719/TiO_2$ film and mercury is shown in **Scheme 4-2**, where the functionalised TiO_2 film shows a colour change from red to yellow. This colour change is attributed to a transformation of the thiocyanate ligands of the Ruthenium dye induced by Hg^{2+} ions.

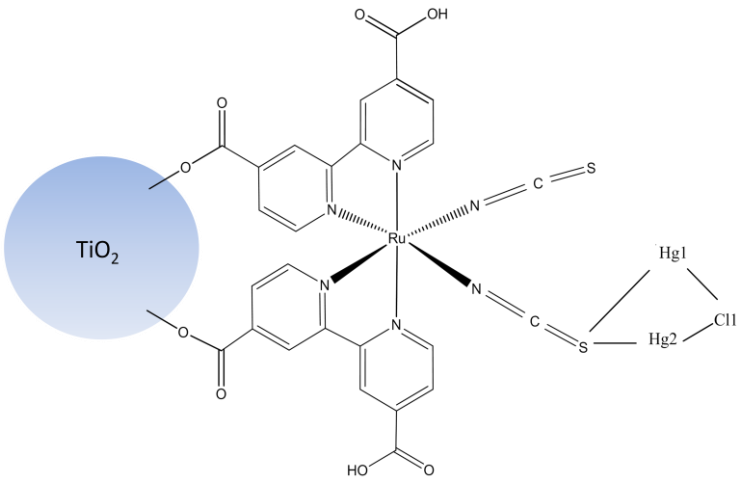

Scheme 4-2. One possible binding of mercury to N719 adsorbed onto TiO_2 film.

The $N719/TiO_2$ film is an ideal mercury scavenging material and overcomes all the limitation of current scavenging methods. It is highly selective to mercury compared

to the adsorption of hydrous manganese oxides[118] and dietary fibre.[119] Hydrous manganese oxide (MnO_2) suspensions scavenges mercury by adsorption of the uncharged $Hg(OH)_2$ and $HgCl_2$, and dietary fibre contains phytic acid which binds to heavy metals. Both of them also bind to other cations, such as rare metals (to MnO_2), Zinc and calcium (to phytic acid). In addition, unlike reported SMMs modified by vicinal sulfur or thiol groups, dye N719 functionalised metal oxide films can be regenerated and reused, and no further waste produces are generated. For example, it can be easily regenerated by dipping it into KI solution to form more stable mercury salt HgI than Hg-N719 complex. As it is operated under ambient condition at room temperature, it is energetically more favourable compared to photocatalytic removal of mercury ions[121,122]. Besides, it not only shows high scavenging efficiency at low mercury concentrations, but also shows high selectivity towards mercury ions. It selectively binds to mercury even in a high concentration of interfering cations. Its reversibility and fast response to mercury in which colour changes can be observed by 'naked eye' make it feasible in mercury scavenging overcoming all the reported SSMs' limitations. Additionally, it can be used at least four times retaining more than 80% of the scavenging activity towards mercury even in the presence of other metal ions. Furthermore, the scavenging data can be fitted with analytical equations to estimate the film mercury ion binding constant to the N719 molecules quantitatively.

4.5 Summary

Based upon the concept of applying functionalised nanocrystalline metal oxide films in real sample sensing such as mercury sensing[5] and cyanide sensing (results shown in Chapter 3), in this chapter, studies have been extended to scavenging toxic ions in aqueous solution. From the results in this and the previous chapters, the functionalised nanocrystalline mesoporous metal oxide films have exhibited multipurpose properties for heterogeneous sensing and scavenging by varying the functional ligands in the anchored molecules. These studies could lead to a new direction for developing novel colorimetric ions sensors and scavenging materials for toxic ions and broadening the scope of application of nanocrystalline mesoporous metal oxide films.

Chapter 5 Spectroelectrochemical Studies of Cation Percolation on Functionalised Nanocrystalline TiO_2 Films: Towards Voltammetric Mercury Sensing

Functionalised nanocrystalline metal oxide films have been reported in the past two chapters for cyanide sensing, mercury sensing and mercury scavenging in aqueous solutions. In this chapter, similar structured electroactive ruthenium complexes are considered to develop voltammetric sensors for sensing mercury via dye cation/hole percolation. This percolation moreover potentially enables dye/TiO_2 films to function in applications of the molecular wiring of wide bandgap inorganic materials for hole percolation in batteries, molecular nanotransistors and sensing.

5.1 Introduction

In chapter 4 and in previous studies[5,88], the selective binding of mercury ions to the -NCS ligands in Ru-complexes such as N719 has been demonstrated. Similar to the chemical structure of the N719 dye, a hydrophobic ruthenium complexes N621 (*cis*-di(thiocyanato)(2,2′-bipyridyl-4,4′-dicarboxylic acid)-(2,2′-bipyridyl-4,4′-tridecyl) ruthenium(II)) and an analogous donor-acceptor dye HW456 (*cis*-di(thiocyanato)(2,2′-bipyridyl-4,4′-dicarboxylic acid)-(2,2′-bipyridyl-4,4′-bis(vinyltriphenylamine) ruthenium(II) (dye structure shown in **Scheme 5-1**) are also containing two –NCS ligands, which is supposed to interact with mercury. As these two dyes are electroactive, the binding to mercury of these two dyes may extend the heterogeneous sensing strategy from optical to electrochemical (percolation sensing) by either quenching or accelerating the electrochemical signal under bias. Also in this chapter, the application of spectroelectrochemical techniques to compare the hole

percolation dynamics of molecular networks of these two ruthenium bipyridyl complexes adsorbed onto mesoporous, nanocrystalline TiO_2 films are investigated.

5.1.1 Percolation sensing

The fabrication of functionalised metal oxide films on conducting substrates such as FTO with metal complexes or organic compounds allows the application of positive potentials sufficient to oxidise electroactive molecules (herein corresponding to dye molecules) adjacent to the FTO substrate. The subsequent percolation of dye cations (or 'holes') via two-dimensional hopping across the molecular network can be observed when the dye surface coverage exceeds a percolation threshold. Below this threshold, the dye molecules are disconnected. This concept can be used to sense cations or anions which bind to these dye molecules, at or above the percolation threshold, *i.e* addition of cations/anions in the solution with dye-sensitised metal oxide films can potentially change the hole/dye cation percolation, as monitored through cyclic voltammetry (CV) and spectroelectrochemical measurements.

Nazeeruddin, et al[93] has reported that the addition of mercury ions affects the CV shape and anodic peak current of N621/TiO_2 films at full dye surface coverage. Wang et al[127] also reports that the sulfur *p*-orbitals in Z907 dye molecules undergo strong binding with mercuric ions, preventing their participation in the intermolecular electron exchange and blocking the cross surface hole transfer process. This suggests that hole percolation can be suppressed by adding mercury at or above the percolation threshold of both N621 and Z907 sensitised nanocrystalline metal oxide films. In this chapter, these studies are further extended to investigate the sensing selectivity and sensitivity of both N621/TiO_2 and HW456/TiO_2 films to mercury ions by means of spectroelectrochemical measurements. The sensitivity and the LOD of mercury ions can be obtained via relating the oxidation potential (the anodic peak current from the CV measurement) of the two dyes to the mercury concentration in organic solutions.

5.1.2 Kinetics of dye cation/hole percolation

The kinetics of the hole percolation process are critical to potential device applications. These kinetics are of potential importance not only to the sensing function discussed above but also to the function of dye-sensitised nanocrystalline solar cells (DSSCs), where such percolation processes may result in the transport of dye cations across the sensitised TiO_2 surface prior to regeneration by the redox electrolyte. Bonhôte, et al[17] studied a phosphonated triarylamine anchored to a nanocrystalline TiO_2 film which demonstrated cation/hole transport across the adsorbed amine layer, with a percolation threshold of ~50% of a full monolayer coverage. Meyer, et al[128] extended such studies to osmium bipyridyl complexes adsorbed to TiO_2 films. Papageorgiou, et al[16] observed the lateral electron transport across a monolayer of derivatised fullerenes bound on nanocrystalline ZrO_2 film, whilst more studies have focused on ruthenium bipyridyl dyes[85,127,129] and organic dyes[130]. However, all these molecules show a lower cation diffusion coefficients D_{app} (of the order of 10^{-8}~10^{-9} cm^2/s), which can be monitored by chronoabsorptometry and estimated by fitting the experimental data quantitatively using a modified version of the Cottrel equation[131] given by **Equation 5-1** (see Appendix 1 for details).

$$\Delta OD(\lambda,t) = \frac{2\Delta OD_f}{d}\sqrt{\frac{D_{app}t}{\pi}} \qquad \textbf{(Equation 5-1)}$$

Here ΔOD is the absorbance change at time t and ΔOD_f is the total absorbance change; the film thickness d is 4 μm in this study.

To date, the correlation between molecular structure and the dynamics of cation/hole percolation has only received limited attention. In this chapter, the percolation dynamics for two ruthenium bi-pyridyl complexes with and without the inclusion of a tri-phenyl amine (TPA) electron donating group is compared.

5.1.3 Donor-acceptor dyes

Donor-acceptor dyes have been shown to be attractive sensitiser dyes for DSSCs, due both to their high molar extinction coefficients (> 2 x 10^4 M^{-1} cm^{-1}) and their potential

to generate remarkably long-lived photoinduced charge separation at the dye/metal oxide interface.[132,133] By introducing a π-electron donor, such as TPA, into the dye structure, the positive charge or 'hole' is shifted on to this moiety, potentially increasing the distance between the dye cation and the metal oxide surface, and thus retarding the interfacial charge recombination dynamics (Equation 1-4). One such dye is HW456, which has shown good device performance in both solid state and liquid electrolyte DSSCs.[134,135] In this study, the performance of HW456 is compared with that of a control dye, N621, where the TPA electron donating groups are replaced by alkyl chains. Both the HW456 and N621 dyes adsorbed strongly to nanocrystalline, mesoporous TiO_2 films due to the presence of their carboxylic acid groups. This chapter focuses on the impact of the different donor substituents on the dynamics of hole percolation when these dyes are adsorbed to nanocrystalline, mesoporous TiO_2 films.

From the CV data, the oxidation potentials of the two ruthenium (II) dyes considered in this chapter both lie in the centre of the TiO_2 bandgap, which the TiO_2 film functions only as an insulating supporting material. Functionalisation of such films with these dyes thus can be employed to study the lateral percolation of holes across the adsorbed molecular film.

5.1.4 Spectroelectrochemistry

Spectroelectrochemistry, which combines electrochemical perturbation of an optically transparent electrode with simultaneous optical absorption monitoring, has been successfully applied to provide remarkably detailed information about the mechanism of both homogeneous and heterogeneous electrochemical reactions.[6,94,136] These techniques (detailed in 2.2.4.2) allow the molecular species of interest to be optically monitored directly. One such technique is cyclic voltabsorptometry (CVA), which can be carried out simultaneously with cyclic voltammetry at a fixed wavelength (normally λ_{max}) to monitor the changes of optical density of dyes as a function of cycling potential. The derivative cyclic voltabsorptometry signal (DCVA, dA/dE in Equation 2-4) is similar to the CV, but background free. DCVA has been employed to

investigate the redox processes of proteins adsorbed to nanocrystalline metal oxide films[6], rutin[137] and conducting polymer films such as polyaniline[138,139], poly(3,4-ethylenedioxythiophene)[140] and poly(3,4-dimethoxy-thiophene)[141]. In addition, potential step absorption spectroelectrochemistry techniques, such as chronoabsorptometry, has been intensively utilized to study lateral electron/hole transport in electroactive species and has proven to be a useful technique for the determination of heterogeneous electron transfer kinetic parameters, such as the reaction rate and diffusion coefficients.[17,127]

In this chapter, spectroelectrochemical techniques have been employed to monitor the electroactivity and hole percolation dynamics of both N621/TiO_2 and HW456/TiO_2 films. The dependence of these percolation dynamics upon the presence of mercuric ions is used to provide further insight into the different mechanisms of hole percolation between these two molecules. Additionally, as the cation percolation exists in DSSCs and the effect of the cation percolation on the cell performance remains unclear, the kinetics of the cation percolation is further analysed in order for comparison with the kinetics of ground state regeneration of the dye in DSSCs. It is hoped that these results are useful to enable the dye/TiO_2 films in applications of the molecular wiring of wide bandgap inorganic materials for percolation batteries, molecular nanotransistors and sensing.

5.2 Experimental section

5.2.1 Film sensitisation

Nanocrystalline mesoporous TiO_2 and ZrO_2 films were prepared following the procedure in 2.1, and then sensitised in dye solutions in the concentration range of 0.02 - 2 × 10^{-4} M in 1:1 (v/v) acetonitrile and *tert*-butanol solution for N621 and chloroform for HW456 for two days, with the final dye loading depending upon the solution concentration. The absorbance of dye-sensitised films at peak wavelength is

used to estimate the films' dye loading. Dye-sensitised films were rinsed in acetonitrile for 15~20 min prior to measurements.

5.2.2 Mercury sensing

Selectivity. The selectivity measurement was carried out by addition of all metal ions including Hg^{2+}, Mg^{2+}, Cd^{2+}, Fe^{2+}, Co^{2+}, Ni^{2+}, Cu^{2+} and Zn^{2+} from their 2.0×10^{-2} M stock in acetonitrile. TiO_2 films, N621/TiO_2 films and HW456/TiO_2 films were immersed in ~60 μM non-aqueous solutions of different cations (namely Hg^{2+}, Mg^{2+}, Cd^{2+}, Fe^{2+}, Co^{2+}, Ni^{2+}, Cu^{2+} and Zn^{2+}) and the cyclic voltammograms were recorded.

Sensitivity. The CVs of N621/TiO_2 film was recorded at a scan rate of 10 mV/s in the electrolyte of 0.1 M TBAP in acetonitrile. To avoid the dye degradation, different amount of mercury ion were added from its 20 mM stock (in acetonitrile) for individual fresh N621/TiO_2 films.

5.2.3 Dye cation/Hole percolation

5.2.3.1 Chronoabsorptometry measurement

Chronoabsorptometry measurements recorded the corresponding optical spectra (wavelength 300~900 nm) as a function of the applied step potential (-0.4 V to 0.6 V and 0.8 V vs Fc/Fc^+ for N621 and HW456, respectively). The apparent diffusion coefficients of hole hopping through neighbouring adsorbed dye molecules by percolation were measured at different surface concentrations of dye molecules using chronoabsorptometry measurements employing the classical chronocoulometric methodologies - established on the semiinfinite diffusion model relating the charge Q exchanged against time with a modified electrode.[131] The derivation of the relationship between diffusion coefficient and chronoabsorbtometry can be seen in Appendix 1.

5.2.3.2 Estimation of Dye cation diffusion coefficient and diffusion length

The apparent dye cation(or hole) diffusion coefficient (D_{app}, cm^2/s) can be estimated either by fitting the experimental data quantitatively using **Equation 5-1** or by analysing the maximum anodic current from the CV data using **Equation 5-2**.[131]

$$j_p = (2.69\times10^5) z^{3/2} D_{app}^{1/2} C_0 v^{1/2} \quad \textbf{(Equation 5-2)}$$

Here j_p is the peak anodic current density in amperes/cm^2, z (= 1) is the number of electrons consumed in the electrode reaction (in this case, dye oxidation/reduction), C_0 is the dye concentration in the mesoporous TiO_2 films in mol/cm^3, and v is the scan rate in V/s.

Dye cation diffusion length can be calculated by **Equation 5-3**,

$$L = \sqrt{D_{app}\tau} \quad \textbf{(Equation 5-3)}$$

where L is the hole diffusion length, D_{app} is the apparent dye cation diffusion coefficient, which can be obtained from Equation 5-1 or 5-2, and τ is the dye cation lifetime, *i.e.* the oxidised dye regeneration time by the electrolyte. τ can be estimated by transient absorption spectroscopy (TAS)[142].

5.3 Results

As discussed above, lateral hole percolation across adjacent molecules adsorbed onto nanocrystalline, mesoporous metal oxide films has been studied using spectroelectrochemical techniques, in order to obtain the percolation threshold and the hole diffusion coefficient. It is shown that the kinetics of the hole percolation may be affected by molecular structure (its HOMO position) and molecular orientation on the metal oxide surface.

The optical transparency of nanocrystalline TiO_2 films, which shows negligible optical absorbance in the visible region (see **Figure 2-6**), makes it feasible for the

spectroscopic measurements of adsorbed dye molecules. The insulating properties of nanocrystalline TiO_2 film in the examined potential range, -0.4 V to + 0.8 V versus ferrocene/ferrocenium (see **Figure 2-8**), provide a background free platform for monitoring the oxidation reactions of adsorbed N621 and HW456 dye molecules. Therefore, the redox processes and the hole percolation kinetics of these dye molecules adsorbed on TiO_2 films can be investigated using dye-sensitised TiO_2 films as the working electrode under an applied potential step or a positive bias sweep.

5.3.1 DFT calculations of N621 and HW456 molecules

Density functional theory (DFT) calculations of the dye's neutral and cation HOMO orbitals were performed by employing B3LYP/LANDZ parameters using Gaussian. The calculations confirmed HOMO orbitals are localised upon the NCS groups for neutral (first oxidation state) HW456 molecules and spread over the phenyl amine moieties (TPA) for HW456 cations (second oxidation state). For N621, the HOMO (cation) orbitals are essentially ruthenium t_{2g} character with sizable contribution coming from the NCS ligand orbitals (**Scheme 5-1**). This implies that the first oxidation in both complexes is still dominated by ruthenium t_{2g} character.

5.3.2 Steady state absorption spectroscopy and dye loading

The steady state absorption spectra of N621/TiO_2 and HW456/TiO_2 films are shown in **Figure 5-1**. A control TiO_2 film spectrum is shown for comparison. As can be seen, the absorption bands at 530 nm for N621 and at 450 and 540 nm for HW456 correspond to a metal-to-ligand charge-transfer transitions (MLCT); the 530 nm and 540 nm bands for N621 and HW456 are the result of the presence of NCS ligands, as reported previously.[15]

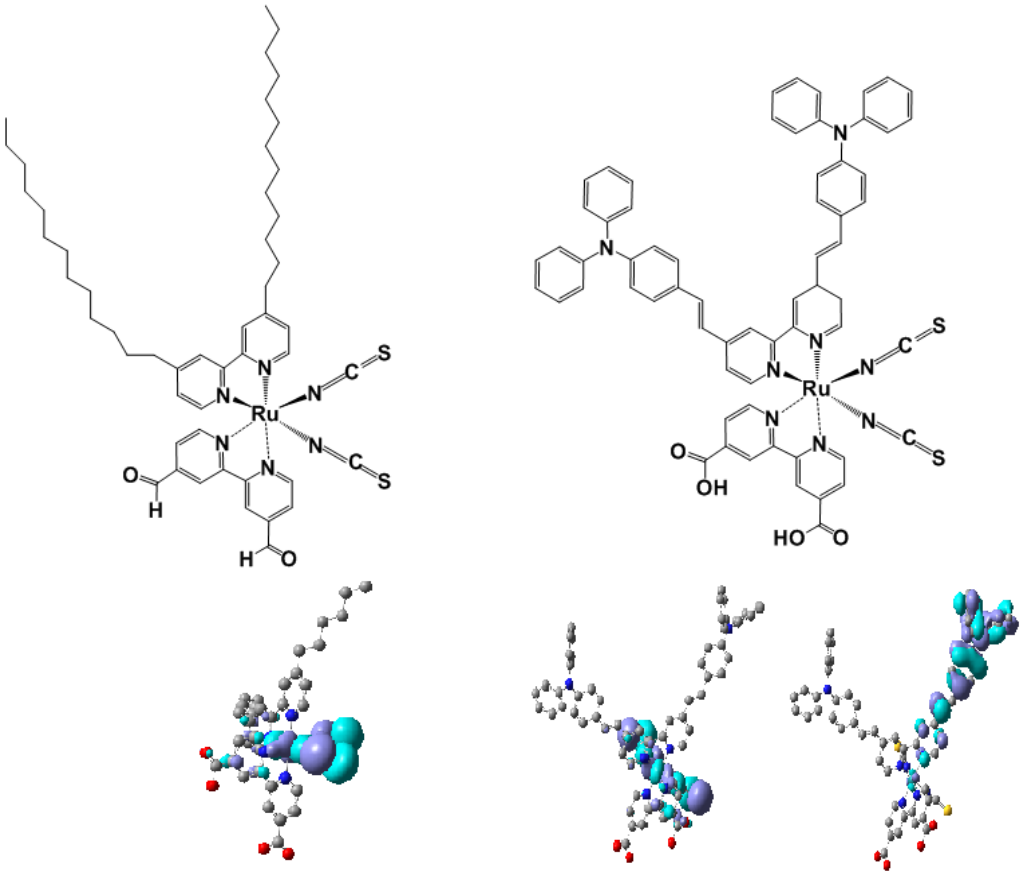

Scheme 5-1. Structures of [Ru(dcbpyH)(tdbpy)$(NCS)_2$] (N621, left) and (b) [Ru(dcbpyH)(tdbpy)$(NCS)_2(TPA)_2$] (HW456 (neutral (middle) and cation (right)) sensitiser and graphical representation of the dye cation HOMO orbitals as determined from DFT ab initio calculations.

The surface loading of dye molecules on mesoporous nanocrystalline TiO_2 films can be calculated by Equation 2-5 employing the molar extinction coefficient of 7,830 M^{-1} cm^{-1} at wavelength 530 nm for N621 and 24,600 M^{-1} cm^{-1} at 540 nm for HW456, respectively.[93,132] At a full monolayer dye coverage, the equilibrium dye loading experimental data are fitted by **Equation 1-14,** ${}^{s}\Gamma$ is 3.42 ± 0.02 and 1.64 ± 0.02 μmol/m^2 for N621 and HW456, and K_f =12.2 ± 3.4 and 8.1 ± 3.5 mM^{-1} for N621 and HW456, which corresponds to 2.0 × 10^{18} and 9.8 × 10^{17} molecules per m^2 TiO_2 surface for N621 and HW456, respectively. The estimated surface area one dye molecule occupies, S_{mol} (=1/(${}^{s}\Gamma \times N_a$), N_a is the Avogadro number, Equation 2-8) is estimated to be 50 and 100 $Å^2$ or 0.5 and 1 nm^2 for N621 and HW456 respectively, which is in reasonable agreement with the molecular dimension determined from the

modelling[143,144]. Consequently, the lower packing density of HW456 molecules adsorbed on nanocrystalline, mesoporous TiO_2 films implies a greater distance between adjacent HW456 molecules' core than in the case of N621.

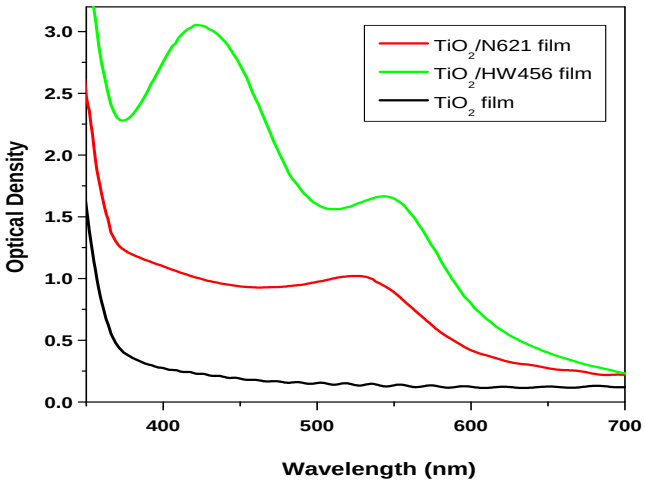

Figure 5-1. UV-Vis spectra of N621/TiO_2 film (**red**), HW456/TiO_2 film (**green**) and control TiO_2 film (**black**).

5.3.3 Potentiometric Spectroelectrochemistry

The changes of the UV/Vis absorption spectra for N621/TiO_2 and HW456/TiO_2 films before and after the application of positive oxidation potentials are shown in **Figure 5-2**.

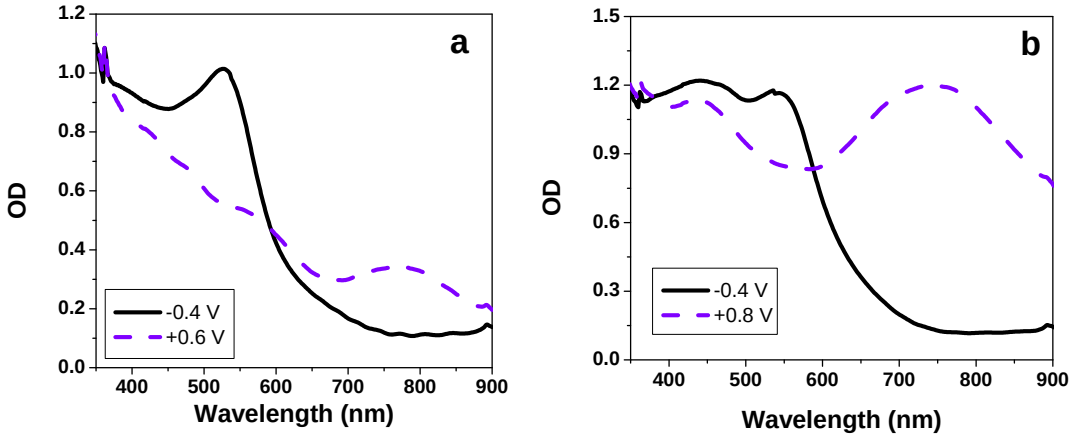

Figure 5-2. UV/Vis spectra of (a) N621 and (b) HW456 adsorbed on nanocrystalline, mesoporous TiO_2 electrodes measured ca. 4 minutes after the application of the potentials indicated. The potential range is from -0.4 to 0.6 V or 0.8 V vs Fc/Fc^+ for N621 and HW456, respectively. The electrolyte is 0.1 M TBAP in acetonitrile.

These changes in absorption spectra are assigned to dye oxidation. The applied potential is stepped from a potential where no current flows (e.g. -0.4 V *vs* Fc/Fc^+) to one at which dye cations are formed (+0.6 V *vs* Fc/Fc^+ for N621 or +0.8 V *vs* Fc/Fc^+ for HW456). The absorption spectra of the oxidised dyes were taken after ca. 4 minutes, allowing time for saturation of the dye oxidation processes (see below). The spectra are characterised by loss of the MLCT ground state absorption bands at 530 and 540 nm, and the appearance of cation absorption bands at 770 and 750 nm for N621 and HW456, respectively. The magnitude of these absorption changes are indicative of extensive (> 50 %) oxidation of the adsorbed dye molecules in both cases. The absorption in the near IR region (770 nm) is due to transitions from ligand orbitals to the d^5 ruthenium cation (LMCT). The slight blue shift of the near IR band in the HW456 (750 nm) as compared to that of N621 is assigned to de-stabilization of ruthenium orbitals caused by the donor strength of TPA groups. The enhanced optical density of the near IR band in HW456 indicates that in addition to the NCS ligands, the TPA groups are also involved in these LMCT transitions.[132] Similar results obtained with the N621/ZrO_2 films (**Figure A-3**) confirm that metal oxide films are insulating supporting materials in the potential range examined, and thus electrons in TiO_2 conduction band have no effect on the oxidation of dyes.

Following prolonged oxidation (more than 20 minutes), both sensitiser dyes showed absorption changes that were only quasi-reversible. This is consistent with the vulnerability to decomposition shown by similar ruthenium-NCS dyes reported previously[145] where oxidative degradation forms *cis*-$RuL_2(CN)_2$ (L = 2,2′-bipyridine-4,4′-bisphosphonic acid) indicated by an absorption peak at 450 nm.[146] Furthermore, the rate of dye degradation ($k_{degradation}$, estimated by normalising the differentiated ΔOD with respect to time, **Equation 5-4**, was compared with the rate of hole transport ($k_{transport}$, estimated by **Equation 5-5**):[147]

$$k_{degradation} = -(\frac{d\Delta OD}{dt})/\Delta OD \qquad \textbf{(Equation 5-4)}$$

$$k_{transport} = \frac{\pi^2 * D_{app}}{4d^2} \qquad \textbf{(Equation 5-5)}$$

It was found that $k_{transport}$ is of 0.40 s^{-1} which was much greater than the maximum $k_{degradation}$ (~ 9.8 x 10^{-3} s^{-1} for HW456 dye, **Figure A-4**). This implies that the degradation of dye cations is not fast enough to significantly influence the conclusions on percolation dynamics. To analyse percolation dynamics, transient electrochemical measurements were used on a time scale which avoids dye degradation, as detailed below.

5.3.4 Cyclic Voltammetry (CV) and Voltabsorptometry (CVA)

Cyclic Voltammetry (CV). During the scan from -0.4 to 0.8 V (vs Fc/Fc^+) at a scan rate of 1 V/s, as shown in **Figure 5-3**, the applied potential became sufficiently positive at +0.4V to cause oxidation of dye N621 molecule to dye cation (D^+) occurred on TiO_2 electrode surface. For the scan at a rate of 1 V/s, the oxidation of N621 dye molecules is accompanied by the anodic peak current i_{pa} = 3110 μA (at E_{pa} = 0.6 V). The reduction peak has a similar shape to the oxidation peak, and the cathodic peak current $i_{p,a}$ = -1561 μA at peak potential for the cathodic process with E_{pa} = 0 V. The Half-wave potential, $E_{1/2}$, is calculated from (E_{pc}+E_{pa}) / 2 = 0.3 V (vs Fc/Fc^+) and the peak current ratio, i_{pa}/i_{pc} = 2.

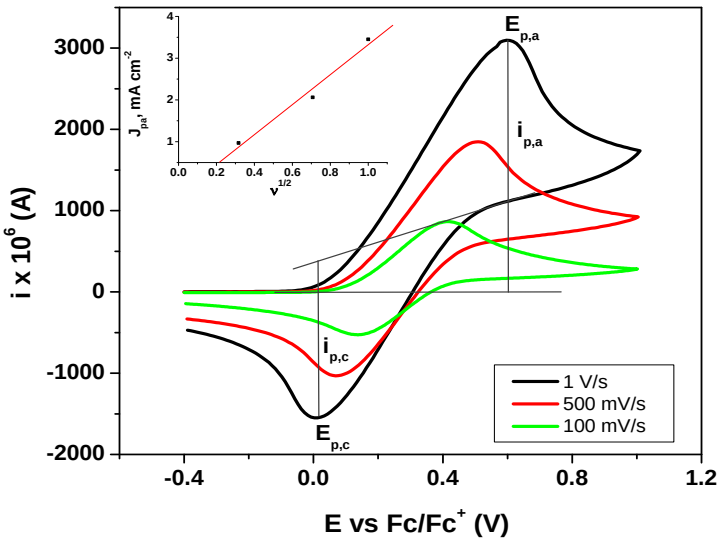

Figure 5-3. Cyclic voltammogram of the N621 complex adsorbed on TiO_2 film (~ 4 μm) measured at scan rates (v) of 1, 0.5, 0.1 V/s in acetonitrile with 0.1 M TBAP, respectively. The inset shows variation of anodic peak current, i_{pa}, with $v^{1/2}$.

It also can be seen in **Figure 5-3** that with a decrease of scan rate, the peak current of anodic and cathodic are all reduced. Meanwhile, the separation of peak potentials is reduced. This reduction in the reserve peak height observed shows a quasi-reversible voltammetric response. The inset shows a plot of oxidative peak current (i_{pa}) vs $v^{1/2}$, showing the $v^{1/2}$ dependence expected for a diffusional process. The fitting line does not pass through the origin which may be due to the charge effect of the film. ΔE_p (= E_{pa} - E_{pc}) is significantly scan rate dependent, varying from 280 mV at v =100 mV/s to 600 mV at v =1 V/s, characteristic of slow electron transfer[131].

CV, CVA and DCVA of dye-sensitised TiO_2 films. Voltammetric and in situ spectroelectrochemical measurements were conducted in a three-electrode cell (**Figure 2-9**). **Figure 5-4** shows the resulting current cyclic voltammograms (CV), and cyclic voltabsorptommograms (CVA) of both N621/TiO_2 films (left) and N621 dye free in solution (right) as a function of applied sweep potential. Control experiments were carried out by employing either FTO glass only, nanocrystalline mesoporous TiO_2 film on FTO glass but without the sensitisers, or dye-sensitised FTO glass as the working electrode, respectively. All the CVs of these control films show no oxidation and re-reduction process.

The CV signal monitors the current flow corresponding to the change in film redox state. In contrast, the CVA signal, monitoring the film optical density at the dye cation absorption maxima, tracks the total cation population. Comparison of the CVA and CV data is thus facilitated by differentiation of the CVA data, yielding the DCVA data shown in **Figure 5-4** (c). As the dye cation absorption peak (750 nm) is chosen to monitor the redox change of N621 in the optical measurement (CVA), DCVA is insensitive to both film charging and faradic currents. It is apparent that the DCVA data are similar to CV, confirming the CV data are due to the dye itself.

For the N621/TiO_2 films, quasi-reversible one-electron transfer processes are observable in both the CV and DCVA traces, with a mid-point potential $E_{1/2}$ at 0.25 V vs Fc/Fc^+, which is in agreement with dye free in solution (**Figure 5-4** (right)) and previous observation on dye-sensitised films.[93] In contrast, for the HW456/TiO_2 films,

the CVA and DCVA results are more complex, typically exhibiting two oxidation waves with mid-point potentials at 0 V and 0.5 V vs. Fc/Fc^+, as shown in **Figure 5-5**. A more detailed electrochemical study of HW456 is reported elsewhere.[132]

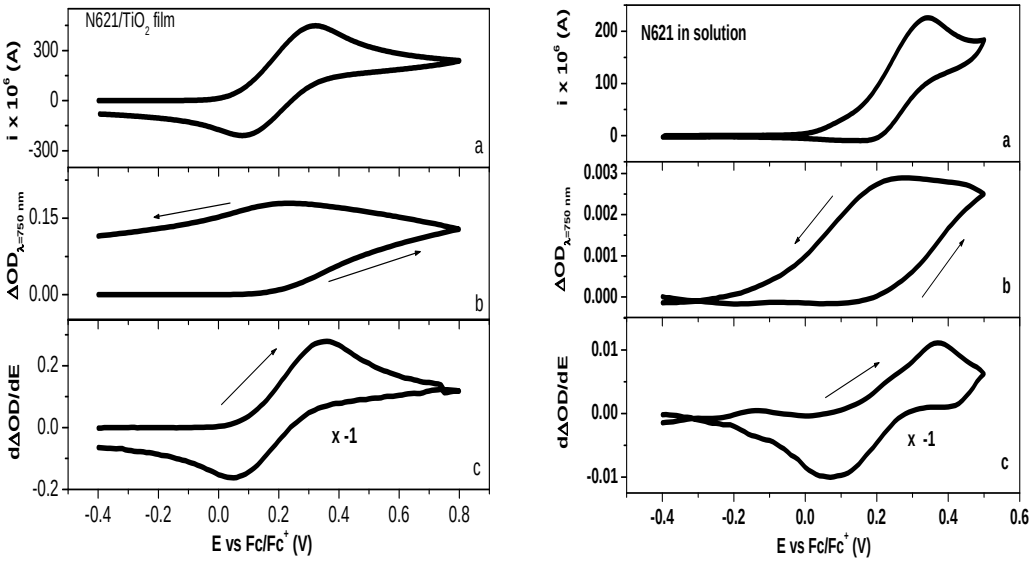

Figure 5-4. Spectroelectrochemical characterization (CV (a), CVA (b), and DCVA (c)) of N621 on nanocrystalline TiO_2 film (left) and in solution (right) at a scan rate of 100 mV/s. Arrows show the scan directions. In order to make it readily comparable to CV, the oxidation in DCVA data were multiplied by -1. All experiments were measured in non-aqueous solution (0.1 M TBAP in MeCN).

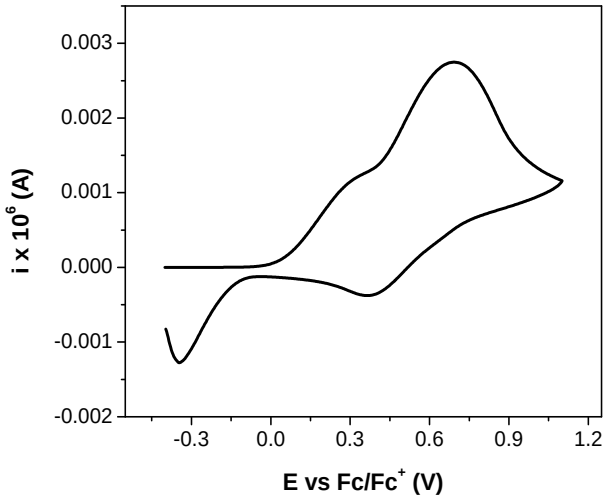

Figure 5-5. CV of HW456 on nanocrystalline TiO_2 film at scan rate 100mV/s in non-aqueous solution (0.1 M TBAP in MeCN).

The increase and then decrease of absorbance in the CVA of the N621/TiO_2 film (**Figure 5-4**b), correspond to the Ru(II)-NCS to Ru(III)-NCS oxidation and the Ru(III)-NCS to Ru(II)-NCS reduction, respectively. The trend of DCVA is in good correlation with the nearly reversible, well defined anodic and cathodic peak currents in the CV results (**Figure 5-4**a). For the purposes of this discussion, it is enough to note that +0.8 V is sufficient to oxidise both dye molecules. In addition, to determine the charge passed through the dye/TiO_2 films and thus the fraction of oxidized dye molecules, the current vs. time curves from the CV data (**Figure 5-4a** and **Figure 5-5**) are integrated. The calculation shows that one-third of N621 and almost all HW456 molecules have been oxidised within 12 and 15 second for TiO_2 films with full surface dye coverage, respectively. This indicates the faster hole transport in HW456/TiO_2 films relative to N621/TiO_2 films. Additionally, in the reverse scan direction, ~60% dye cation molecules are re-reduced. Consequently, the redox couple in both dye complexes are quasi-reversible.

5.3.5 Mercury response

Previously studies have demonstrated the strong interaction between the sulfur *p*-orbitals of -NCS groups in ruthenium complexes such as N719[88] and Z907[127] and mercuric ions, apparent for example as a colour change from red to yellow of N719/TiO_2 films in the presence of mercuric ions.[5,127] The quenching of anodic current of N621/TiO_2 electrode by addition of mercuric ions is observed, as shown in **Figure 5-6a**, in agreement with Nazeeruddin's results.[93] In contrast, for the HW456/TiO_2 electrode, the presence of mercuric ions increases its anodic current, as shown in **Figure 5-6b**. This implies different percolation behaviours of the two Ru-complexes and thus the selective sensing to mercury ion in organic solutions through electrochemical lateral charge percolation measurements. The selectivity and sensitivity of both ruthenium complexes were then studied in detail.

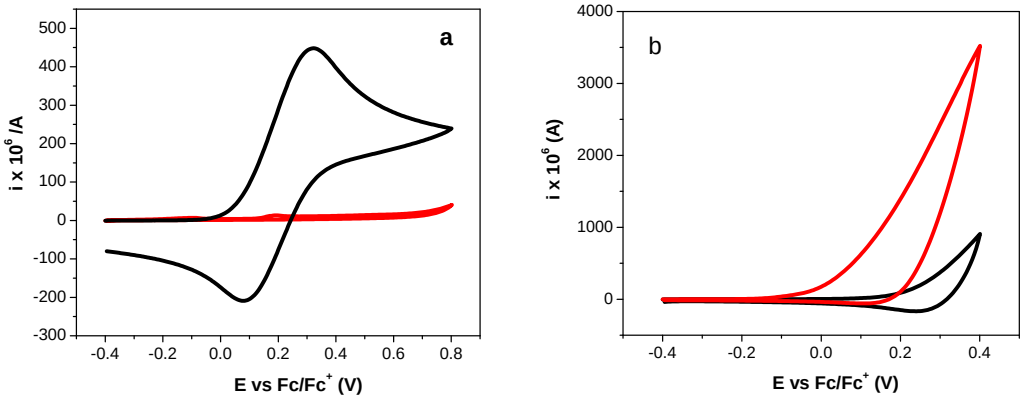

Figure 5-6. Cyclic voltammogram in the absence (**black**) and presence (**red**) of mercury ion (0.6 mM in acetonitrile) for N621/TiO_2 (left) and HW456/TiO_2 (right) films at scan rate 1 V/s in 0.1 M TBAP in acetonitrile.

Selectivity. The experimental results of N621/TiO_2 films in different cations solutions are shown in **Table 5-1**. Only mercury ion decreases the anodic peak current ~97% while other metals are fluctuated without N621 electro-bleaching. This demonstrates selective electrochemical mercury sensing with the N621/TiO_2 film, in agreement with its optical sensing selectivity[93]. However, copper (II) also shows ~44% decrease of anodic peak current which may influence the selectivity of mercury sensing when it exists at a high concentration (e.g. double or triple the mercury concentration). Also shown in **Table 5-1** are the results of HW456/TiO_2 films. Such films show non-selective mercury sensing.

Table 5-1 Selectivity of Mercury Sensing

Cation / R [a]	No M^+	**Hg^{2+}**	Mg^{2+}	Cu^{2+}	Cd^{2+}	Fe^{3+}	Co^{2+}	Ni^{2+}	Zn^{2+}
N621/TiO_2 film[b]	1.0	**0.01**	1.0	0.6	0.9	1.05	0.83	1.2	1.0
HW456/TiO_2 film[b]	1.0	**2.5**	1.1	0.9	4.0	5.0	1.0	1.2	2.0

[a] R= i_p/i_a, where i_a and i_p are the anodic current at 0.3V in the absence and presence of cations, respectively.
[b] Each individual 4μm thick dye-sensitised TiO_2 film was introduced 10 minutes into solutions containing the cations (0.6 mM in acetonitrile) above indicated.

Sensitivity. As N621/TiO_2 films are selective to mercury sensing, it is necessary to obtain the sensitivity and limit of detection (LOD). As can be seen in **Figure 5-7**, the linear response of anodic peak current i_{pa} to mercury concentration shows the sensing

sensitivity (namely $d(i_{pa})/d[Hg^{2+}]$) as 0.7 mM^{-1} and the detection limit (=0.01/sensitivity) as 3 ppm.

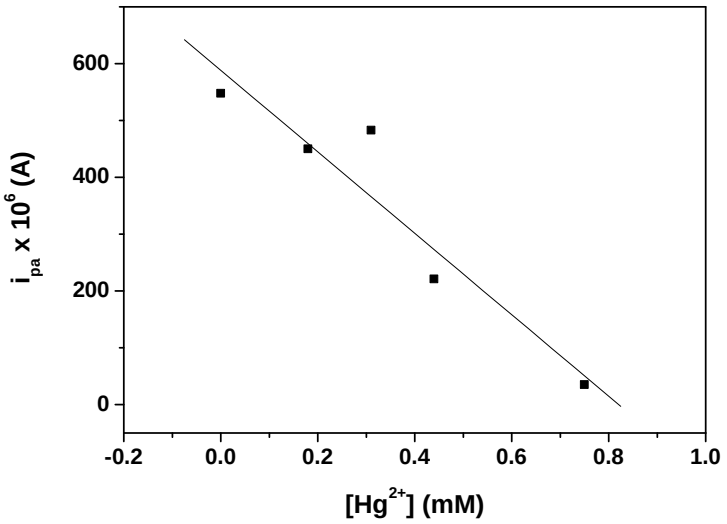

Figure 5-7. Relationship between the i_{pa} of N621/TiO_2 films and mercury concentration. Mercury was added from its 20 mM in ACN stock. All experiments were measured at 10 mV/s in non-aqueous solution (0.1 M TBAP in ACN).

5.3.6 Kinetics of hole percolation

The kinetics of dye cation formation were determined from chronoabsorptometry measurements, which monitor optical absorption changes at the dye cation absorption maxima (770 nm and 750 nm for N621 and HW456 respectively) induced by a step change in electrical potential applied to the dye-sensitised film. Typical data measured at full monolayer dye coverage is shown in **Figure 5-8a**. It is apparent that the kinetics of dye cation formation is significantly faster for HW456 compared to N621. For HW456, the optical response exhibits a half time of ~3 s, and saturates at ~20 s. In contrast, for N621, the signal did not saturate in the time scale plotted, and exhibited an estimated half-time of > 20 s.

Quantitatively, the experimental data were fitted using a modified version of the Cottrel equation[131] given by **Equation 5-1**. This relationship gives a good approximation to the exact solution for the diffusion of holes through a thin layer for times where $t < d^2/(4D_{app})$ (see Appendix A1 for details). Typical fits are shown in

Figure 5-8b, showing reasonable agreement with the experimental data, yielding value for D_{app} of 2.6×10^{-8} and 1.2×10^{-9} cm^2/s for HW456 and N621, respectively.

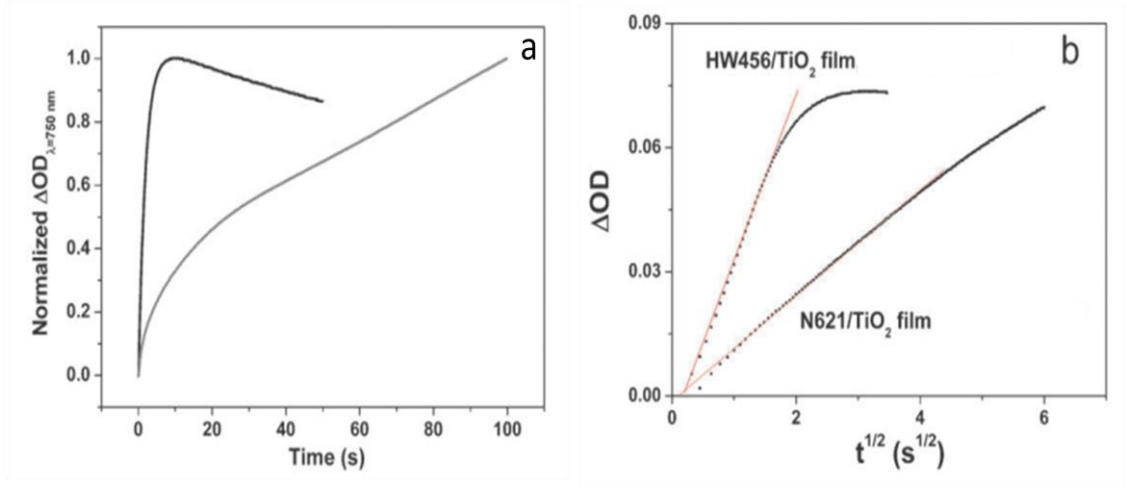

Figure 5-8. (a) Formation time of dye cations at a potential step of +0.3 V or +0.6 V vs Fc/Fc^+ for HW456 (**black**) and N621 (**grey**) and **(b)** ΔOD plotted as a function of $t^{1/2}$ and the fitting of the data using **Equation 5-1** (data in black scatter, fitting in red line).

Measurements similar to those shown in **Figure 5-4** and **5-8** were made for films with different dye loading. The hole diffusion coefficient was found to be dependent on the dye loading on the nanocrystalline TiO_2 films. The dependence of the anodic current and diffusion coefficient on dye surface coverage are shown in **Figure 5-9a** (N621) and **Figure 5-9b** (HW456). The apparent diffusion coefficient D_{app} was determined at different dye surface coverages ($=\Gamma/^s\Gamma$) from chronoabsorptometry data fitted by equation 5-1, where ΔOD_f was determined at sufficiently long time and the gradient was found from the linear region of the slope where $t < d^2/(4D_{app})$.

The hole diffusion coefficient D_{app} of both the $N621/TiO_2$ and $HW456/TiO_2$ films increases dramatically at $\Gamma/^s\Gamma$ >60%. For $N621/TiO_2$ films, the D_{app} values are also compared with an alternative estimate of D_{app} determined by analysing the maximum anodic current from the CV data using equation 5-2 (the data are plotted in **Figure 5-9a**).[131] It can be seen that at full dye loading, D_{app} from CV is 4.5×10^{-9} cm^2/s, somewhat larger than the value estimated from chronoabsorptometry data but within a similar magnitude. The difference may be related to the irreversible formation of an oxidation species (for example $[Ru(LL)_2(CN)_2]$)[146] which partially cancels the ΔOD signal from the cation.

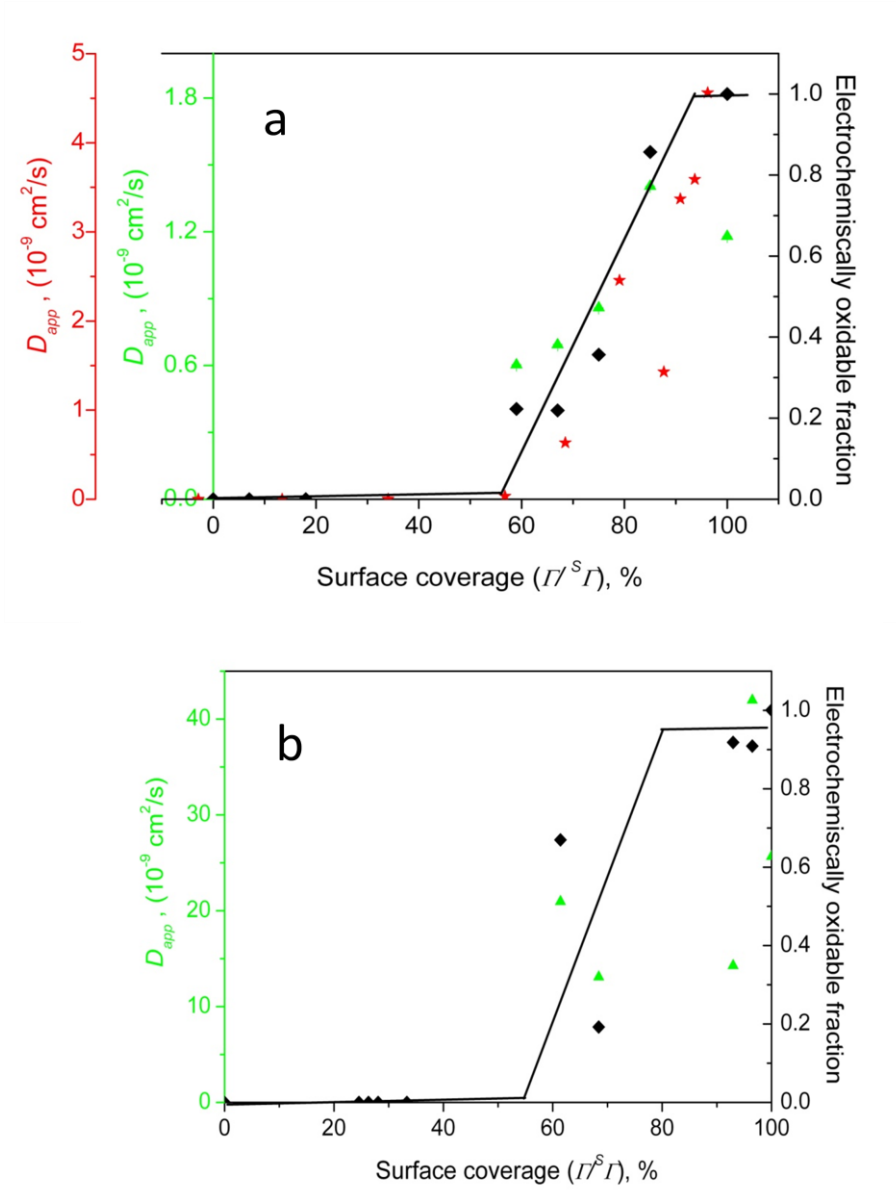

Figure 5-9. The D_{app} (**red stars**, fitted j_p vs $v^{1/2}$ by equation 5-2, far left Y axis), D_{app} (**green triangles**, fitted chronoabsorptiometry data by equation 5-1, left Y axis) and electrochemically oxidizable fraction (**black diamonds**, right Y axis) of **(a)** N621/TiO_2 and **(b)** HW456/TiO_2 films, following a potential step from -0.4 V to +0.6 V (vs Fc/Fc^+) for N621 and 0 V to 0.7 V (vs Fc/Fc^+) for HW456 as a function of the dye surface coverage. The electrolyte is 0.1 M TBAP in acetonitrile for both CV and chronoabsorptometry measurements. All experiments were measured at a scan rate of 100mV/s. The lines across the experimental dots (**black diamonds**) are plotted to mark the percolation threshold.

The similarity of the onset and variation of D_{app} determined by these different methods (chronoabsorptometry and CV) suggests that a rough approximation of the percolation controlled hole diffusion coefficient has been found, in line with the previous discussions.[17,127] The similarity of the percolation threshold demonstrates

that the current flow is due to the hole transport across the surface-coated TiO_2 nanoparticles. Below this threshold, there are not enough dye molecules to create a lateral percolation pathway on TiO_2 surface.

Also plotted in **Figure 5-9** is the electrochemical oxidisable fraction of dye $(=(\Delta OD_f/n_d)/(\Delta OD_f/n_d)_{max}$, where n_d is the number of dyes molecules in moles per unit TiO_2 films projected area (μmol/m^2)) as a function of surface coverage. This shows a similar percolation threshold ($\Gamma/^s\Gamma$ ~60%) for both dyes and indicates that a progressively larger proportion of the molecules on the surface can be oxidised as the surface coverage increases. This is expected as the fraction of molecules belonging to percolating clusters connected to the substrate increases.

5.4 Discussion

Percolation sensing mercury using functionalised metal oxide films (N621/TiO_2) has been demonstrated and works reasonably well. The change in anodic current of N621/TiO_2 electrode in the presence of mercury ions is linearly proportional to its concentration enabling the film to sense mercury voltammetrically. However, compared to other voltammetric mercury sensing strategies, this sensing method is not sensitive enough and needs to be improved for technology approach. Future work should therefore be focused on the improvement of the sensing sensitivity by, for example, developing micro-sized heterosupramolecular electrochemical devices using field-effect transistor (FET) configuration.

Then, the process of hole percolation through hole hopping between the adjacent molecules adsorbed on the nanocrystalline metal oxide films (such as TiO_2 and ZrO_2) is considered. This is only observed on a macroscopic (film) scale when the dye surface coverage is above the percolation threshold, where dye molecules have sufficient conductivity to create a conducting pathway for charge transport. During the oxidation of the dye molecules following an applied positive potential, holes are

injected into the film via the attached molecules from the FTO substrate and across the dye molecules anchored to the TiO_2 film surface.

The single bi-(carboxypyridine) (dcbpy) group of both dyes are responsible for anchoring the dye to the TiO_2 surface and result in significant flexibility in binding orientation.[148] This flexibility is likely to be important in enabling the sensitiser dyes to orientate on the TiO_2 surface such as to favour intermolecular electronic coupling, and thus hole transfer. This has been discussed previously for the Z907 sensitiser dye[148], analogous to N621 but with an short alkyl side chain, where molecular modelling calculations suggested monolayer dye binding would result in significant electronic coupling of the NCS groups between molecules. In contrast, for HW456 the lower dye density at monolayer coverage can be expected to reduce NCS group intermolecular interactions, with the primary interactions being between the larger TPA groups.

The hole percolation dynamics are 20-fold faster for donor-acceptor dye HW456 than its N621 analogue without the tri-phenyl amine (TPA) electron donating moieties, with an apparent hole diffusion coefficient of 2.6×10^{-8} cm^2/s compared to 1.2×10^{-9} cm^2/s at a full monolayer dye surface coverage. This difference in apparent diffusion coefficients is attributed to the presence of the TPA group in HW456 molecules as triphenylamines (TPAs) are well known to be good hole transport materials in, for example, solid-state DSSCs.[132,149] Such fast hole percolation of HW456 (short transport time ~5 s) has potential interest for a range of technological applications, such as the molecular wiring of otherwise insulating inorganic films for molecular nanotransistors applications, although it is noted that such applications will probably require the omission of NCS moieties to avoid instability limitations of the dye cation.

The binding of mercuric ions to both dyes is thought to be primarily due to the NCS groups, forming a NCS-Hg complex.[88,93,147] For N621, this prevents the NCS groups from participating in the intermolecular hole exchange along adjacent dye molecules. This suppresses the hole percolation within the molecule network, which is in agreement with the previous studies of Z907 dye molecules.[127] In contrast, for

HW456, the observed increase in hole percolation in the presence of mercuric ions is consistent with hole percolation for this dye being primarily mediated by the TPA groups. It thus can be assumed that the hole percolation pathway is along the overlapped neighbouring NCS groups for the N621 functionalised films, whereas for the HW456 functionalised films hole percolation is via the overlapped intermolecular TPA ligands (**scheme 5-3**).

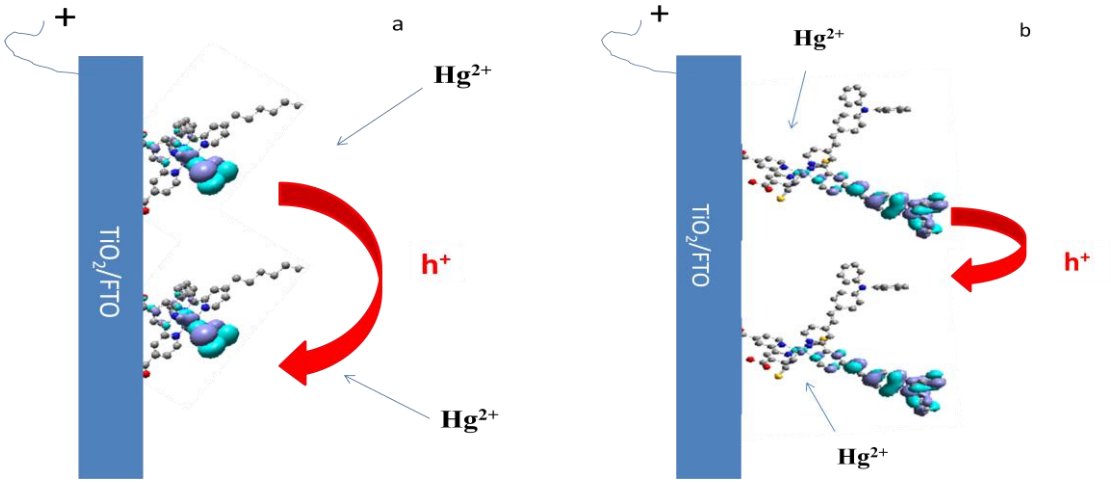

Scheme 5-3. Schematic model showing the lateral hole transfer percolation along dye-sensitised TiO_2 films: (a) N621/TiO_2 film, (b) HW456/TiO_2 film.

The relevance of these results to dye-sensitised solar cell is further investigated. In DSSCs, the dye cation can undergo two reactions: one is regeneration, in which D^+ is reduced by iodide in the electrolyte (equation 1-3) and the other is the recombination of the D^+ with electrons in the TiO_2 conduction band (equation 1-4). Dye cation (or hole) percolation across the surface of the TiO_2 film, has not previously been considered as a significant issue for device function. However, this hole percolation may change dye cation regeneration and recombination dynamics. It could in principle favour device function by, for example, enabling dye cations generated in small pores of the TiO_2 mesoporous network where iodide may have limited access to move to nearby dyes, or in solid-state OMeTAD cells where dye cations move towards spiro-OMeTAD (hole-transport material, HTM). On the other hand, hole percolation could potentially decrease device efficiency either by facilitating recombination with trapped TiO_2 electrons or by resulting in cation trapping on surface impurities. Therefore, to understand the influence of hole percolation on

DSSC's device performance, dye regeneration and hole percolation dynamics are further considered.

The dye cation/hole percolation (or 'diffusion') length in cell can be obtained from the chronoabsorptometry measurements reported herein, coupled with dye cation lifetime kinetics determined by transient absorption spectroscopy (TAS). It can be estimated by equation 5-3 and the results are shown in Table 5-2. Although dye HW456 shows slower regeneration dynamics compared to N621 dye[142,148], the hole diffusion coefficient is ~20 times bigger. As a result, the hole diffusion lengths are 1 and 8 nm for N621 and HW456 molecules in DSSCs. This implies that the hole diffusion length of HW456 is about half of the TiO_2 particle size (~15 nm), and thus HW456 cations located in a pore which is not well connected to the electrolyte are more likely to reach the redox couple or HTM and be regenerated than N621 cations. In addition, the number of dye molecules within a 'diffusion area', e.g. the dye cation or hole percolation area, πL^2, is estimated to be 6 and 200 nm^2 for dye N621 and HW456 respectively. This diffusion area represents the surface which the dye cation/hole can percolate across the surface-coated TiO_2 nanoparticles before regeneration by iodide or the HTM. In this regard, it is noted that an analogous dye to HW456 has been shown to yield superior performance to N621 in solid state DSSCs employing spiro-OMeTAD.[132,132,149] On the other hand, a higher diffusion area may also facilitate recombination with electrons or hole trapping/recombination at surface impurities. As such, further studies could investigate the effect of hole percolation in DSSCs by measuring the dye regeneration and recombination processes at different dye surface coverage.

Table 5-2 Comparison of hole percolation to dye cation regeneration

Film	**N621/TiO_2**	**HW456/TiO_2**
D_{app} (cm^2/s)	1.2×10^{-9}	2.6×10^{-8}
Surface area per dye S_{mol}(nm^2/dye)	0.5	1
Dye cation regeneration time τ (μs)*	10	25
Hole diffusion length L (nm)	1	8
Numbers of dye molecules in the area πL^2 (nm^2)	6	200

*Regeneration time for dye cation by TAS was determined elsewhere.[142,148]

5.5 Summary

The electrochemical sensors developed in my studies are based on the interaction between dyes and the mercury ions. It is successful because the dye cation percolation is changed by the binding of mercury to the dye molecules. However, mercury sensing with dyes N621 and HW456 molecules are limited by their degradation.

Cation/hole percolation dynamics can be obtained by combining electrochemical and spectroelectrochemistry techniques. A fast cation percolation of the donor-acceptor dye HW456 adsorbed on the nanocrystalline TiO_2 film was observed. The high value of the apparent hole diffusion coefficient of such film may enable its applications in fabrication of percolation batteries, molecular nanotransistors and sensors. Additionally, cation transportation in DSSC involving percolation, regeneration and recombination can be investigated for optimization of cell performance.

Chapter 6 Iodine-metal oxide film interaction

In the last three chapters, functionalized metal oxide films have been investigated for applications of heterogeneous sensing and scavenging toxic ions, such as mercury and cyanide. Moreover, in chapters 5, the diffusion coefficients of dye cations (or holes), measured by electrochemical and spectroelectrochemistry techniques, were used to estimate the diffusion length of dye cation before being regenerated/reduced by the reduced form in the redox couple, for example, iodide in iodine-iodide based DSSC.

The purpose of this and the following chapters is to address the iodine-metal oxide film interaction and iodine-functionalised mesoporous metal oxide films interaction, and to consider the importance of these interactions for the function of dye-sensitised solar cells.

6.1 Introduction

The optimised electrolyte used in dye sensitized solar cells (DSSCs) is a mixture of a redox couple (e.g. iodine/iodide) and other salts (e.g. 4-tert-butylpyridine (tBP) and lithium iodide (LiI)) in either organic solvents such as acetonitrile[33] or water[34]. With these additives, the conduction band edge of TiO_2 is shown to shift negatively (with tBP) or positively (with Li^+), resulting in an increase or decrease in cell open circuit voltage (*V*oc).[33] For the iodine/iodide redox couple, there is a recombination between electrons (injected into the TiO_2 conduction band from the excited state dye) and iodine (or triiodide), as shown in Equation 1-7, which in turn reduces the cell's *Voc*. Additionally, the diffusion, reaction and mass transport of iodine and iodide in both the electrolyte and TiO_2 nanopores (different from the bulk TiO_2 films) in DSSCs all influence cell performance, especially in the water-based electrolyte[34]. All these imply the interaction between TiO_2, dye molecules and ions/salts in the electrolyte. In this chapter, the TiO_2 surface interaction with the iodine redox couple is addressed.

Iodine has been shown to exhibit different colours in different solvents, for example, it is pink in dichloromethane and dark red-orange in acetonitrile. These colour differences are suggested to be due to the formation of iodine charge transfer complexes.[150] An assumed reaction mechanism between iodine (electron acceptor) and solvent (electron donor) is that it forms an outer complex and then transforms to an inner complex which further forms triiodide[151], as shown in **Equation 6-1** and **6-2**.

$$D + I_2 \rightleftharpoons DI_2 \longrightarrow DI^+I^- \qquad \textbf{(Equation 6-1)}$$

Donor Acceptor Outer complex Inner complex

$$DI^+I^- + I_2 \longrightarrow DI^+ + I_3^- \qquad \textbf{(Equation 6-2)}$$

Inner complex

Typical studies in solution show that the equilibrium reaction between iodine and acetonitrile forms the triiodide band either in its own or in a medium such as carbon tetrachloride (CCl_4) or cyclohexane solution.[150] The newly observed band of triiodide can be seen either in UV-Vis absorption spectrum (291 nm and 360 nm in acetonitrile)[152], infrared absorption spectrum (183 cm^{-1} in *n*-heptane)[153] or Raman spectrum (112 cm^{-1} and 207 cm^{-1} in acetonitrile)[154].

All these iodine interactions with solvents were investigated in solution. However, few studies have reported on the iodine interaction with TiO_2 electrodes, which is critical to the diffusion of iodine, iodide and triiodide through the nanopores of nanocrystalline mesoporous TiO_2 films. Kebede et al[152,155] examined iodine-solvent interactions and the diffusional permeability of triiodide ions in acetonitrile in free standing TiO_2 membranes with a porosity of 55% and determined the apparent diffusion coefficient to be 3.4×10^{-6} cm^2 s^{-1} which is probably sufficiently large for current designs of organic solvent based DSSCs. However, these results cannot explain the observation of photocurrent in iodide-free cells[156] and the possible mechanism of iodine interaction with TiO_2 nanoparticles. In this chapter, absorption spectroscopy has been employed to investigate the interaction between iodine and metal oxide films in acetonitrile. The possible reactions and ions existing in the system, shown in **Scheme 6-1**, are discussed. This study provides further evidence to

understand the iodine reduction reaction in DSSCs, and thus to reduce dark current and improve cell performance.

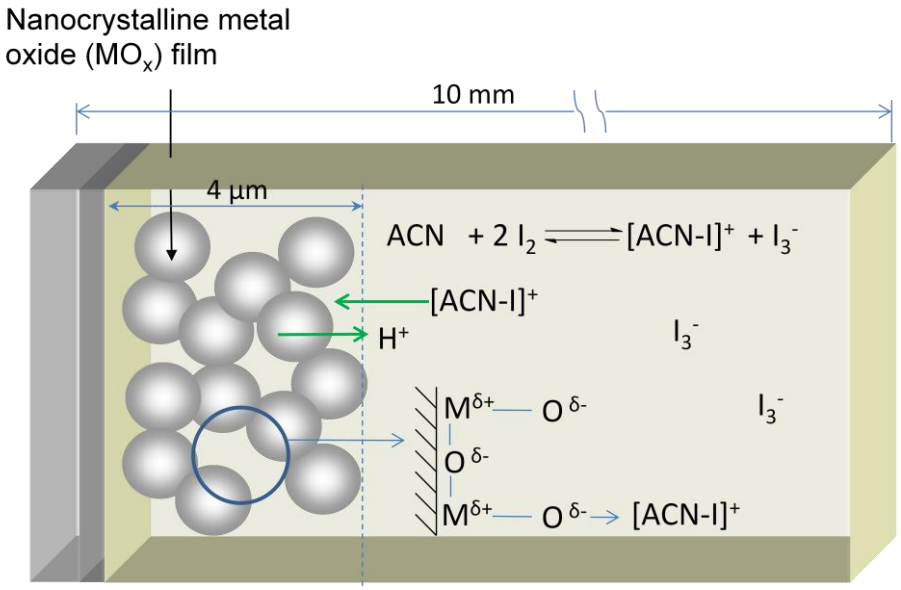

Scheme 6-1. Scheme of iodine-metal oxide interaction in iodine in ACN solution in 10 mm cuvette.

6.2 Experimental section

Film sensitisation. Nanocrystalline, mesoporous metal oxide films employed in the studies are TiO_2 (particle sizes are either 15 or 400 nm), ZrO_2 (30 nm) and Al_2O_3 (50 nm)[108]. These films were prepared according to the processes shown in 2.1.2~2.1.4 on microscope slides (VWR) by doctor blading. The 400 nm TiO_2 films were fabricated using Ti300 paste (Solaronix, Switzerland, SEM image shown in **Figure A-5**). All films were cut into a size of 0.9 x 1 cm^2. N719/TiO_2 films were obtained by soaking the ca. 4 µm-thick TiO_2 film into 0.3 mM dye solution in a 1:1 mixture of acetonitrile/*tert*-butanol at room temperature overnight. The N719/TiO_2 films were rinsed in acetonitrile for 20 minutes prior to dipping into the I_2 in ACN solution.

Time dependence of films in iodine solution. Nanocrystalline metal oxide films were immersed into 2 ml 2 x 10^{-4} M I_2 in acetonitrile (ACN) solution in a 10 mm cuvette (Stantus) over a period of one hour. The time dependence of the absorption spectra of the solution in the presence and absence of metal oxide films were

monitored at room temperature using UV-Vis Spectrophotometer. Measurement of the solution which had been exposed to the metal oxide nanoparticles was achieved by positioning the metal oxide films next to the inner wall of the cuvette but out of the spectrophotometer light beam. The reversible studies were performed by immersing the 'iodine-bound-TiO_2' films into a mixture of iodine (5 mM) and iodide (10 mM) in ACN solution for one hour and then these films were immersed into a fresh I_2 in ACN solution and the absorption spectra were measured repeatedly at different time periods.

All UV-Vis measurements are carried out using air as the baseline. Control experiments were performed with the same size of microscope slide only.

6.3 Results

6.3.1 Iodine in acetonitrile and dichloromethane

The absorption spectra of iodine in acetonitrile (ACN) and dichloromethane (DCM) are presented in **Figure 6-1**. By comparing the absorption spectra of I_2 in ACN (black solid) to I_2 in DCM (black, dash), the 362 nm peak can be confirmed as the triiodide band. This is also confirmed by comparison with the absorption spectra of iodine and iodide mixtures (which are well known to produce triiodide) in both solvents (in blue) as only the 362 nm peak is increased (**Figure 6-1**) compared to the absorption spectra without iodide (in black). These results are in agreement with previous studies[150,152]. In addition, this triiodide band is also observed for I_2 added to 3-methoxypropionitrile (MPN) solution, but not in I_2 in CCl_4 solution. This may be due to the difference in the donor number (DN) of these solvents.[152]

Iodine may react with ACN to produce $[ACN\text{-}I]^+$ and triiodide (**Equation 6-3**).

$$ACN + 2\,I_2 \rightleftharpoons [ACN\text{-}I]^+ + I_3^- \qquad \textbf{(Equation 6-3)}$$

The extinction coefficient (ε) of triiodide in acetonitrile solvent can be estimated by Beer-Lambert law $A = \varepsilon \times n \times 10^3$ (Equation 2-5) to be 3.3 x10^4 and 5.6 x10^4

M^{-1} cm^{-1} in DCM and ACN respectively, within the same order of magnitude reported previously by Popov (2.6 x10^4 M^{-1} cm^{-1} in ACN)[157].

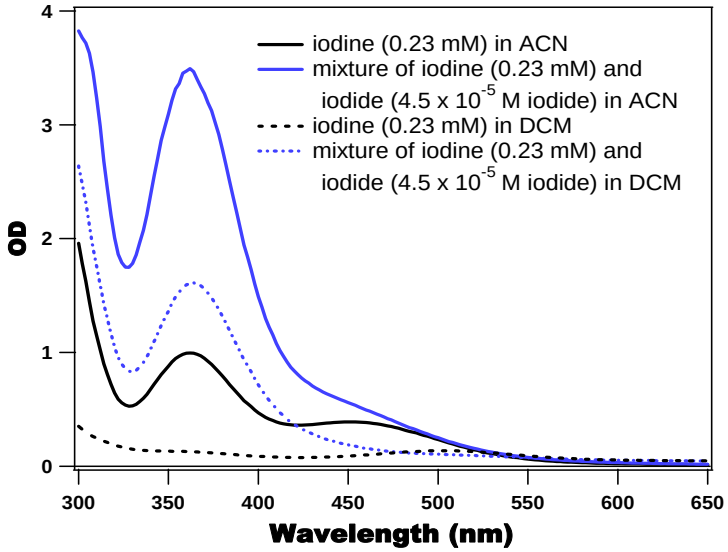

Figure 6-1. Absorption spectra of iodine and iodine mixed with iodide in dichloromethane (**blue**) and acetonitrile (**black**) solutions, respectively.

6.3.2 Interaction of iodine with metal oxide films

Figure 6-2 shows the solution absorption spectra measured when the nanocrystalline, mesoporous TiO_2 films (particle size 15 nm, film thickness ~3.6 µm) are immersed in I_2 in ACN solution. The optical density of triiodide band (362 nm) increases significantly, whereas that of the iodine band (460 nm) decreases slightly, as the exposure time to the nanocrystalline mesoporous TiO_2 film is increased. After exposure to the TiO_2 film for one hour, the solution contains 2.5 x 10^{16} triiodide ions compared to 6.9 x 10^{13} of TiO_2 particles in the film (calculated by assuming spherical particles with 15 nm diameter), i.e. the number of triiodide generated per TiO_2 particle is estimated to be 360 under the equilibration. For the control experiments, the same size microscope slide without TiO_2 was employed. The immersion of the slide in the iodine in ACN solution (black dash in **Figure 6-2**) did not show significant change in the absorption spectrum, indicating that the triiodide generated in solution is specifically derived from interactions with the TiO_2 nanoparticles.

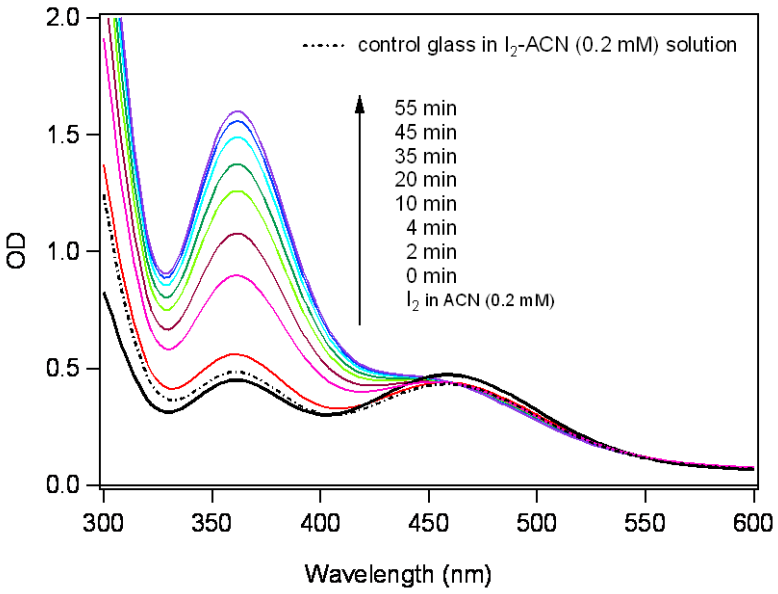

Figure 6-2. Time dependence of UV-Vis spectra of I_2 in ACN solutions in the absence (black) and presence of nanocrystalline mesoporous TiO_2 films. Also presented in the above graph is the UV-Vis spectrum of control microscope slide (black dash) in 0.2 mM iodine in acetonitrile for 55 min.

To investigate the reusability of this iodine-bound-TiO_2 film, it was then immersed in a mixture of iodine and iodide solution. It is found that this film can be reused, showing the same characteristics as a fresh TiO_2 film after reversed by the mixture (**Figure A-6**). This increase of the triiodide band for I_2 in ACN solution in the presence of nanocrystalline TiO_2 film might be expected from (1) the reaction between the electrons in TiO_2 conduction band and iodine or the surface impurities; (2) more generation of either $[ACN\text{-}I]^+$ or $[TiO_2\text{-}I]^+$ ions, probably with the release of protons (from nanopores) to the bulk solution for charge balance.

To examine the first hypothesis, further experiments were carried out in I_2 in ACN solutions with either insulating nanocrystalline, mesoporous ZrO_2 or Al_2O_3 films, and in ferrocium hexafluorophosphate ($FcPF_6$) in ACN solution with TiO_2 films. Similar trends with ZrO_2 and Al_2O_3 films as that of TiO_2 films were found, as shown in **Figure A-7**. Meanwhile, for the TiO_2 film immersed in $FcPF_6$ in ACN solution, there is no reduction of Fe(III) to Fe(II) observed after one hour (**Figure A-8**). Consequently, the increased triiodide band in the presence of nanocrystalline TiO_2 film for iodine in acetonitrile is not related to the electron density in its conduction

band. Furthermore, the triiodide species was produced with iodine in ACN solution with both base-washed TiO_2 films (to clean the surface impurities) and TiO_2 films prepared from different processes with and without organic binders (such as polyethylene glycol). The effect of these metal oxide films on iodine in ACN solution is not catalytic because these films can make triiodide only once without first reversing the effect (e.g. there is no effect when the same film dipped in a fresh I_2 ACN solution). All these observations may imply that TiO_2 nanopores stabilize the $[ACN\text{-}I]^+$ or $[TiO_2\text{-}I]^+$ ions.

On the other hand, the triiodide formation with the presence of nanocrystalline TiO_2 films is not shown in DCM. As can be seen in **Figure A-9**, no triiodide band (362 nm) appeared when a nanocrystalline, mesoporous TiO_2 film is immersed in the I_2 in DCM solution for 35 min, which implies that the reason TiO_2 film cannot produce triiodide in DCM may be due to an absence of triiodide ion generation in the I_2 in DCM solution. This implies the function of TiO_2 films in the I_2 in ACN solution is only to stabilize the formed $[ACN\text{-}I]^+$, but not to form $[TiO_2\text{-}I]^+$ specimen.

6.3.3 TiO_2 Particle size effect

As the particle size affects the film's surface area (SA) and porosity, 400 nm particle size TiO_2 films were examined in the same way as small particles (15 nm) to assess the influence of these factors. The results are shown in **Figure 6-3** and **Figure A-10**. **Figure 6-3a** shows that three times more triiodide ions is generated by the TiO_2 films with small particles (15 nm, black) than large particles (400 nm, blue). For small particles, the triiodide concentration in solution is determined to be 1.9×10^{-5} M, indicating ~10% of the iodine is dissociated to form the triiodide ions in one hour.

To assay the reduced generation of the triiodide by large particles, the change of optical density (ΔOD) was normalised by surface area (SA) and pore volume (Vv), *i.e.* ΔOD/SA and ΔOD/Vv, which were plotted *vs* time at triiodide peak (362 nm), as shown in **Figure 6-3b** and **c.** The surface areas of the 1 cm^2, 3.6 µm thick-TiO_2 film are estimated to be 4.7×10^{-2} and 2.8×10^{-3} m^2 for 15 nm and 400 nm TiO_2 particles,

respectively. The pore volume (Vv) is calculated by the subtraction of the particles' volume from the total film volume, which is estimated to be 2.4 x 10^{-4} and 2.2 x 10^{-4} cm^3 for 15 nm and 400 nm TiO_2 particles, respectively. As the pore volumes of two types TiO_2 films are almost the same value, the trends of ΔOD and ΔOD/Vv are similar. In contrast, the ΔOD/SA *vs* time plot is opposite to that of the OD *vs* time. This is due to the large surface area of the TiO_2 film with 15 nm particles (16 times bigger than that of 400 nm particles). Although the triiodide generation effect is reduced by larger particles (3 times), this reduction is not as great as the reduction in particle surface area (16 times).

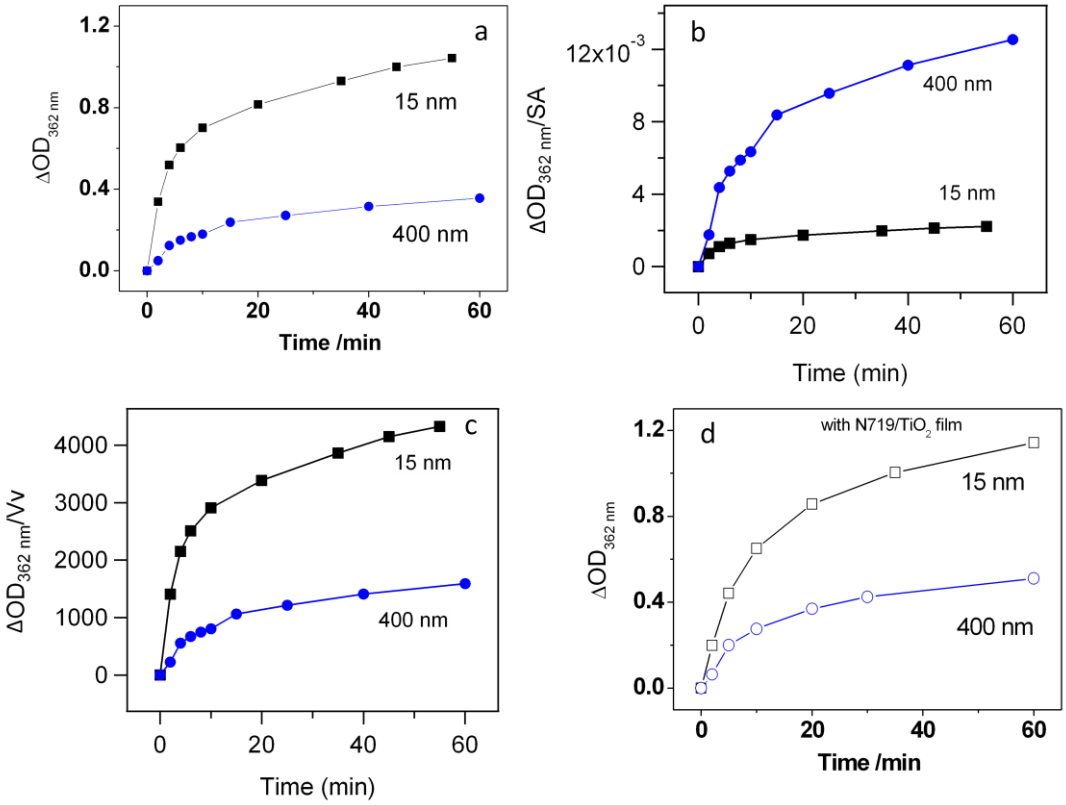

Figure 6-3. Time dependence of ΔOD of TiO_2 films (a); ΔOD normalized by surface area (b) and by pore volume (c), and ΔOD of N719/TiO_2 films (hollow) in different TiO_2 particle sizes: 15 nm (square, **black**) and 400nm (circle, **blue**).

Also shown in **Figure 6-3d** and **Figure A-11** is the results of N719/TiO_2 films (400 nm and 15 nm) in I_2 acetonitrile solution. Comparison of **Figure 6-3a** to **d**, the triiodide band generated with and without dye on the films' surface is approximately the same amount. The surface area of TiO_2 film reduced by dye coverage has no effect on the triiodide generation, which might be due to the compensation of triiodide

generated from iodine-dye binding which produces iodide and then triiodide in solution (see next chapter for details).

6.3.4 Effect of initial I_2 concentration

All the above results show that the production of triiodide in I_2 acetonitrile solutions in the presence of nanocrystalline TiO_2 films is slow, occurring on a time scale of minutes. This was also true in previous solution studies[151,158]. To examine the relationship between the amount of triiodide generated and the initial iodine concentration, three iodine solutions were measured in the presence of 15 nm TiO_2 films. The results are shown in **Figure 6-4**.

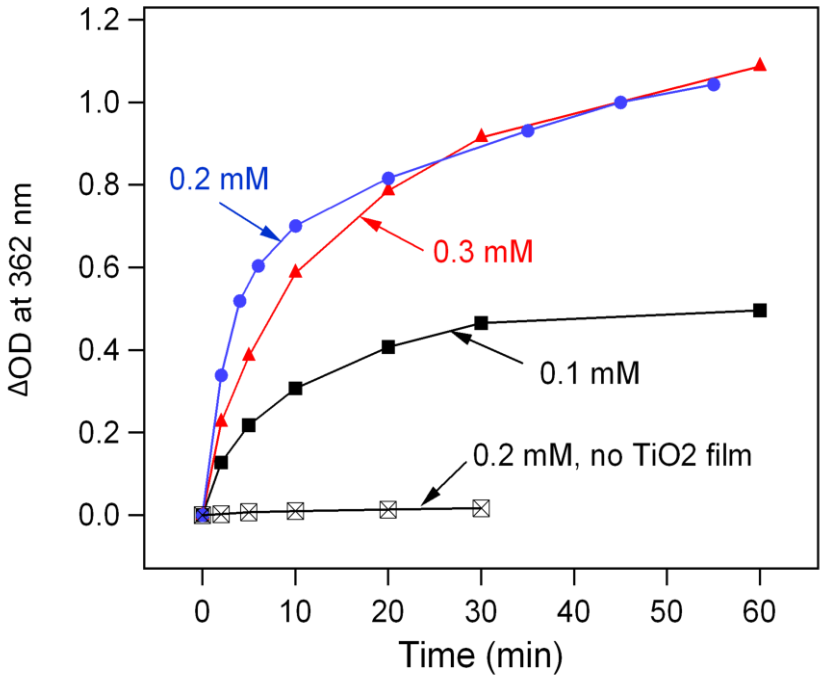

Figure 6-4. Change of optical density at different initial iodine concentration for 15 nm TiO_2 films. Control experiment was undertaken without TiO_2 film.

As can be seen in **Figure 6-4**, the TiO_2 films have increased the forward reaction in the equilibrium reaction (**Equation 6-3**). When the iodine concentration is above 0.2 mM, there is no significant difference in the production of triiodide from TiO_2 film after 30 min. The TiO_2 films in three solutions at different initial iodine concentration are saturated after one hour, exhibiting a half time of 4 min for 0.2 mM I_2, and ~8 min

for 0.1 and 0.3 mM I_2 in ACN solution. From **Figure 6-4**, the amount of triiodide formed in 0.2 mM and 0.3 mM I_2 acetonitrile solution are approximately 2 times bigger than that in 0.1 mM I_2 acetonitrile solution.

6.3.5 Cation (Li^+) effect

The absorption spectra of the mixtures of iodine with different addition of lithium perchorate ($LiClO_4$) in ACN solution were also measured. The results are shown in **Figure 6-5**. An increase of triiodide band at 362 nm and a decrease of iodine band at 460 nm are observed as the addition of Li^+ increased. Apparently, the lithium cation assists the triiodide production in I_2 acetonitrile solutions. The extra amount of triiodide generated by $LiClO_4$ may be due to the stabilization of $[ACN\text{-}I]^+$ ion by ClO_4^- ions. Further studies could investigate the effect of ClO_4^- ions by other lithium salts, such as LiCl.

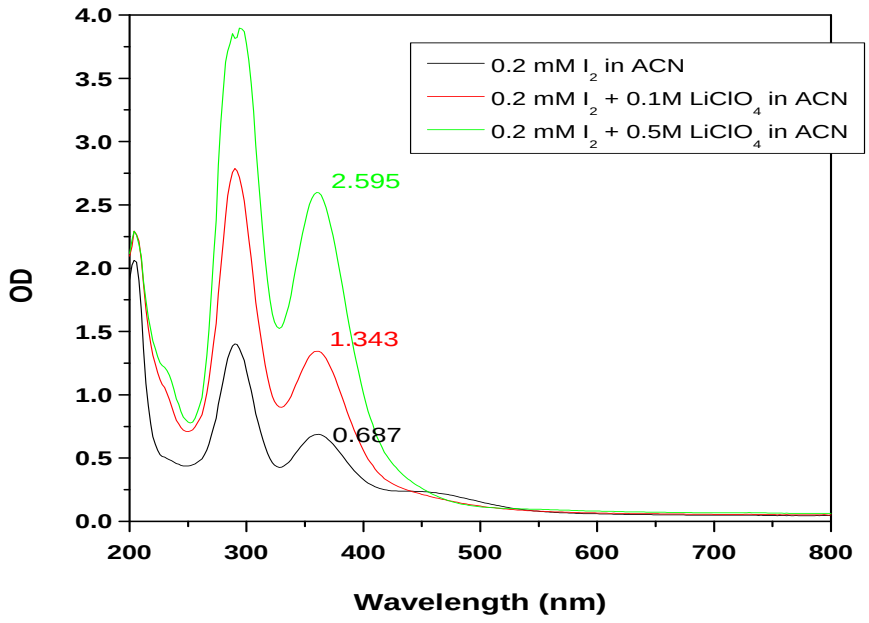

Figure 6-5. UV-Vis spectra of iodine in acetonitrile (0.2 mM, **black**) and iodine mixed with lithium perchlorate (0.2 mM iodine and 0.1 M (**red**) and 0.5 M (**green**) in ACN solution.

Further experiments were carried out in the presence of nanocrystalline TiO_2 film. The changes in the optical density of the triiodide band at 362 nm with time in the

presence of a nanocrystalline TiO_2 film with and without lithium cation present in solution are shown in **Figure 6-6**.

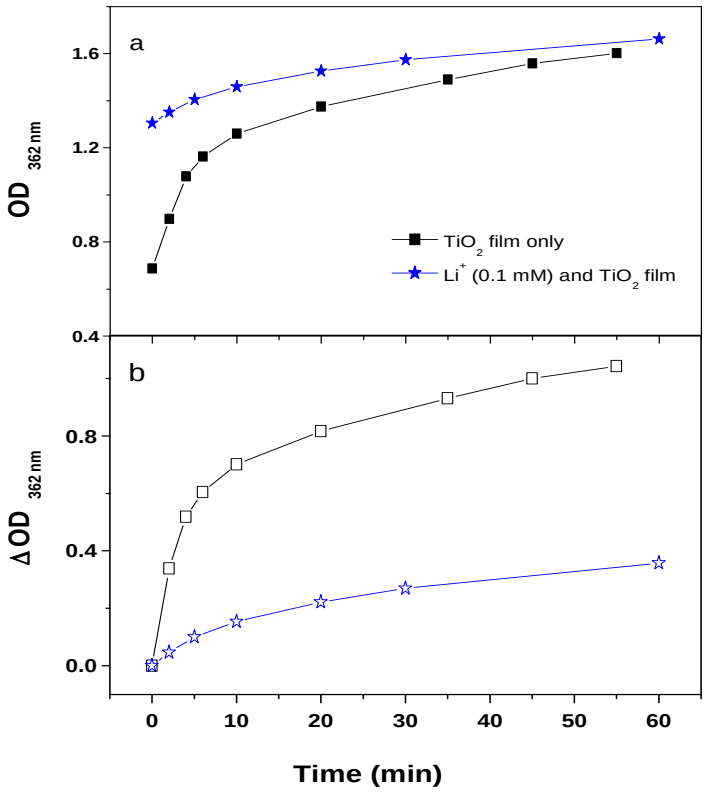

Figure 6-6. (a) Optical density (OD) and (b) the change of optical density (ΔOD, subtracting the triiodide produced in the absence of TiO_2 film, hollow) at triiodide peak (362 nm) to time in the presence of the TiO_2 film only (square), and Li^+ (0.1 mM) and TiO_2 film (star) in 0.2 mM I_2 acetonitrile solutions, respectively.

Apparently, the triiodide band reaches the same level both with and without Li^+ after 60 min in the presence of the TiO_2 film (compare the two curves in **Figure 6-6**a), while the initial triiodide in solution in the absence of the TiO_2 film (at time t = 0) shows a big difference. To obtain the extra amount of triiodide produced by TiO_2 film itself, the optical densities at different time were subtracted the initial triiodide in the I_2 in ACN solution with and without Li^+ ions. The results are shown in **Figure 6-6**b. A big difference between the two measurements in OD changes (ΔOD=0.7) after 55 min can be observed, which is due to the difference in the initial OD of triiodide, as lithium has already produced triiodide in solution before the immersion of the TiO_2 film. This indicates that less triiodide is generated with TiO_2 film in the presence of

Li^+ ions. Previous studies have shown that lithium cation changes the surface charge of TiO_2 film from negative to positive[159] and results in the positive shift of the TiO_2 conduction band energetics[160] The addition of Li^+ adsorbs onto negatively charged TiO_2 surface to make it positive and decreases the number of surface OH groups on TiO_2 surface. As such, less triiodide is generated by the TiO_2 film in the presence of Li^+ ion.

6.3.6 Water effect

As mentioned in the introduction, iodine reacts with water to produce hypoiodite, OI^-, protons and iodide (equation 1-10), whereas iodine can further react with iodide to form triiodide. In order to investigate the effect of water on the iodine-metal oxide interaction and also to clarify the mechanism of triiodide generation when the TiO_2 film is immersed into iodine acetonitrile solution, 1% water (20 µl) was added into iodine acetonitrile solution in the presence and absence of TiO_2 film. This amount of water is much more than that of a water saturated TiO_2 film (~0.24 µl, supposing all nanopores (Vv=2.4 x 10^{-4} cm^3) inside the TiO_2 film are filled with water). The results are shown in **Figure 6-7**.

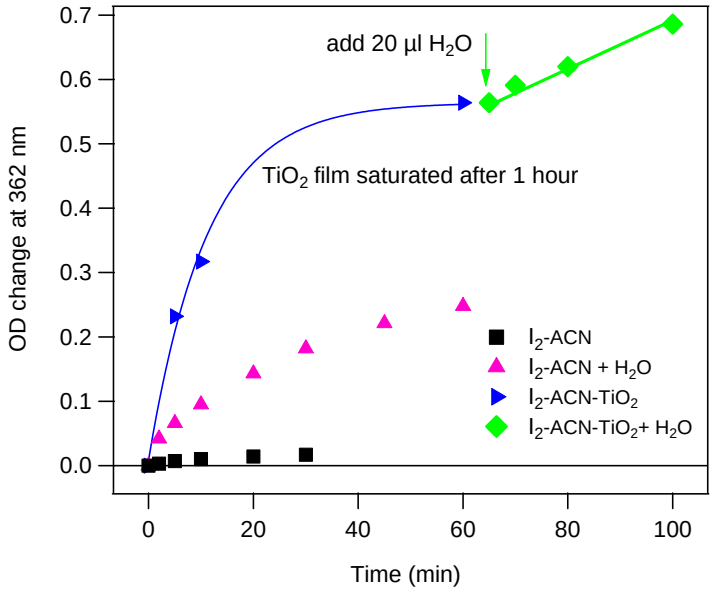

Figure 6-7. Change of optical density to time in the absence (**black**) and presence of the TiO_2 film (**blue**) with and without water addition (**pink** and **green**) in 0.2 mM I_2 acetonitrile solutions, respectively.

The amount of triiodide generated in I_2 acetonitrile solution after 30 min is estimated to be is ~6 nmol (with water only, pink triangle), ~20 nmol (with TiO_2 film, blue triangle) and ~4 nmol (with both TiO_2 film and water, green diamond) employing the extinction coefficient of 5.6 $x10^4$ M^{-1} cm^{-1} in ACN at wavelength of 362 nm. This difference may imply that the stabilisation of the ACN-I^+ cation by the TiO_2 nanopores suppresses the iodine-water reaction, and the water effect can be ignored in the iodine-metal oxide system.

6.3.7 Function of iodine-TiO_2 interaction in DSSC

The standard electrolyte applied in DSSC contains iodide/triiodide redox couple. The function of iodide is to regenerate the dye cation (Equation 1-3). The formed triiodide is subsequently reduced on the counter electrode (Equation 1-5). As the iodine-TiO_2 interaction produces triiodide, which then dissociates to iodine and iodide ((Equation 1-6), cells assembled with the electrolyte without added iodide ion might work. To investigate this, three cells with electrolytes containing 10, 50, and 100 mM iodine with 0.3 M tBP and 0.1 M $LiClO_4$ in MPN were assembled. Comparing the dark currents of these cells measured as a function of voltage (**Figure 6-8a**), it shows that the cell with 10 mM I_2 has a current limited by mass transport of ions in the electrolyte. Additionally, the more iodine added to the electrolyte, the smaller the *Jsc* is (**Figure 6-8b**). However, the difference between *Jsc* is not huge, although the trend is clear. Due to the equilibrium, Equation 1-6, the concentration of triiodide generated in the electrolyte containing 100 mM iodine is greater than that at low iodine concentration (e.g 10 mM iodine), but the iodide ions formed by reduction of triiodide are consumed by the excessive amount of iodine immediately. As a result, the *Jsc* of the 100 mM iodine device is the lowest among three cells. The S-shape of IV curve under light illumination may be due to the overpotential on the counter electrode.

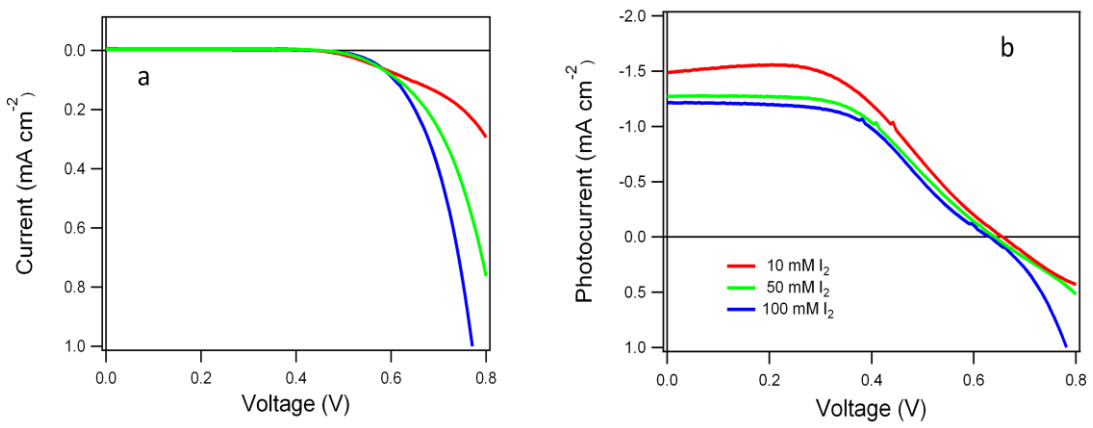

Figure 6-8. IV characterization of DSSC (a) dark current and (b) photocurrent with electrolytes containing 10, 50 and 100 mM iodine, 0.3 M tBP and 0.1 M $LiClO_4$ in MPN.

6.4 Discussion

Previous studies show that in organic solvent, the iodine-solvent interaction forms charge transfer complexes and triiodide.[151] In this chapter, this formation of triiodide has been increased in the presence of metal oxide films, such as TiO_2, Al_2O_3 and ZrO_2. Further tests with other redox couple such as Fc/Fc^+ show that this iodine – metal oxide interaction is a non-electrical interaction, and that metal oxide films are not catalysts for this process as they are saturated after one hour and only produce triiodide once without a reverse treatment. Moreover, these films cannot produce triiodide in non-polar solvent such as DCM where there is no triiodide ion generation from the I_2 in DCM solution.

To understand this iodine–metal oxide interaction, the surface properties of these metal oxide films were considered. All the metal oxide films tested here show triiodide generation. This probably relates to their surface hydroxyl groups (for a typical TiO_2 film, its surface hydroxyl density is 4~12 OH/nm^2).[161] These groups have been confirmed by FTIR spectroscopy[162], and can be estimated by thermogravimetric analysis (TGA)[161]. The surface OH of metal oxides attracts/binds to the Lewis acid[163], in this case $[ACN\text{-}I]^+$ in nanopores, leading to the diffusion of $[ACN\text{-}I]^+$ inside pores, probably with diffusion of protons into the bulk solution to maintain charge balance. The smaller amount of $[ACN\text{-}I]^+$ residing in the bulk solution changes the equilibrium

(**Equation 6-3**) by increasing the forward reaction. This will increase the amount of triiodide in bulk solution. Once the surface OH species on the metal oxides are consumed completely (after about 1 hour), the concentration of triiodide in bulk solution reaches a plateau (see **Figure 6-2** and **Figure A-7**).

Triiodide released in the bulk solution is about three times more with the 15 nm particle size TiO_2 film than with 400 nm particles, as shown in **Figure 6-3a.** This greater concentration of triiodide in bulk solution may result from the film's surface hydroxyl density. The smaller the particle size, the larger the surface area of the TiO_2 film, and the more surface OH groups, leading to more triiodide production. As the two TiO_2 films containing particles with different particle size were fabricated with different TiO_2 pastes, which were prepared through different synthetic processes, the surface properties are different. This could explain the three times difference in triiodide generation between the 15 nm and 400 nm TiO_2 films when the surface area of these films is different by 16 times. As the pore volume (Vv) within the films is similar for both particle size, it has no effect in equilibrium **Equation 6-3**.

From **Figure 6-8b,** the dye-sensitised solar cell with 10 mM iodine in the electrolyte (no addition of iodide) gives a photocurrent of 1.5 mA/cm^2, which is in agreement with the recent report in the literature by Andserson[156]. This implies that there is free iodide in the electrolyte to regenerate dye cations. The iodide may be produced by the dissociation of triiodide, which is generated by iodine interaction with solvent (MPN) and dye N719 (see next chapter). Regarding the cell with a electrolyte containing 100 mM iodine, the number of iodine molecules added is 250 nmol (= 100 mM x 2.5 µl, 2.5 µl electrolyte was added in the cell, see 2.4.1 in detail). It is more than the amount of iodine in the 0.1 mM I_2 acetonitrile solution in 2ml in cuvette (200 nmol). In the latter case, the triiodide generated is ~20 nmol, about a tenth of the amount of iodine. Assuming both the dye/TiO_2 film and TiO_2 film generate the same amount of triiodide (compare **Figure 6-3a** to **d**), the estimation of the triiodide concentration in the electrolyte gives a concentration of triiodide ~10mM. Then the concentration of iodide in the electrolyte can be calculated by employing the equilibrium constant of

Equation 1-6 to be $1x10^{-5}$ mM. This small amount of free iodide in the electrolyte may account for the current in these devices with no added iodide.

6.5 Summary

In this chapter, the iodine-metal oxide interaction is observed, and the effects of water, cation, and nanoparticle size on the reversible formation of triiodide ions were investigated. All metal oxide films are saturated with iodine after one hour in I_2 acetonitrile solution. The mechanism of this interaction may relate to the surface hydroxyl groups. This study enables an understanding of the diffusion and reaction of redox couples in the nanopores of TiO_2 films in dye-sensitised solar cells to improve cell performance.

Chapter 7 Iodine binding to ruthenium complexes adsorbed to nanocrystalline mesoporous TiO_2 films

The purpose of this chapter is to extend the results in last chapter further to address the interaction between iodine and different molecular structures adsorbed to TiO_2, and the effect of this interaction on the recombination of electrons from the TiO_2 with electron acceptors in the electrolyte of DSSCs.

7.1 Introduction

In last chapter, the results show that both TiO_2 films and dye/TiO_2 films can generate triiodide in solvents such as acetonitrile (**Figure 6-3a** and **d**). For dye-sensitised TiO_2 films, the formation of triiodide may relate to the iodine binding to the dye's electron donor atoms. The interaction of iodine with organic molecules containing electron donor groups (e.g -NCS, $-NH_2$) forming charge transfer (CT) complexes was first published in 1961.[164] Among those organic molecules, pyridine has been studied the most. Hassel et al[164] determined the structure of $(Pyr)_2I^+$ by X-ray crystallography from its salt and found the N-I bond. Rao et al[150,151] also observed the $(Pyr)_2I^+$ band at 280 nm (in non-polar solvents) in the absorption spectrum. Ma et al[165] used the surface enhanced Raman spectra (SERS) to identify the iodine-pyridine charge transfer complexes on the Ag electrode. This is also confirmed from the comparison of the infrared absorption spectra of iodine-pyridine crystalline complex and pyridine. In this iodine-pyridine interaction, pyridine acts as a σ donor and iodine as a σ* acceptor, which forms $(Pyr)_2I^+$ complex and triiodide ion.[151] The equilibrium constant of iodine to pyridine ranges from 63 to 140 M^{-1} (25 ^oC) according to different authors.[150]

In addition, studies on the charge transfer complexes between iodine and electron donors containing sulfur atoms showed that iodine binds to sulfur atoms through its lone pair electron. Plahte et al[166] observed a weak interaction between iodine and isothiocyanate (R-N=C=S), such as ethyl isothiocyanate and allyl isothiocyanate. Greijer et al[167] studied the formation of iodine-thiocyanato complex by FTIR and Raman spectra in sealed DSSCs. Orszagh et al[168] found that the charge transfer complex produced in the iodine thiocyanate (R−S−C≡N) interaction in water was I_2SCN^- with a binding constant of 53 M^{-1}. There is a wide range of binding constants for different donors from 0.5 to 2410 M^{-1} which may depend on the donor strength of the donor group of molecules.[150]

In DSSCs, literature publications show that the interaction between iodine and dyes adsorbed on TiO_2 surface influences cell performance. The binding of iodine to dyes, such as phthalocyanines[29], porphyrins[169], ruthenium dyes[170] and organic dyes[171], has a key role in determining the recombination kinetics of electrons photoinjected into the TiO_2 conduction band with the electrolyte (Equation 1-7). This recombination reaction proceeds via electron transfer either to I_3^- ions or directly to I_2. Moreover, an increase of iodine concentration in the electrolyte leads to an increase of recombination and thus a reduction of photocurrent.[172] The increase in recombination in the presence of certain dyes can be interpreted as iodine binding to dye molecules increasing the local iodine concentration near the TiO_2 surface, resulting in an increase of the recombination losses. A previous paper shows that iodine binding to amino groups (NH_2), such as in 4-aminobenzoic acid (PABA) in the electrolyte, decreases the recombination lifetime 5 times more for PABA than p-acetylamino benzoic acid (PACA), causing a drop in cell *V*oc, as shown in **Figure 7-1**.[37] Recently, the intermolecular interaction between organic dye molecules with thiophene ligands and iodine or triiodide (in the electrolyte in DSSC) has been reported by theoretical calculation and measurements of recombination kinetics.[171] The same dyes in cobalt complex electrolyte showed no interaction and slow recombination, which might be due to the large size of cobalt complex, whose larger steric hindrance prevented the increase of its concentration near the surface of TiO_2.

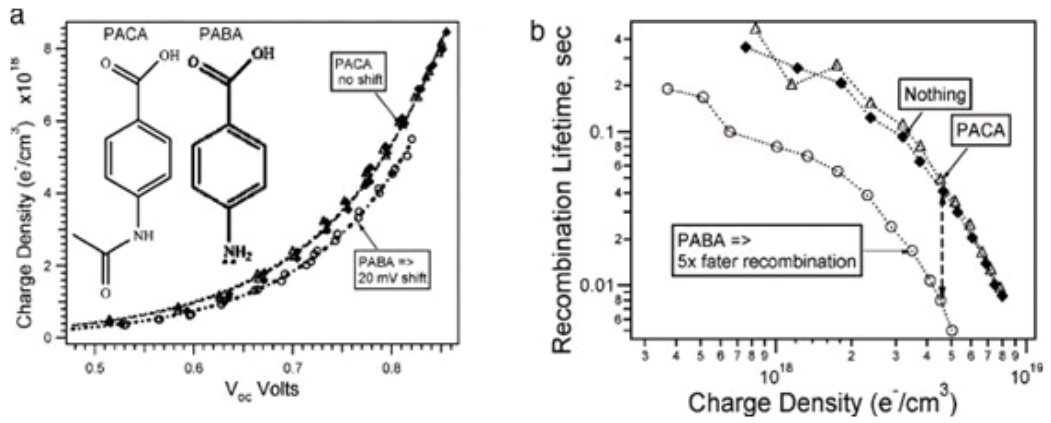

Figure 7-1. (a) Electron density in TiO_2 versus Voc for various electrolyte additives. (b) Recombination lifetime versus electron density for the same cells. Reproduced from reference[37].

In this chapter, the interaction between iodine and three ruthenium dyes adsorbed to TiO_2 has been studied via measurements of UV-Vis and Fourier transform infrared spectroscopy (FTIR). These three dyes are named N719, C101 and AR24[173], and their molecular structures are shown in **Scheme 7-1**.

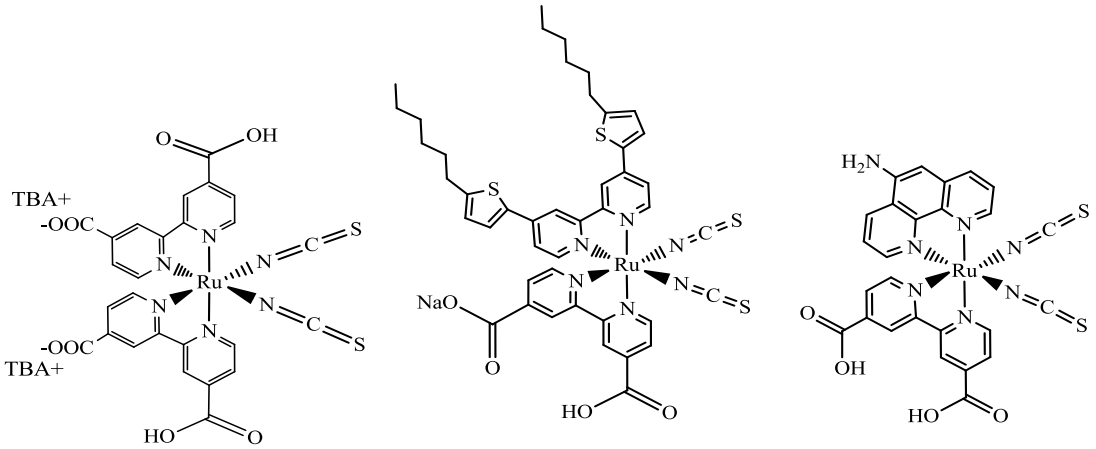

N719 C101 AR24

Scheme 7-1. Chemical structures of N719 (left), C101 (middle) and AR24 (right).

C101 and AR24 molecular structures are similar to that of N719: C101 has thiophene substitutes while AR24 has a 5-amino-1,10-phenanthroline substitute. Both C101 and AR24 dyes are used herein as comparable dyes to N719. Iodine could bind to these three dyes via their electron donor groups, such as thiocyanate, thiophene (in C101 dye) and amine (in AR24 dye) ligands. In addition, in order to investigate the

influence of iodine binding on the charge recombination, cells were prepared with these dyes. These iodine binding studies have implications for optimizing the dye structure and the electrolyte composition and thus improving the cells' efficiency.

7.2 Experimental section

N719 dye was purchased from Dyesol (Queanbeyan, Australia), C101 dye was obtained from EPFL and AR24 dye was synthesized by Dr.Anna Reynal, as described elsewere[173].

Film sensitisation. Nanocrystalline, mesoporous TiO_2 and Al_2O_3 films were fabricated on microscope slides (VWR) by doctor blading the TiO_2 and Al_2O_3 paste (see 2.1.2 and 2.1.3). Films sensitizations were carried out by overnight dipping of TiO_2 and Al_2O_3 films into dye solutions: 3×10^{-4} M N719 and C101 in 1:1 (v/v) acetonitrile and *tert*-butanol solution, and 1×10^{-4} M AR24 in dimethylformamide (DMF) solution, respectively. Dye-sensitised films were rinsed in acetonitrile for 20 minutes prior to iodine binding tests. Sensitized films were named as N719/TiO_2, C101/TiO_2, AR24/TiO_2, N719/Al_2O_3 and AR24/Al_2O_3 films.

Iodine titration. The absorption spectra of the dye sensitised films were recorded using a UV-Vis Spectrophotometer. The iodine dye interactions were examined by measuring the absorption spectra of dye-sensitised films (area of 0.9 cm^2) under iodine titration in acetonitrile (ACN) and dichloromethane (DCM) in a 10 mm cuvette, where a series of I_2 acetonitrile solutions were added from its 0.01 M stock in the presence of dye/TiO_2 films.

In detail, iodine titrations were carried out in a 10 mm cuvette containing 2 ml acetonitrile where dye-sensitised films were placed, and the absorption spectra at different iodine concentrations were recorded**.** Control experiments were performed by using blank TiO_2 and Al_2O_3 films with no dyes. Baselines were measured in air. The absorbance of dye-sensitised films (OD_{film}) at each wavelength were obtained by

Equation 7-1, which corrects the total absorption by subtracting the absorption of iodine in solution.

$$OD_{film} = OD1 - 0.9 \times OD2 \qquad \textbf{(Equation 7-1)}$$

where OD1 is the absorbance of dye-sensitised films in iodine solution (i.e, film in beam) and OD2 is the absorbance of iodine solution (i.e. film out of beam but still immersed in solution); the subtracting factor 0.9 corrects the beam pathway (10 mm) by subtracting the thickness of microscope slide (1 mm).

Cell assembly. Glass based dye-sensitised solar cells were fabricated with three dyes according to the process as described in 2.4.1. The TiO_2 films were fabricated on FTO glass by doctor blading the commercial TiO_2 paste (DSL-18NRT, Dyesol, particle size ~20 nm). Two sets of cells were assembled: one set of cells use N719 and C101 dye-sensitised films without any treatment as the working electrodes employing E1 electrolyte (described below), and the other set cells employ AR24 and N719 dye-sensitised films presoaked in E2 electrolyte (also described below) for 2 hours prior to cell assembly. The electrolyte E1 contained 0.8 M 1-methyl-3-propylimidazolium iodide (PMII), 0.05 M iodine (I_2), 0.05 M guanidinium thiocyanate (GuSCN), 0.025 M lithium iodide (LiI) and 0.28 M *tert*-butylpyridine (tBP) in 3-methoxypropionitrile (MPN), and E2 consisted of 0.6 M PMII, 0.1 M I_2, 0.1 M LiI in MPN. Cell characterization were determined by the solar simulator and the transient rig as detailed in 2.4.2 and 2.4.3.

7.3 Results

7.3.1 Absorption spectra of N719/TiO_2, C101/TiO_2 and AR24/TiO_2 films upon iodine titration

To investigate quantitatively the interaction between iodine and dyes, the absorption changes of dye/TiO_2 films in acetonitrile were recorded upon iodine titration. The absorption spectra of dye sensitized TiO_2 films with the iodine concentrations ranging from 0 to 350 μM were shown in **Figure 7-2** (and **Figure A-12** in DCM).

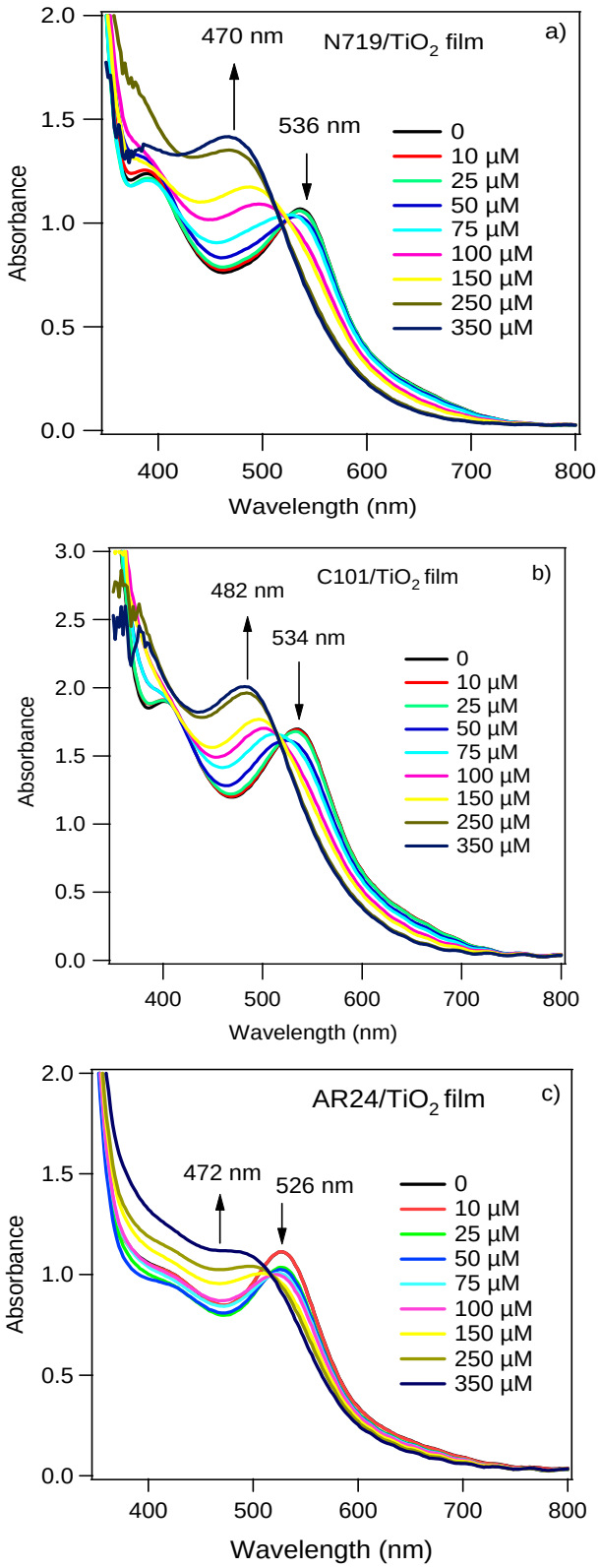

Figure 7-2. The absorption spectra of (a) N719/TiO_2 film, (b) C101/TiO_2 film and (c) AR24/TiO_2 film in acetonitrile upon iodine titration.

In the control experiment, a blank TiO_2 film was employed. It shows negligible changes of the optical density in the visible region (**Figure A-13**), this makes it feasible for measuring the absorption spectra of adsorbed dye molecules.

In **Figure 7-2**, new complexes are formed in a range of 470~482 nm in absorption spectra for all dyes. And the triiodide peak at 362 nm was also observed in the solution absorption spectra (film out of beam, **Figure A-14**). The absorbances of dye metal-to-ligand-charge transfer (MLCT) peak at ~535 nm (Ru-NCS) were decreased during iodine titration. This implies that the iodine binds to the lone pair of electrons in sulfur atoms on the NCS ligands of the dye molecules.

7.3.2 Absorption spectra of N719/Al_2O_3 and AR24/Al_2O_3 films

In **Figure 7-2**, the absorbance of dye/TiO_2 films in the presence of iodine in ultraviolet region was too high for accurate measurements due to the absorbance of TiO_2 film itself (**Figure 2-6**). As such, dye peaks in the range of 300 to 400 nm cannot be observed. To investigate the absorption of iodine dye complexes in this region, dye N719 and AR24 were adsorbed on Al_2O_3 films which show negligible absorption between 300 and 400 nm (**Figure 2-6**). The absorption spectra of N719/Al_2O_3 and AR24/Al_2O_3 films upon iodine titration are shown in **Figure 7-3**. The MLCT band (at 540 nm for N719 and at 520 nm for AR24) shows a blue shift in the presence of iodine. This blue shift could be related to the iodine dye (-NCS) interaction (also shown in **Figure 7-2**). However, the absorption peak of AR24 dye at 374 nm shows almost no change/shift (slightly shift from 374 nm to 368 nm, 6 nm shift) as iodine is introduced, while the one for N719 shows a significant blue shift (from 392 nm to 368 nm, 24 nm shift). DFT calculation (**Figure A-15**) shows that this 374 nm peak of AR24 dye relates to the HOMO to LUMO+1 transition (the LUMO+1 is a phenanthroline π^* orbital with substantial contributions from the $–NH_2$ group). As iodine could possibly bind to the nitrogen atom in $–NH_2$ group in phenanthroline, the 374 nm peak is shifted to a longer wavelength. Therefore, no significant shift observed at 374 nm for AR24 implies a simultaneous iodine binding to both –NCS (HOMO level) and $–NH_2$ (LUMO+1 level) of AR24 dye.

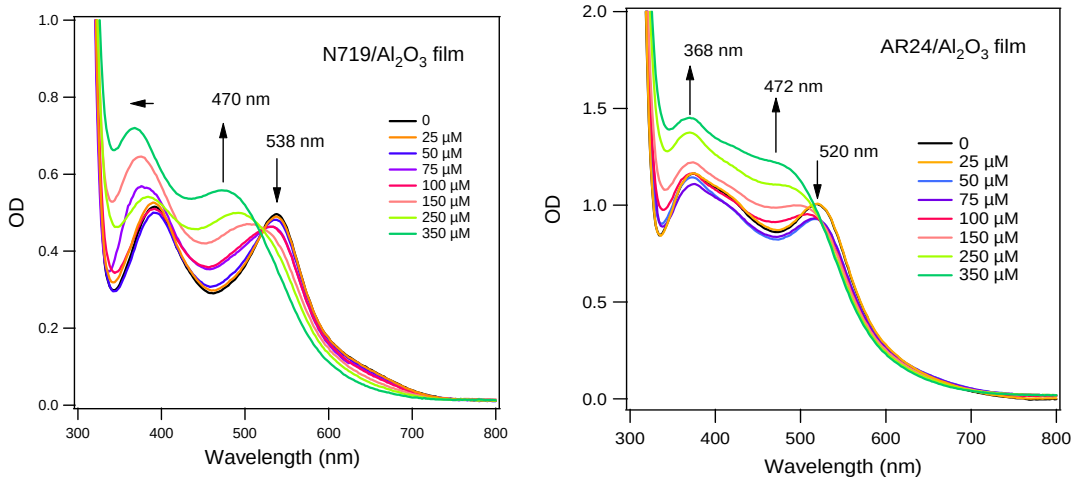

Figure 7-3. The absorption spectra of the N719/ Al_2O_3 and AR24/Al_2O_3 upon the iodine titration. The MLCT at 392 nm was blue shifted to 368 nm for N719 dye as iodine added.

7.3.3 Iodine dye binding constant

Dye loadings on 0.9 cm^2 TiO_2 films (projected area) are 93, 96 and 108 nmol for N719, C101 and AR24, respectively, which were calculated by Beer-Lambert law employing the molar extinction coefficient of 12,000 $M^{-1}cm^{-1}$ at wavelength 535 nm for N719, 17,500 $M^{-1}cm^{-1}$ at 534 nm for C101 and 9,242 $M^{-1}cm^{-1}$ at 528 nm for AR24, respectively.[5,26,173] At the full monolayer dye coverage, ${}^{s}\Gamma$ (the density of surface loaded dyes) is estimated to be 2.3, 2.4 and 2.7 µmol/m^2 for N719, C101 and AR24 (Equation 2-7), which corresponds to 1.4×10^{18}, $1.45 \times 10^{18}$and 1.6×10^{18} molecules per m^2 TiO_2 surface. Additionally, the estimated surface area one dye molecule occupies, S_{mol} (=$1/({}^{s}\Gamma \times N_a)$, N_a is the Avogadro number, Equation 2-8) is estimated to be 70, 67 and 60 $Å^2$ or 0.7, 0.67 and 0.6 nm^2 for N719, C101 and AR24 respectively, which is in reasonable agreement with the molecular dimension determined from the modelling[143,144].

The changes of optical density *vs* the iodine concentrations at 560 nm and at the new iodine dye complex peak (470 nm for N719, 482 nm for C101 and 472 nm for AR24) were plotted in **Figure 7-4** and **Figure A-16**. The binding constant, K_f, is the overall equilibrium constant, defining the strength of interaction between iodine and dye molecules. It can be estimated by fitting the points with **equation 1-14.** The results

are listed in **Table 7-1**. Also plotted in **Figure 7-4** were the change in optical density for control TiO_2 film and a control dye named Z995[174] (no –NCS ligands) for comparison.

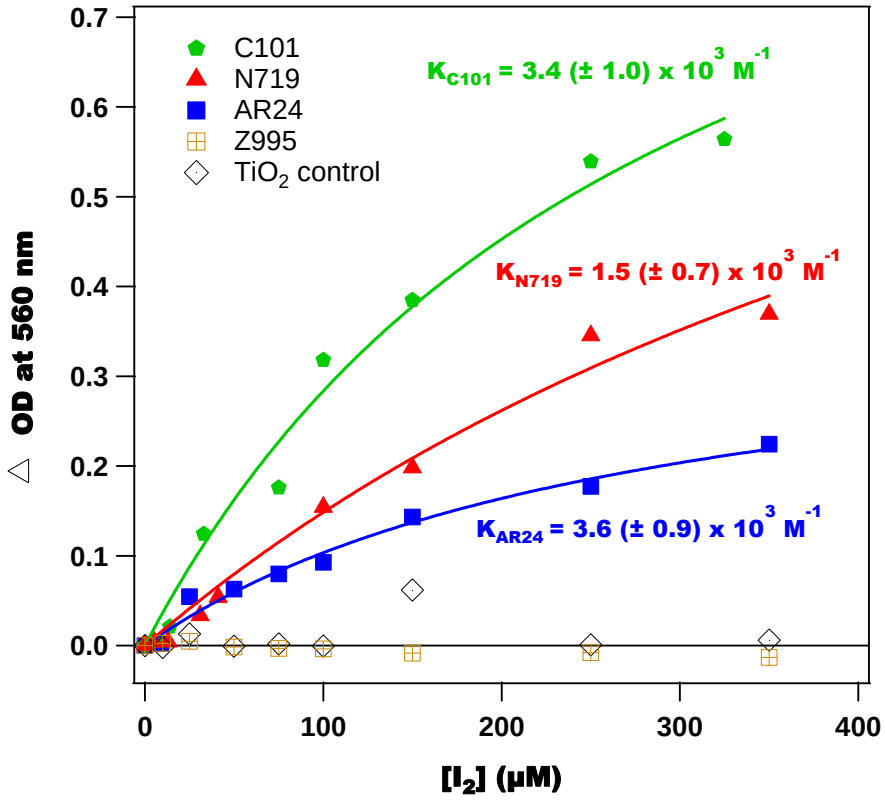

Figure 7-4. The absorbance changes at 560 nm (=A_0-A) vs the iodine concentration for the TiO_2 film, C101/TiO_2 film, N719/TiO_2 film, AR24/TiO_2 film and Z995/TiO_2 film. The structure of Z995 is similar to N719 with one more bipyridine to replace the two –NCS ligands.

Table 7-1 The binding constant for dyes in solution and on TiO_2 films

No.	Dye/TiO_2 film	solvent	K_f, M^{-1}	
			At 560 nm	At CT band
1	N719	ACN	1.5 (± 0.7) x 10^3	2.4 (± 0.5) x 10^3
2	C101	ACN	3.4 (± 1.0) x 10^3	2.7 (± 0.5) x 10^3
3	AR24	ACN	3.6 (± 0.9) x 10^3	2.0 (± 0.5) x 10^3
4	Z995	ACN	0	0
5	N719	DCM	4.1 (± 0.4) x 10^3	2.8 (± 0.2) x 10^3
6	N719 solution	ACN		4.4 (± 1.1) x 10^4

The binding constant of iodine to dyes are found to be 1.6 (± 0.7) x 10^3, 3.4 (± 1.0) x 10^3 and 3.6 (± 0.9) x 10^3 M^{-1} at 560 nm for N719, C101 and AR24, respectively, within the same order of magnitude. As the difference in dye structure between N719

dye and C101 dye or AR24 dye are the presence of the thiophene groups (in C101 dye) or the amine group (in AR24 dye), the relatively high binding constant of C101 and AR24 dyes may be due to the weak interaction between iodine and thiophene or amine ligands. However, the electron pairs on sulfur in thiophene ligands (in C101 dye) are delocalized in the π-electron system[175], this iodine binding is much weaker than the iodine binding to the sulfur atoms in -NCS ligands.

Comparing these numbers to literature, the order of the magnitude of binding constant of my results is the same as iodine binding to diethyl sulfide (2410 M^{-1} at 20C in CCl_4)[150], although they are more than 10 times bigger than that to isothiocyanate. At the new complex band, analogous analysis of the data for the N719/TiO_2 film in dichloromethane (DCM) yields a similar iodine-N719 binding constant of 2.8 (±0.2) x 10^3 M^{-1} to the film in ACN (**Figure A-17**), which implies a similar reaction mechanism between iodine and N719 dye in both acetonitrile and dichloromethane solutions. For N719 dye in ACN solution upon iodine titration (**Figure A-18**), the solution iodine binding constant is 18 times bigger (4.4 (±1.1) x 10^4 M^{-1}) than N719/TiO_2 film in ACN solution, indicating a stronger interaction of iodine to dye in solution.

7.3.4 FTIR spectra of N719/TiO_2 films exposed to iodine

Further investigations were carried out to scrutinize the interaction between iodine and sulfur atoms by infrared absorption spectrum of N719/TiO_2 in the absence and presence of iodine, undertaken by Dr Robin Humphry-Baker (EPFL, Switzerland), as shown in **Figure 7-5**.

The -NCS peak appears at 2104 cm^{-1}, is in good agreement with literature report[176], which is assigned to the antisymmetrical stretching band. The surface binding carboxylates are seen at 1384 cm^{-1} and under 1608 cm^{-1}. In the presence of the iodine, the intensity of -NCS peak is reduced and a new shoulder appears at a slightly higher frequency of 2124 cm^{-1}. For C101 dye, similar results were obtained (see **Figure A-19)**.

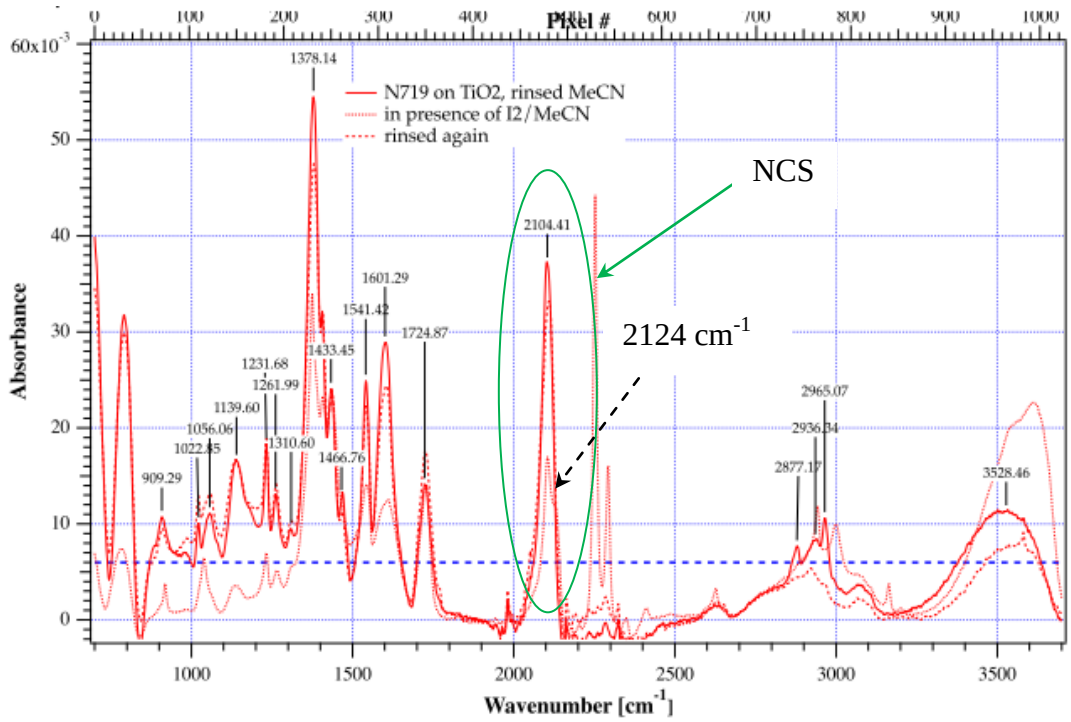

Figure 7-5. FTIR spectrum of N719 on the TiO_2 surface in the presence and absence of iodine for 20 min. (Surface water has been removed in the data processing) This work was done by Dr Robin Humphry-Baker at EPFL.

7.3.5 Charge recombination and transport/collection

To understand the shifts in the absorption peak at a wavelength of 368 nm of N719 and AR24 dyes in the presence of iodine, dye-sensitised solar cells with these dyes were further made and the recombination kinetics were investigated. Previous work[173] reported AR24 cells showed the photocurrent was 10 times less than N719 cells with a electrolyte containing a base (in this case, tBP), this is related to poor electron injection. To avoid this, the electrolyte used herein did not consist of any base. To keep the cells' TiO_2 conduction band edge (CBE) at the same position, *i.e.* at the same potential (relative to iodine/iodide), dyed TiO_2 films were soaked with the electrolyte for 2 hours prior to cell assembly. In order to compare recombination lifetimes of these cells, transient photovoltage and photocurrent measurements and charge extraction were carried out. The experimental results are depicted in **Figure 7-6**.

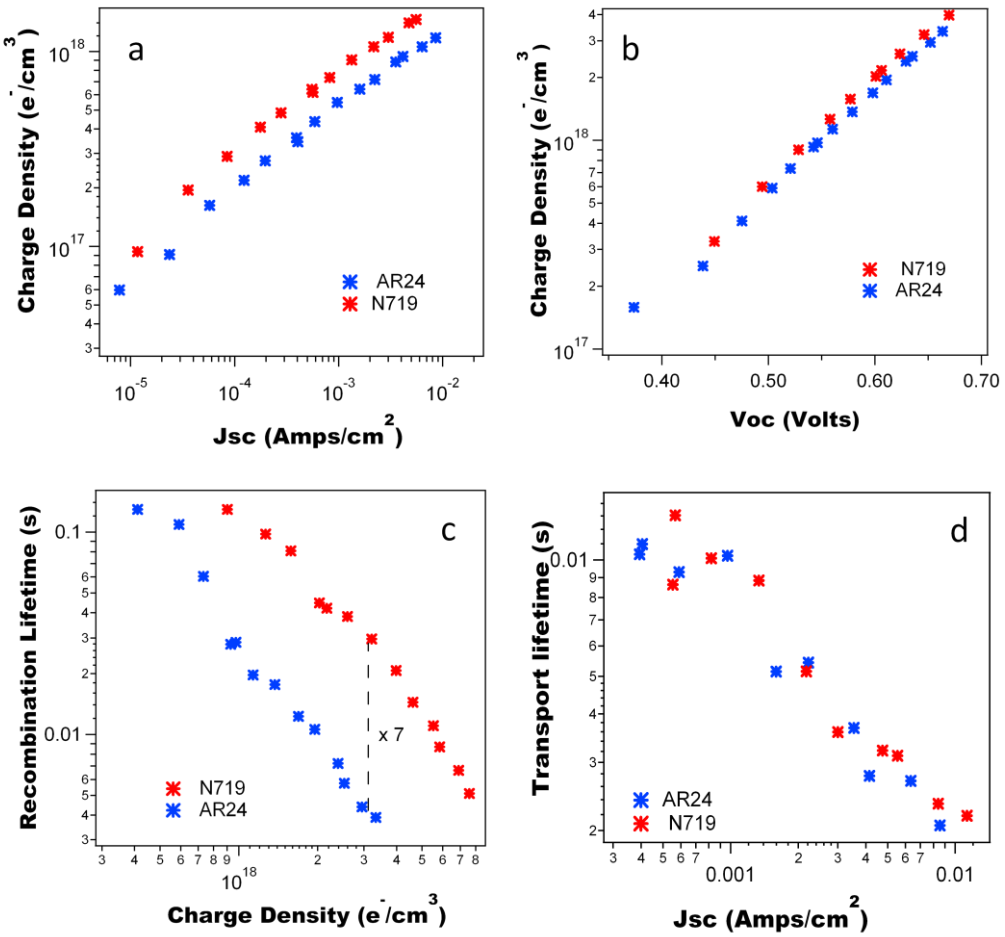

Figure 7-6. Charge in the cells with AR24 (**blue**) and N719 (**red**) dyes plotted as a function of (a) Jsc and (b) Voc, where the Voc was varied by changing the bias light intensity; (c) Recombination lifetimes *vs* charge density measured at V_{oc} and (d) Transport lifetime plotted against *Jsc* measured at a short circuit. **E2** electrolyte is used.

Figure 7-6a shows the charge extracted from the cells at short circuit. The small difference (less than 2 times) between two dyes may correspond to the slight different electron trap density. Comparing the charge in the cell for two dyes at the same Voc, as shown in **Figure 7-6b**, the concentration of electrons in the TiO_2 conduction band in the N719 cell is the same as in the AR24 cell. This implies that the two cells have the same TiO_2 conduction band edge (CBE). The electron lifetime τ_n, measured at *Voc* controlled by the bias light intensity, as a function of the charge density, is presented in **Figure 7-6c**. From **Figure 7-6c**, the N719 cell shows around 7 times longer electron lifetime than the AR24 cell. This may be related to iodine binding to the amino groups on phenanthroline group of AR24 dyes. Meanwhile, as can be seen in **Figure 7-6d**, the transport lifetimes for two dyes are the same.

In addition, the charge recombination of N719 cells is also compared to that of C101 cells, as shown in **Figure A-20**. At the same *Voc*, the concentration of electrons in the N719 cells is similar to that in C101 cells (1.8 times bigger for N719 than C101, **Figure A-20b**). The charge vs *Voc* curve for C101 dye is shifted to ~60 mV higher voltages than that for N719 dye (**Figure A-20b** and **Figure A-21**). This shift can be interpreted as a 60 mV upward shift in TiO_2 conduction band. From **Figure A-20c**, N719 dye shows slight longer electron lifetime (2.5 times) at *Voc* than C101 dye. Meanwhile, the transport lifetime in **Figure A-20d** shows the same for both N719 and C101 dyes.

7.4 Discussion

The interaction between iodine and dyes adsorbed on TiO_2 surface in dye-sensitised solar cells may increase the recombination and thus decrease the cell's *Voc*.[37] The formation of iodine-dye complex could localise iodine near the dye/TiO_2 surface which enhances recombination reaction (Equation 1-7) and reduce the average numbers of dye molecules available for light harvesting. Both cases may reduce the cell efficiency via a decrease in *Voc* or *Jsc*.

In last chapter, the reaction mechanism between iodine and donor is assumed that the outer complex (DI_2) is formed first and then it transforms to inner complex which further reacts with iodine to generate triiodide, as listed in **Equation 6-1** and **Equation 6-2**. From **Figure A-14**, a large amount of triiodide is generated in acetonitrile solution with the N719/TiO_2 film during the iodine titration. For example, 104 nmol triiodide generated (i.e. 1 triiodide per dye) under 700 nmol iodine addition (estimated by using the absorbance of triiodide peak at 362 nm in **Figure A-14** employing the extinction coefficient of triiodide of 5.6×10^4 $M^{-1}cm^{-1}$), which means about 15% iodine has been converted to form triiodide.

On the other hand, also shown in **Figure A-14**, in dichloromethane the formation of triiodide is 16 nmol (2 triiodide per 10 dyes) under the same amount of iodine (estimated by employing the extinction coefficient of triiodide of 3.3×10^4 $M^{-1}cm^{-1}$),

which is less than 3% of added iodine and can be ignored. This implies that the reaction between iodine and dye N719 in dichloromethane only forms the outer complex, DI_2. As the binding constants in two solvents are almost the same, it can be suggested that the outer complex DI_2 is formed in acetonitrile as well. The triiodide generated in acetonitrile in the presence of the N719/TiO_2 film may not be due to iodine-dye interaction, but is possibly from the reaction between acetonitrile and iodine which is then increased by the TiO_2 film, as shown in **Figure A-14**.

The binding constant (K_f) of iodine to dyes ranges from 2,000 to 4,000 M^{-1}, which is in the same order of magnitude for the three dyes studied. From **Figure 7-2**, clear isosbestic points for N719 and C101 dyes were observed, which implies that one complex is formed. However, for AR24 dye, there is no clear isosbestic point, implying that more than one complex is formed. These complexes may be a result of the binding of iodine to –NCS and/or $–NH_2$ group in AR24 dye. The bigger binding constants of iodine to these three dyes than other donor molecules, such as isothiocyanate and pyridine implies stronger interactions between iodine and dye. This stronger binding might be due to the negative charged –NCS in dyes (as Ru is positively charged) that enhances the electron density in sulfur atoms.

To understand the difference in recombination rate between N719 and AR24, a comparison of the estimated number of iodine molecules brought near to the TiO_2 surface via iodine binding to dyes was made. In typical electrolytes used in DSSCs, the added concentrations of iodine and iodide are 0.1 M and 0.8 M, respectively. The free iodine concentration in the electrolyte can be estimated by employing the equilibrium constant (*Keq* is ~10^7) of equation 1-6 in acetonitrile[38] to be of 10^{-8} M. As the iodine concentration is buffered due to the high concentration of iodide (0.8 M) and triiodide (0.1 M), the number of DI_2 generated per TiO_2 particle is estimated to be 1.0 x 10^{-2} and 3 x 10^{-2} for N719 and AR24 dyes, respectively (where $1>>K_f[I_2]$ at $[I_2]=10^{-8}$ M, calculation details can be seen in **Table 7-2**). As a result, the number of iodine near the TiO_2 surface for AR24 is around 3 times more than that for N719 dye. This might be expected to correspond to an increase in the recombination rate, however if the relationship is linear, the difference cannot fully explain the 7 times

faster electron recombination of AR24 relative to N719 (and the corresponding 80 mV shift in Voc while the conduction band edge is at the same level). This is not consistent with a previous measurement which showed a first-order recombination reaction between electrons and iodine[172]. In addition, at the new complex band, the binding constants (**Table 7-1**) for AR24 and N719 are similar. As the amino group in AR24 dye also interacts with iodine, the iodine binding to AR24 is more complex than to N719. Further calculation of the fractions of DI_2 to dye (=DI_2/D= K_f [I_2]) are 0.002% and 0.004% for N719 and AR24, which implies the dye loss is very small due to the iodine binding.

Table 7-2 Number of iodine and DI_2 near TiO_2 surface

Film*	**N719/TiO_2**	**AR24/TiO_2**
Dye loading *n*, nmol/cm^2	93	108
the numbers of dye per TiO_2 particle (= *n* x *Na* / (9 x 10^{13}))	622	723
the number of DI_2 per TiO_2 particle (=K_f x [I_2] x numbers of dye per TiO_2 particle)	1.0 x 10^{-2} (=1600 x 10^{-8} x 622)	2.6 x 10^{-2} (=3600 x 10^{-8} x 723)
fraction of DI_2 to dye (=DI_2/D= K_f [I_2]),	0.002%	0.004%

*4 μm 1cm^2 thick TiO_2 film; The number of TiO_2 particles in film is 9 x 10^{13} (60% porosity); the K_f used in above table is selected from the Table 1 at 560 nm; *N*a is Avogadro number (6.023 x 10^{23} mol^{-1}).

Previous density functional theory (DFT) calculations of neutral dyes confirmed HOMO orbitals localised upon the NCS groups for all these three dyes molecules[25,173,177], which are essentially ruthenium t_{2g} orbital character with sizable contribution coming from the NCS ligand orbitals, while the LUMO orbitals are on bipyridine anchoring to the TiO_2 surface. For AR24 dye, the LUMO+1 orbital is localised upon the phenanthroline π* orbital and the LUMO+1 is again a phenanthroline π* orbital with substantial contributions from the –NH_2 group (**Figure A-15**). This may imply that the iodine binding to this dye could change both HOMO and LUMO+1 energy levels, and show either a blue or a red shift in its absorption spectra.

As shown in **Figure 7-2** and **Figure 7-3**, there are blue shifts in the MLCT band for dye-sensitised films as the I_2 concentration increased, *i.e*. from 536 to 470 nm (66 nm) for N719 dye, from 534 to 482 nm (52 nm) for C101 dye and from 526 to 472 nm (54 nm) for AR24 dye. As stated in **1.2.3.2,** molecular interactions form CT complexes can shift the absorption spectra. The possible sites of iodine binding to three dyes are the donor atoms such as sulfur and nitrogen atoms due to their lone pair electrons. Previous studies have shown that this MLCT band of dyes appears at low energy to be composed of the transitions from the Ru-NCS sets of HOMO to the sets of LUMO and LUMO+1 (from the occupied 4d orbitals of ruthenium to the lowest unoccupied π^* orbitals of the anchoring bipyridine ligands).[25,177] Within the NCS ligands, the amplitude is located on the sulfur atom.[178] As such, these blue shifts may be due to a reduction of the HOMO-LUMO and HOMO-LUMO+1 gaps. As an electron acceptor, iodine binds to the donor, which herein is the sulfur atoms in dyes and thus decreases the dyes' HOMO level. Furthermore, these spectra shifts are also confirmed by FTIR measurements, i.e. the bond strength of –NCS ligands is changed. Although *Voc* losses are not large in current "record" N719 and C101 DSSCs, it is useful to be aware of the interaction between redox couple and dyes in the electrolyte when aiming to improve a cell's performance.

On the other hand, in the presence of iodine, a large blue shift in shorter wavelength was also observed for N719 dye (from 392 nm to 368 nm) but not for AR24 dye (only 6 nm shift, from 374 nm to 368 nm). It is predicted by DFT calculation that the peak at 374 nm for AR24 is due to the HOMO to LUMO+1 transition, in which the lone pair of the nitrogen atom in the phenanthroline has a strong contribution. Iodine binding to the electron-donating $–NH_2$ group in the phenanthroline ligand (LUMO+1) could decrease the energy level of LUMO+1 simultaneously with the decrease of HOMO level (iodine binding to –NCS group), resulting in no change of the HOMO to LUMO+1 gap, as depicted in **Scheme 7-2.**

The oxidative degradation of NCS ligands in ruthenium dyes has been observed previously.[85,145] This iodine binding to the NCS ligands of dyes also implies that the replacement of NCS ligands is needed. However, the NSC groups determine the

metal-to-ligand charge transfer (MLCT) band at ~535 nm which is important for a high light harvesting efficiency and thus a high *Jsc* for cells. Therefore, a compromise has to be made to obtain a high *Jsc* with the cost of *Voc* loss by iodine binding.

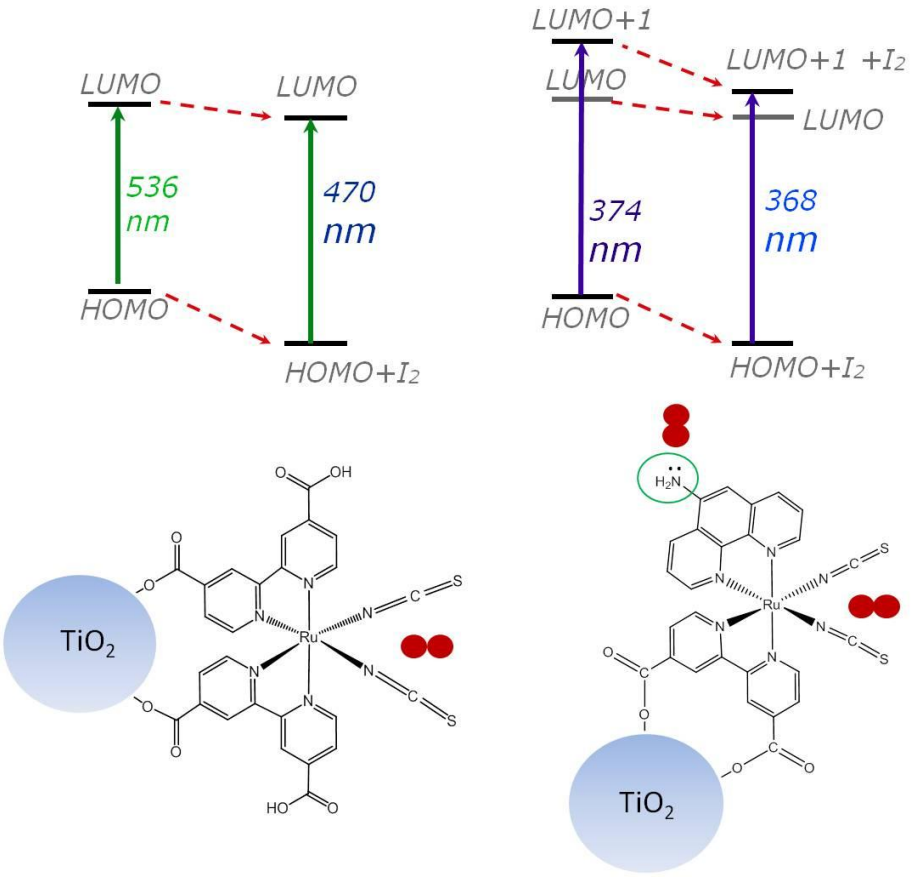

Scheme 7-2. Scheme of the interaction between N719 (left) and AR24 (right) and iodine.

7.5 Summary

In this chapter, the evidence of iodine binding to dyes via the sulfur and/or nitrogen atoms of dyes has been found in blue/red shifts in dye absorption spectra. These shifts can be related to the change of dyes' energy levels and the *Voc* loss in cells. These iodine dye interaction observations imply further studies could be carried out in modification of dye structure via replacement of NCS ligand with other electron donor groups[179,180], and use of new redox couples to replace iodine/iodide couple in the electrolyte, such as Co^{III} /Co^{II} complex[42,181,182] and ferrocene/ferrocenium[183].

Chapter 8 Conclusions

In this thesis functionalised nanocrystalline, mesoporous, metal oxide films functionalised by molecular receptors, such as ruthenium complexes have been investigated. These films can be used in a wide range of applications, such as optical sensing, pollutant scavenging, cation/hole percolation for molecular wiring, and in dye sensitized solar cells. This can be achieved by changing molecular receptors to suit the application.

This chapter highlights the most important results already discussed in previous chapters.

Cyanide sensing: It is found that functionalised nanocrystalline mesoporous Al_2O_3 films can be used to sensing anion in a more basic solution, for example, at a high pH value (>9), such as cyanide which acidic form is very toxic. Meanwhile, modification of organic compounds with anchoring group can construct colorimetric anion sensor and thus is attractive for detecting the anions in wastewater without further treatment.

Mercury scavenging: It is demonstrated that the functionalised nanocrystalline mesoporous N719/TiO_2 films can be used for a practical approach of mercury removal in aqueous solutions. This film has shown that not only high scavenging efficiency at low mercury concentrations, but also high selectivity towards mercury ions which can selectively bind mercury even at a high concentration of interfering cations. It is an ideal mercury scavenging material and overcomes all the limitations of current scavenging methods.

Hole percolation: The donor-acceptor dye functionalised nanocrystalline, mesoporous TiO_2 films exhibits faster hole percolation. This enables its applications in the molecular wiring of otherwise insulating inorganic films for percolation batteries and molecular nanotransistors. Meanwhile, the cation percolation can also be applied for voltammetric mercury sensing. However, this shift of HOMO orbitals does

not stabilise the -NCS groups while dye molecule is oxidized. Therefore, a more stable dye is needed.

Iodine-metal oxide interaction: Triiodide is observed in iodine ACN solution and the amount of triiodide is increased in the presence of metal oxide films. This iodine-metal oxide interaction is further analysed under the influence of water, cation, and particle size. The surface hydroxyl groups on metal oxide is ascribed to account for the stabilisation of $[ACN\text{-}I]^+$ ions and the increase of the amount of triiodide in ACN solution. This observation enables us to understand the diffusion and reaction of redox couples in the nanopores of TiO_2 films in dye-sensitised solar cells to improve cell performance.

Iodine binding: Iodine binding to dyes, N719, C101 and AR24 via the lone pair sulfurs and/or nitrogen atoms has shifted the absorption spectra in blue or red. These shifts can be related to the electron accepting ability of donor/acceptor group in dye molecules and the change of dyes' HOMO-LUMO gap and energy levels. Additionally, iodine binds to dye molecules may increase the charge recombination and decrease the DSSC's *Voc*, and then the cell's efficiency. These observations imply further studies in the modification of dye structure and the use of new redox couples to replace iodine/iodide couple in the electrolyte.

I hope my studies presented here can be extended in the future to understand more basic science of functionalising metal oxide films and broadening their applications.

Appendix

A1 Cation/Hole percolation

1. Derivation of the relationship between diffusion coefficient and chronoabsorbtometry.

The apparent diffusion coefficients (D_{app}) for hole hopping due to percolation through neighbouring adsorbed dye molecules were measured at different surface coverages of dye molecules using chronoabsorptometry. To interpret the measurements, it is considered that the flux of holes diffusing across the surface of the TiO_2 electrode in one dimension where the TiO_2 substrate is located at $x = 0$ and the outer boundary of the film is located at $x = d$. The diffusion of the holes in one dimension is described by Fick's laws according to:

$$\frac{\partial p(x,t)}{\partial t} = D_{app}\frac{\partial^2 p(x,t)}{\partial x^2} \qquad \text{(Equation A1)}$$

where p is the concentration of holes at time t and position x. For chronoabsorptometry measurements the initial condition is $p(x,t = 0) = 0$. The final condition after a step change in potential at $t = 0$ is given when all connected dye molecules on the TiO_2 are oxidised by holes hopping from the boundary is given by $p(x=0,t=\infty) = p_{max}$. The boundary conditions for equation A1 for $t > 0$ are given by:

$$p(x = 0, t > 0) = p_{max} \qquad \text{(Equation A2)}$$

$$\frac{\partial p(x=d,t)}{\partial x} = 0 \qquad \text{(Equation A3)}$$

The solution to equation A1) is given by the infinite sum (see **Figure A-1**):

$$p(x,t) = p_{max} - \sum_{m=0}^{\infty}\frac{4p_{max}}{\pi(2m+1)}\sin\left[\frac{\pi x(2m+1)}{2d}\right]\exp\left[-\frac{\pi^2(2m+1)^2 D_{app}}{4d^2}t\right] \qquad \text{(Equation A4)}$$

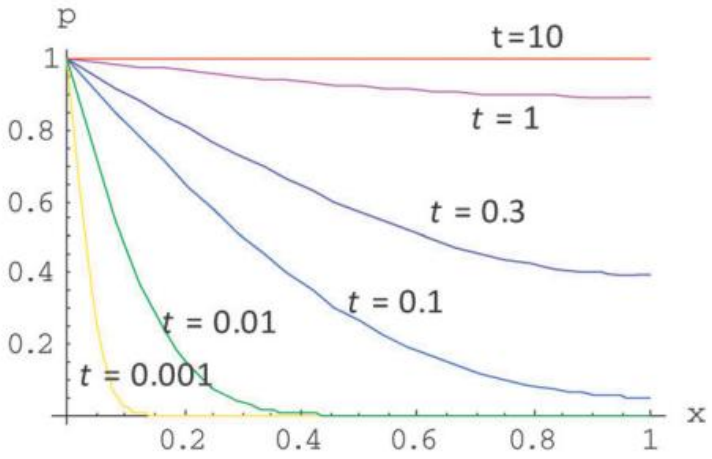

Figure A-1. Hole concentration profile (p) calculated using equation A4 at different times following a voltage step at $t = 0$ where $q = 1$, $p_{max} = 1$, $d = 1$, $D_{app} = 1$ and where $m = 0, 1, 2, \ldots, 100$ is used to approximate $m \rightarrow \infty$. Plots are shown at times $t = 0.001$ (yellow), 0.01 (green), 0.1 (light blue), 0.3 (dark blue), 1 (purple) and 10 (red).

The total concentration of holes in the film is given by integrating equation A4 with respect to x between 0 and d, so that the charge per unit area (Q) in the cell is given by:

$$Q = qp_{max}d - \sum_{m=0}^{\infty} \frac{8qp_{max}d}{(\pi+2m\pi)^2}(1 + \sin[m\pi])\exp\left[-\frac{\pi^2(2m+1)^2 D_{app}}{4d^2}t\right] \quad \text{(Equation A5)}$$

where q is the electronic charge. The dependence of Q on time is illustrated in **Figure A-2**.

The expression A5 can be approximated by an expression derived from the Cottrell equation at sufficiently short times. The solution to A1 with semi-infinite boundary conditions ($p(x=0, t>0) = p_{max}$, $p(x=\infty, t) = 0$) gives the Cottrell equation, describing the change in current density (j) at the substrate with time due the diffusion limited transfer of a species to or from the substrate following a potential step:

$$j = \frac{\partial Q}{\partial t} = zqp_{max}\sqrt{\frac{D_{app}}{\pi t}} \quad \text{(Equation A6)}$$

where $z = 1$ is the number of charges transferred for every hole reaching the substrate. Integrating equation A6 yields the amount of charge collected as a function of time:

$$Q = 2qp_{max}\sqrt{\frac{D_{app}t}{\pi}} \quad \text{(Equation A7)}$$

Figure A-2 shows charge as a function of time calculated using equations A5 and A7. It is apparent from figure A2 and equation A5 that when $t < d^2/(4\,D_{app})$ then Q derived

using the Cottrell equation (A7) is approximately equal to the exact solution (equation A5), and a linear relationship between Q and $t^{1/2}$ is expected.

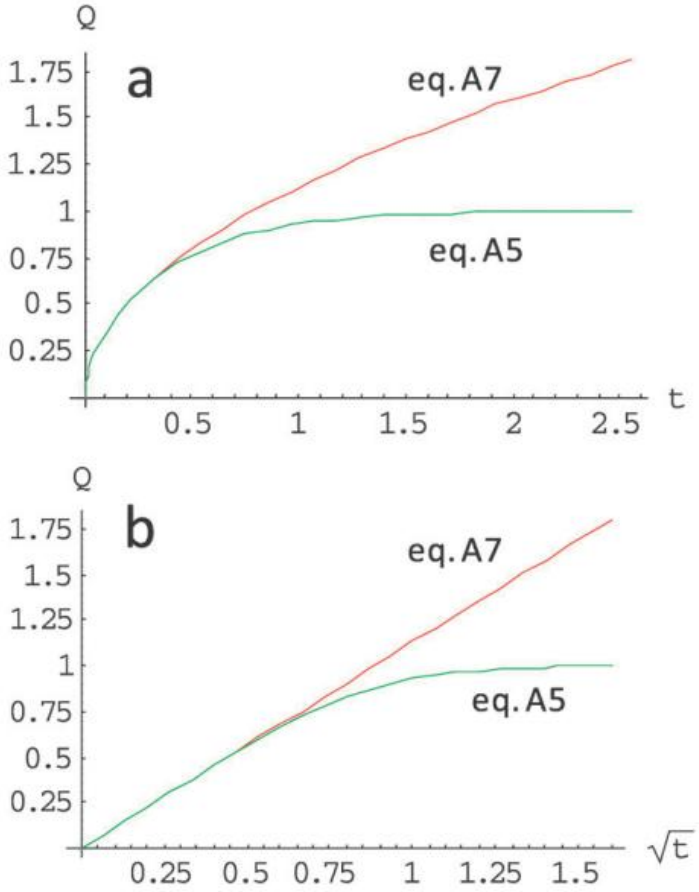

Figure A-2. The charge collected from oxidised dye molecules on TiO_2 at the substrate (Q) following a voltage step applied to the electrode at $t = 0$ using the exact solution to equation A1given by equation A5 (green) and the approximation given by the Cottrell equation A7 (red). **a.** Q plotted as a function of t. **b.** Q plotted as a function of $t^{1/2}$ (an Anson plot), both curves display a linear relationship for $t^{1/2} < 0.5$. The parameters used were the same as those in figure A1.

The maximum charge per unit area collected is related to p_{max} according to $Q_f = qdp_{max}$. In chronoabsorptometry, the change in absorbance (ΔOD) of the electroactive film is proportional to the charge passed (Q), thus equation A7 can be transformed into the corresponding equation 5-1 in the main text, to derive the apparent hole diffusion coefficient D_{app}:

$$\Delta OD = \frac{2\Delta OD_f}{d}\sqrt{\frac{D_{app}t}{\pi}} \qquad \text{(Equation A8)}$$

where ΔOD_f is the change in absorbance at long times corresponding to Q_f.

2. Potentiometric Spectroelectrochemistry of N621/ZrO_2 film

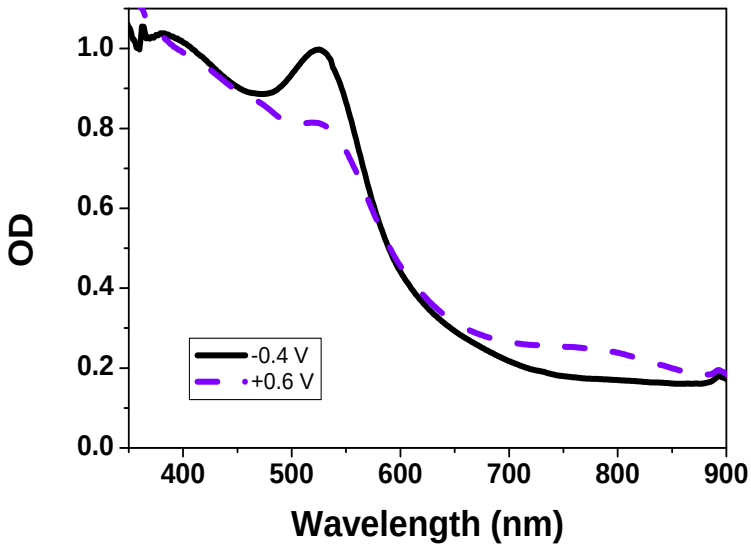

Figure A-3. UV/Vis spectra of N621 adsorbed on mesoporous ZrO_2 electrodes measured ca. 4 minutes after the application of the potentials indicated.The potential range is from -0.4 to 0.6 V vs Fc/Fc^+. The electrolyte is 0.1 M TBAP in acetonitrile.

3. Dye cation lifetime measurement

Figure A-4 shows the life time measurements for HW456 dye. The potential step is from -0.4 V to +0.45 V *vs* Fc/Fc^+.

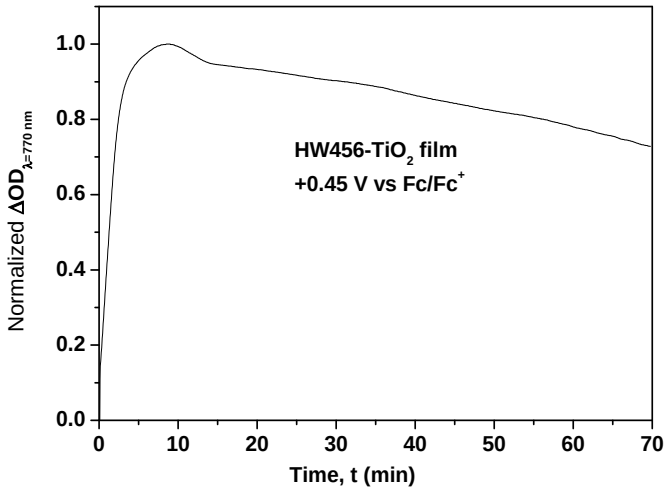

Figure A-4. Lifetime measurements for HW456 on nanocrystalline TiO_2 film in non-aqueous solution (0.1 M TBAP in acetonitrile).

A2 Iodine-metal oxide film interaction

1. SEM of 400 nm TiO_2 film

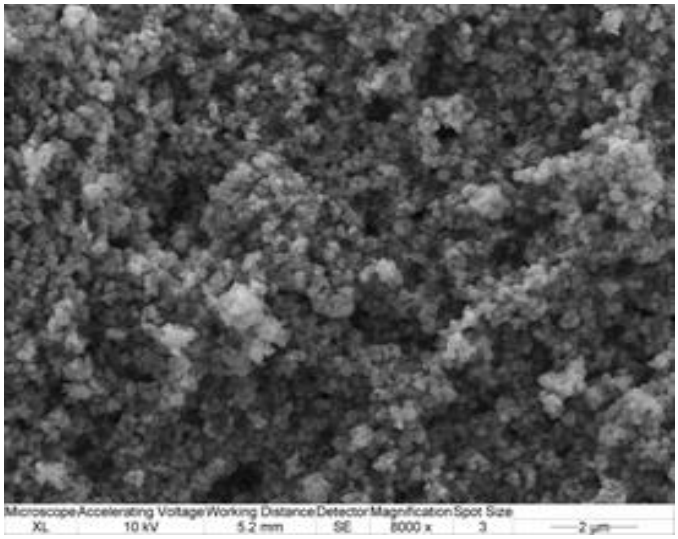

Figure A-5. SEM image of a 4 µm thick nanocrystalline TiO_2 film with particle size ~400 nm. The scale bar is 2 µm.

2. Reversible studies

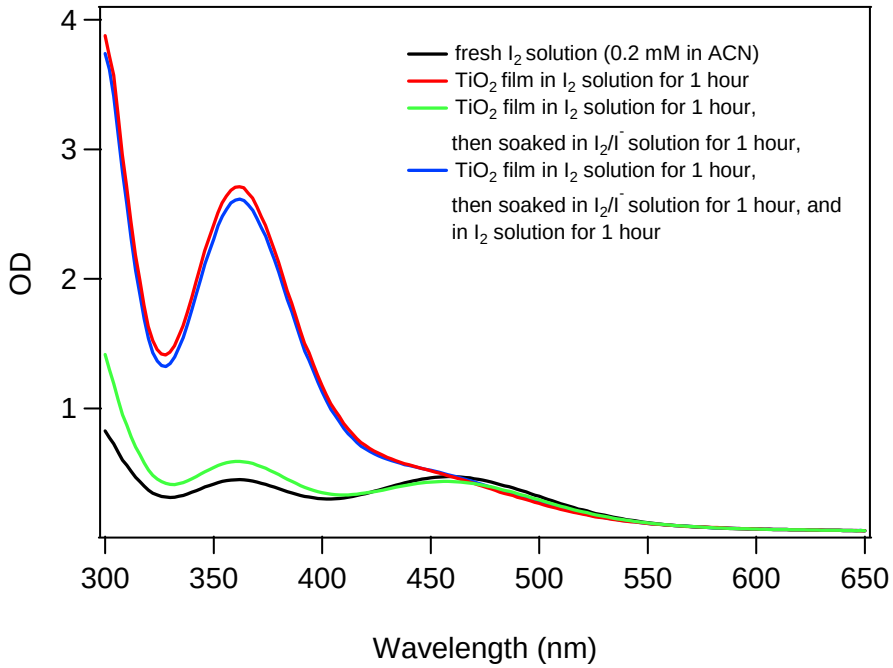

Figure A-6. Absorption spectra of iodine in ACN solution in the absence (black) and presence of the TiO_2 film before (**red**) and after reversed by the iodine and iodide mixture (5 mM iodine and 10 mM iodide) (**green**) and reimmersed in I_2 solution (**blue**) for one hour, respectively.

3. Al_2O_3 films and ZrO_2 films in 2 ml $2x10^{-4}$ M I_2 acetonitrile solutions

Nanocrystalline, mesoporous Al_2O_3 films and ZrO_2 films were immersed into 2 ml $2x10^{-4}$ M I_2 acetonitrile solutions, and then the solution absorption spectra were measured over a period of 45 min. Typical results are shown in **Figure A-**7.

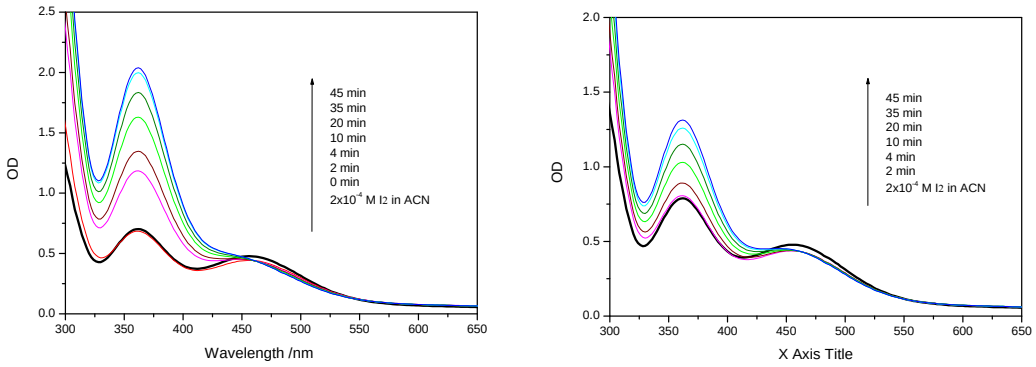

(a) (b)

Figure A-7. Time dependence of UV-Vis spectra of I_2 acetonitrile solutions in the absence and presence of nanocrystalline, mesoporous Al_2O_3 films (a) and ZrO_2 films (b).

4. TiO_2 film in 2 mM $Fc(III)PF_6$ in acetonitrile

Figure A-8 shows the absorption spectra change of ferrocium hexafluorophosphate in the presence of nanocrystalline TiO_2 films for different time. Compare to the UV-Vis spectrum of ferrocene, it can be seen clearly that there is no shift from Fe(III) to Fe(II) while the film immersed in the ferrocium in acetonitrile solvent.

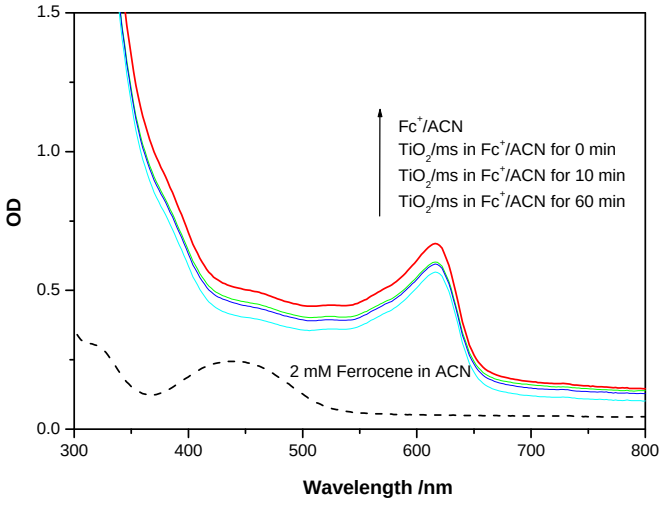

Figure A-8. UV-Vis spectra of 2 mM ferricenium hexafluorophosphate in acetonitrile (black, solid) and with the TiO_2 film up to 1 hour, and 2 mM ferrocene in acetonitrile (black, dash).

5. TiO_2 films in I_2 in DCM solution

In iodine in DCM solution, there is no triiodide band (362 nm) appeared while nanocrystalline, mesoporous TiO_2 film is immersed, as shown in **Figure A-9**.

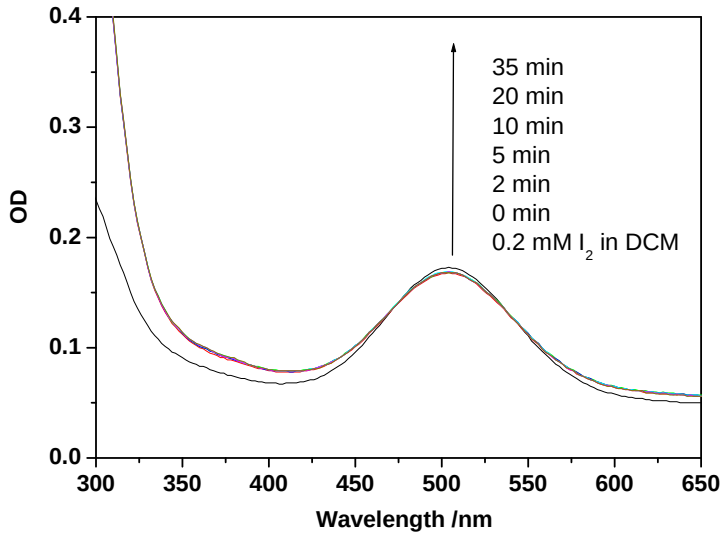

Figure A-9. Time dependence of UV-Vis spectra of I_2 DCM solutions in the absence (black) and presence of nanocrystalline mesoporous TiO_2 films.

6. TiO_2 films (400 nm) in I_2 ACN solution

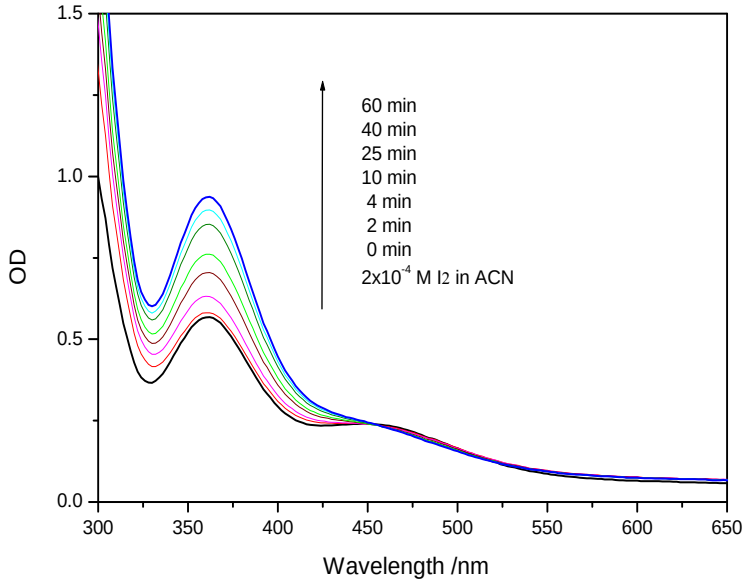

Figure A-10. Time dependence of UV-Vis spectra of iodine in acetonotrile solution in the absence and presence of the nanocrystalline mesoporous TiO_2 film (400 nm).

7. N719/TiO_2 films in I_2 acetonitrile solution

N719/TiO_2 films were immersed into 2 ml $2x10^{-4}$ M I_2 in acetonitrile solution, and the solution absorption spectra were measured for different time period. Typical results are shown in **Figure A-11**.

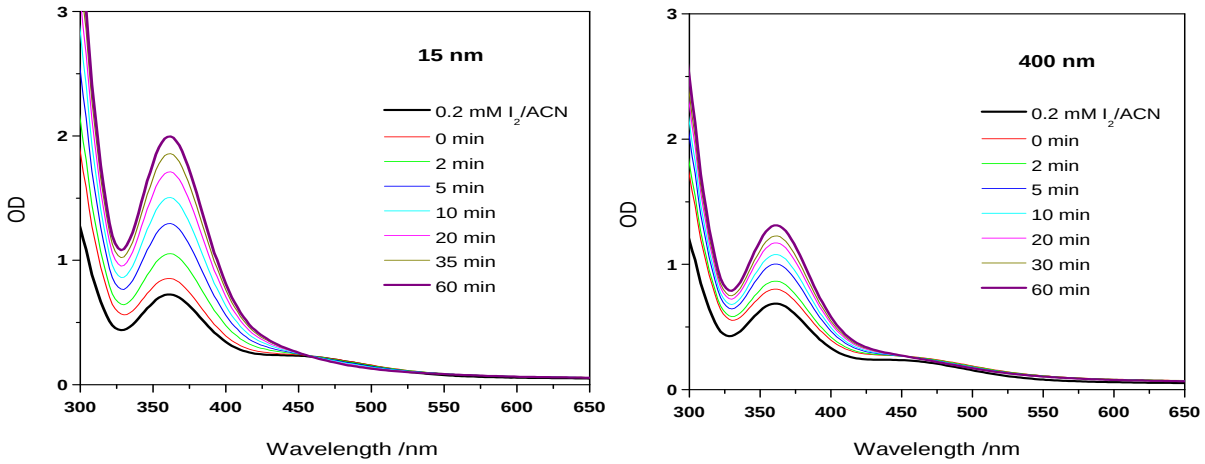

Figure A-11. Time dependence of UV-Vis spectra of iodine in acetonotrile solution in the absence and presence of the dye (N719) sensitised nanocrystalline, mesoporous TiO_2 films with different TiO_2 particle size.

A3 Iodine binding to ruthenium dyes

1. *I_2 titration to N719/TiO_2 films in dichloromethane*

To determine the dye-iodine binding constant in DCM, a series of I_2 solution (2, 5, 10, 15, 20, 30, 50, 70 and 100 µl) from 0.01 M I_2–DCM stock solution was added to 2 ml DCM solution in a 10 mm path length cuvette with a piece of N719/TiO_2 film, and the UV-Vis spectra of film in and out of beam were measured. Control experiments were performed by using blank TiO_2 film in DCM. The absorption spectra of dye sensitised films were obtained by subtracting the absorption of iodine in solution from the total absorption using equation 1, as shown in Figure A-12.

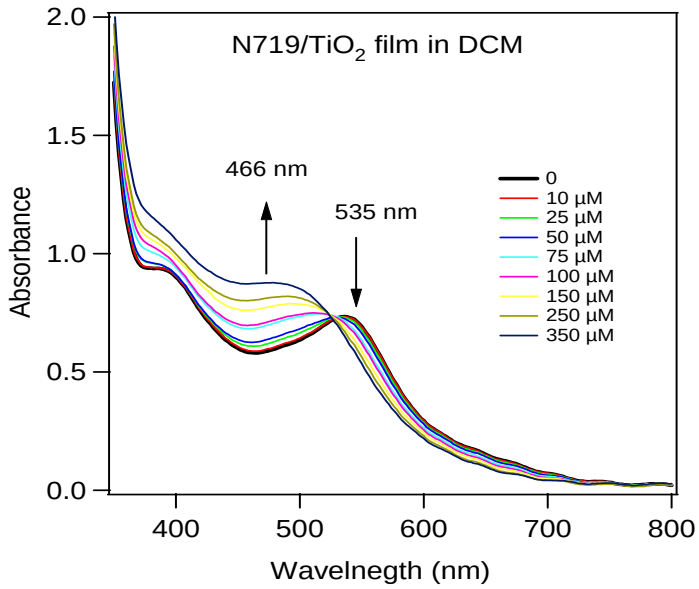

Figure A-12 The absorption spectra of the N719/TiO_2 film in DCM upon the iodine titration.

2. *I_2 titration toTiO_2 and Al_2O_3 films in acetonitrile and dichloromethane*

In the control experiments with TiO_2 and Al_2O_3 films in ACN and DCM (no dyes), there is no peak/change observed above 450 nm (**Figure A-13**) which means that the TiO_2 and Al_2O_3 films have no effect on dyes to I_2 binding in the range of 450~700 nm. However, there is something between 360 and 420 nm for TiO_2 film in ACN.

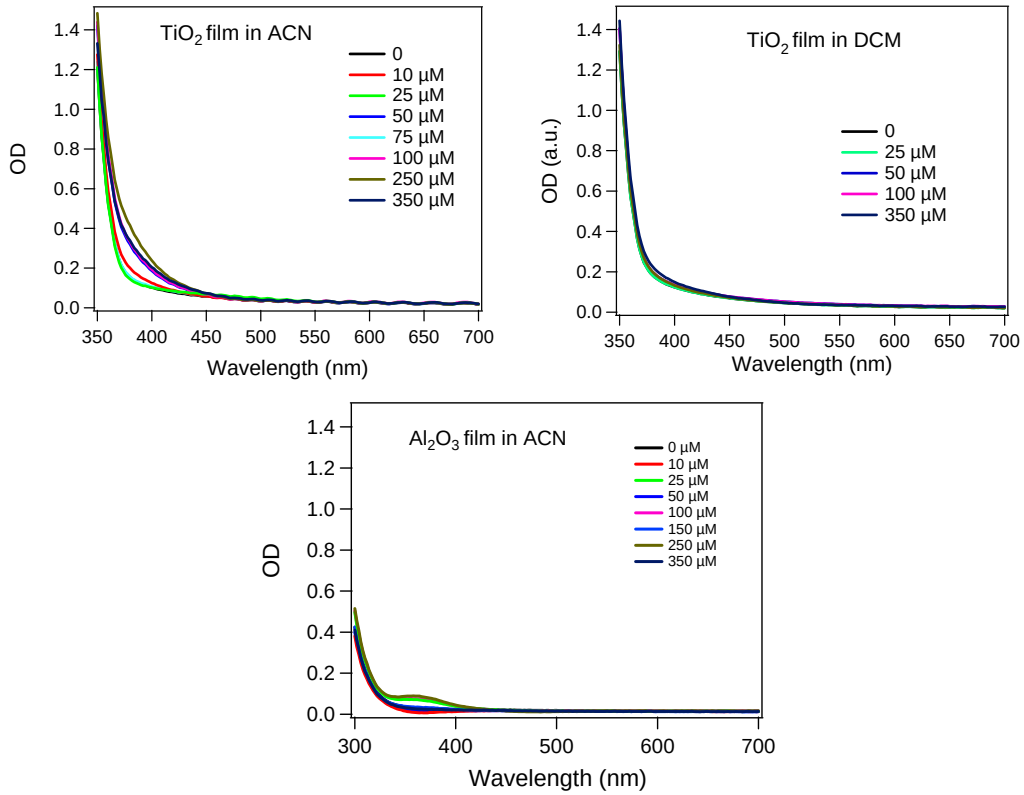

Figure A-13. The absorption spectra of the bare TiO_2 and Al_2O_3 films upon the iodine titration in ACN and DCM.

3. Compare the TiO_2 film to N719/TiO_2 film in the presence of iodine

Figure A-14 shows that the triiodide produced in solution in the presence of different films.

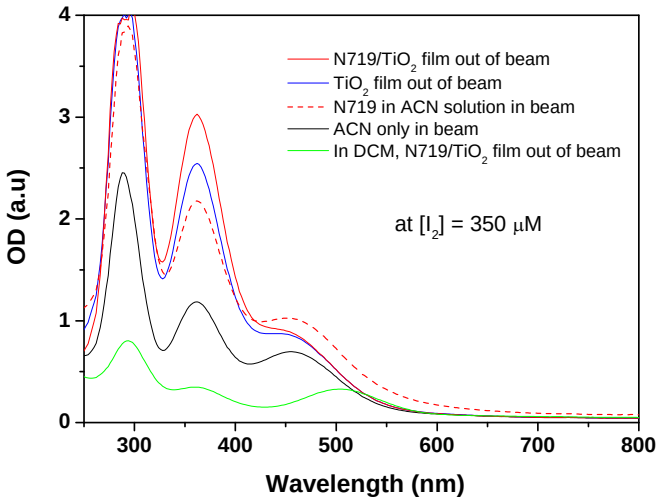

Figure A-14. The solution absorption spectra of TiO_2 film in ACN (blue), N719/TiO_2 films in ACN (red) and DCM (green), N719 in ACN solution (red dash) and control ACN (black) at 350 µM iodine concentration. Films were placed out of light beam in the cuvette.

At 700 nmol iodine, the amount of triiodide generated in acetonitrile is 43 nmol (=1.195/(5.6 x 10^4) x 100 x 2)), with TiO_2 film is 91 nmol (=2.55/(5.6 x 10^4) x 100 x 2) and with the N719/TiO_2 film is 108 nmol (=3.03/(5.6 x 10^4) x 100 x 2, 93 nmol N719 adsorbed on TiO_2 film). On the other hand, iodine titration in dye solution (40 nmol N719), subtracting the triiodide generated by N719 and ACN from only ACN background, there is 35 nmol (=0.978/(5.6 x 10^4) x 100 x 2) triiodide generated by dye N719.

4. DFT calculation

The LUMO of AR24 is of bipyridine π* character, while the LUMO +1 is a phenanthroline π* orbital, as shown in **Figure A-15.**

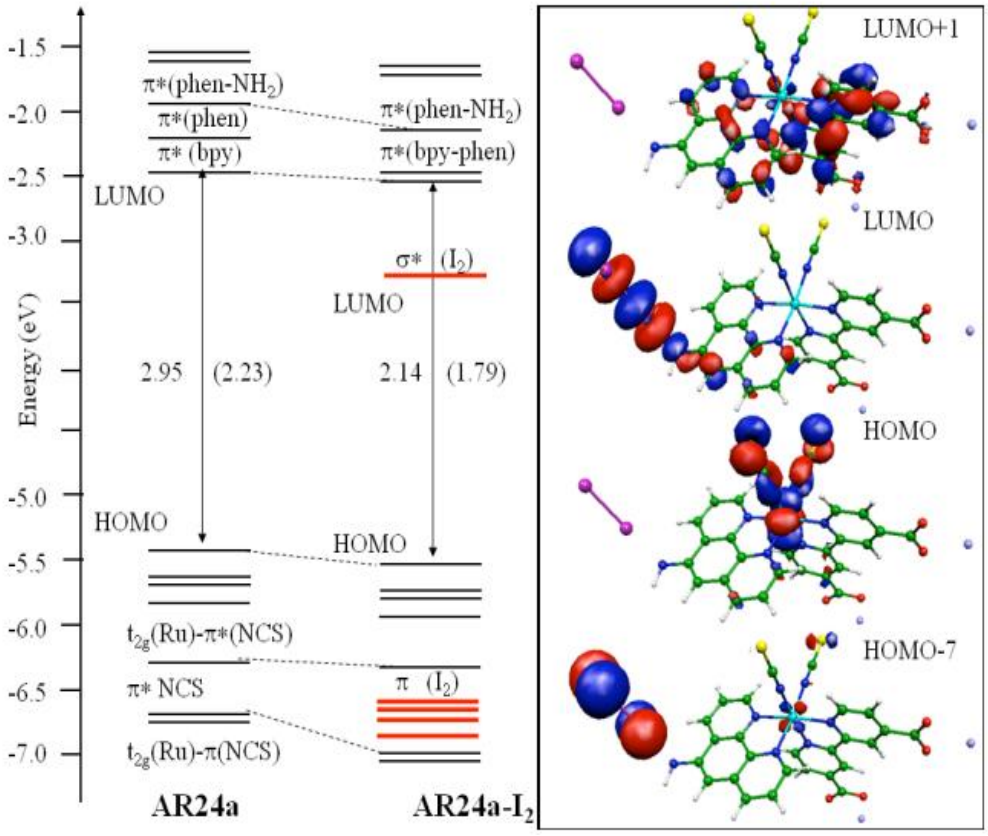

Figure A-15. Schematic representation of the energy levels for AR24 and AR24-I_2, along with isodensity plots of the selected molecular orbitals for the latter. Levels in red are those mainly based on the I_2 moiety. Also indicated are the HOMO-LUMO gaps and the lowest TDDFT excitation energies (values in parentheses). The calculation was carried out by Dr Filippo De Angelis (ISTM-CNR, Perugia, Italy).

5. Dye-iodine binding constant on TiO_2 films at CT band

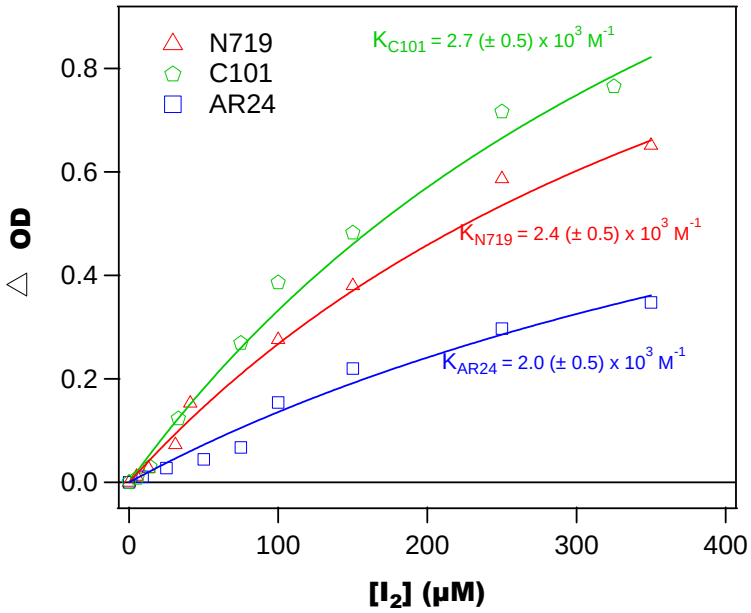

Figure A-16 The absorbance changes of the new complexes (=A-A_0) vs the iodine concentration for N719/TiO_2 film, C101/TiO_2 film and AR24/TiO_2 film.

6. N719 dye-iodine binding constant in DCM

The change of optical density at 466 nm (new complex) and 560 nm vs iodine concentration was plotted in **Figure A-17**, and the binding constant is estimated to be 2.8 (± 0.2) x 10^3 M^{-1} by fitting the scatter with equation 1-14.

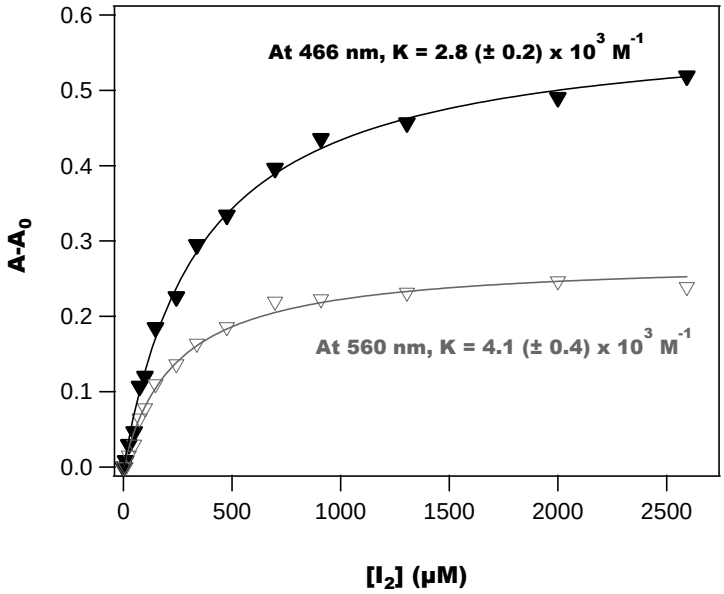

Figure A-17. The maximum absorbance change vs the iodine concentration for N719/TiO2 film in DCM solution.

7. N719 dye-iodine binding constant in solution

To determine the dye-iodine binding constant in solution, a series of I_2 solution from 0.01 M I_2 in ACN solution was added to 2 ml 20 µM N719 in ACN solution in a 10 mm path length cuvette and the UV-Vis spectrum of the mixture was measured. The experimental results are shown in **Figure A-18**.

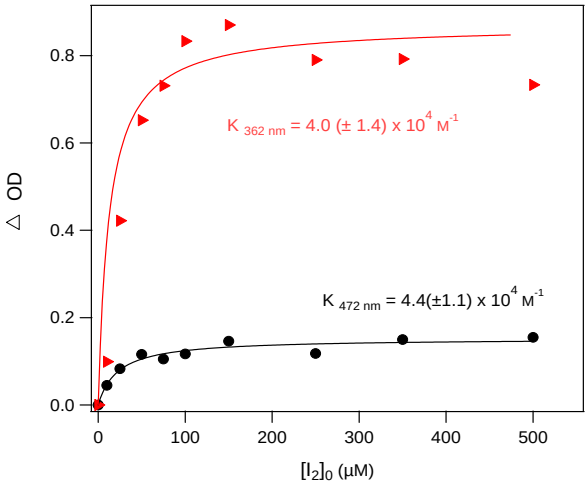

Figure A-18. The maximum absorbance change vs the iodine concentration for N719 solution. ACN background is subtracted.

8. FTIR of C101/TiO_2 in the presence and absence of iodine

Simliar to N719, the NCS peak appears at 2099 cm^{-1} and the hydrocarbon tail at 2856 cm^{-1} and 2926 cm^{-1} can be seen is the FTIR spectrum of C101/TiO_2 film, as shown in **Figure A-19**.

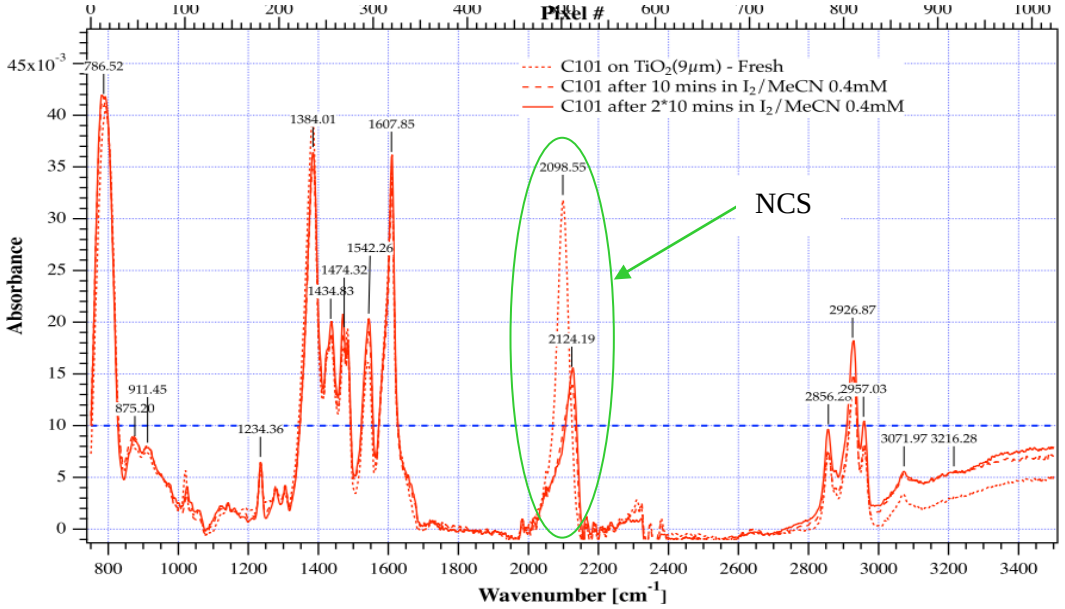

Figure A-19. FTIR of C101 on the TiO_2 surface in the presence and absence of iodine.

8. Charge recombination and transport/collection N719/TiO_2 and C101/TiO_2 cells

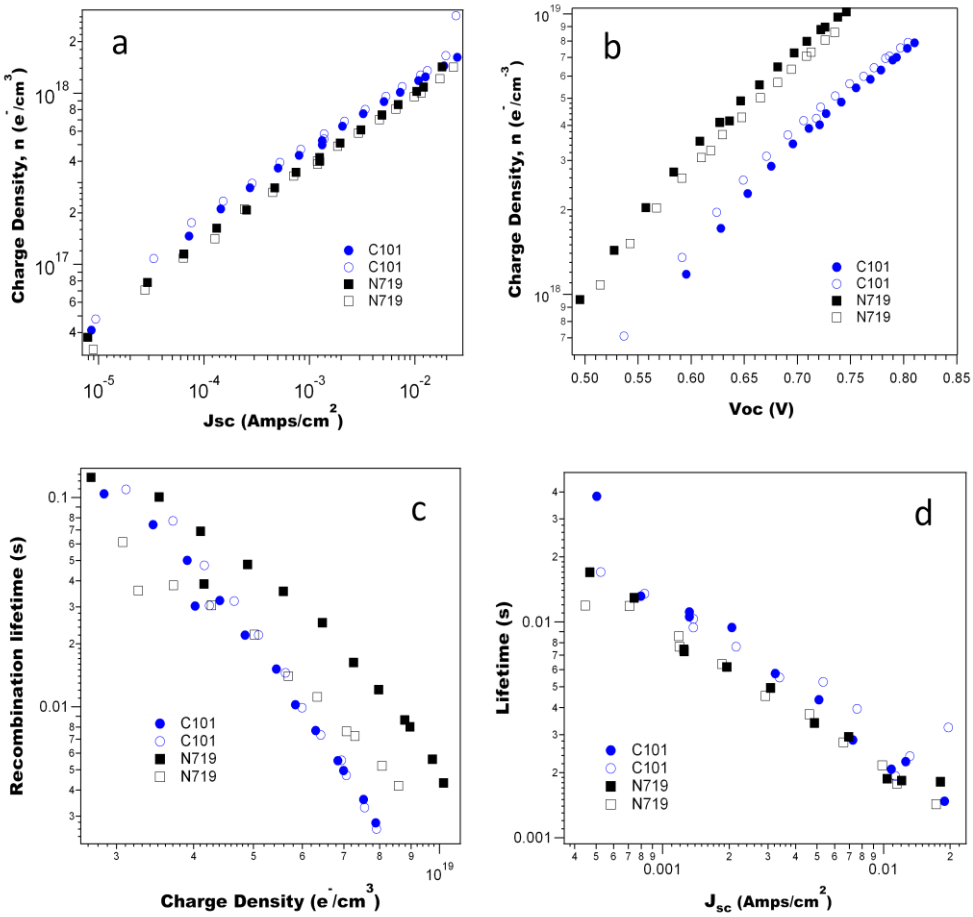

Figure A-20. Charge in the cell plotted as a function of (a) *Jsc* and (b)*Voc*, where the *Voc* was varied by changing the bias light intensity, for N719 (**black**) and C101(**blue**); (c) electron lifetime (τ_n) *vs* charge density measured at V_{oc} and (d) electron transport time (τ_j) measured at short circuit plotted against *Jsc*. E1 electrolyte is used.

9. Cell performance

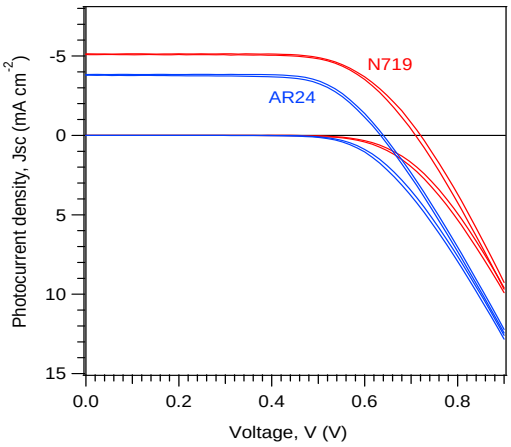

Figure A-21 I−V results for cells with AR24 (in blue) and N719 (in red) dyes. TiO_2 film thickness is 7 μm. Electrolyte as in text.

List of Publications

- O'Regan, B., Li, X., Ghaddar, T. *Energy Environ. Sci.*, 2012, 5, 7203-7215

  Dye adsorption, desorption, and distribution in mesoporous TiO2 films, and its effects on recombination losses in dye sensitized solar cells.

- Li, X.; Nazeeruddin, M. K.; Thelakkat, M.; Vilar, R.; Durrant. *Phys. Chem. Chem. Phys.*, 2011, **13**, 1575-1584

  Spectroelectrochemical Studies of Hole Percolation on Functionalised Nanocrystalline TiO_2 Films: A Comparison of Two Different Ruthenium Complexes.

- Li, X., Barnes, P., Ghaddar, T., Humphry-Baker, R., Durrant, JR, Vilar, R. and O'Regan,B. *Manuscript in Preparation.*

  Iodine binding to ruthenium complexes adsorbed to nanocrystalline mesoporous TiO_2 films.

- Gimeno, N, Li, X, Durrant, JR, Vilar, R, *Chem-Eur J*, 2008, **14**, 3006-3012

  Cyanide sensing with organic dyes: Studies in solution and on nanostructured Al_2O_3 surfaces.

- Li, X,, Perez-Hernandez, J, Haque, SA, Durrant, JR. *J Mater. Chem.*, 2007, **17**: 2028-2032

  Functionalized titania nanoparticles for mercury scavenging.

- Barnes, P., Liu, L., Li, X., Anderson, A., Kisserwan, H., Ghaddar, T., Durrant, J. and O'Regan, B. *Nano Lett.*, 2009, **9** (10): 3532-3538

  Re-evaluation of Recombination Losses in Dye-Sensitized Cells: The Failure of Dynamic Relaxation Methods to Correctly Predict Diffusion Length in Nanoporous Photoelectrodes.

- Durrant, J.R., Palomares, E. and Li, X. WO/2008/025977.

  Mercury Scavenging.

Reference List

1. *http://www. lenntech. com/processes/heavy/heavy-metals/heavy-metals*

2. O'Regan, B.; Grätzel, M. A low-cost, high-efficiency solar cell based on dye-sensitized colloidal TiO_2 films. *Nature* **1991,** *14* (353), 737-740.

3. Grätzel, M. Photoeletrochemical cell. *Nature* **2001,** *14* (414), 338-344.

4. Haque, S. A.; Koops, S.; Tokmoldin, N.; Durrant, J. R.; Huang, J.; Bradley, D. D. C.; Palomares, E. A Multilayered Polymer Light-Emitting Diode Using a Nanocrystalline Metal-Oxide Film as a Charge-Injection Electrode. *Adv. Mater.* **2007,** *19*, 683-687.

5. Palomares, E.; Vilar, R.; Durrant, J. R. Heterogeneous colorimetric sensor for mercuric salts. *Chemical Communications* **2004,** *14* (4), 362-363.

6. Astuti, Y.; Topoglidis, E.; Gilardi, G.; Durrant, J. R. Cyclic voltammetry and voltabsorptometry studies of redox proteins immobilised on nanocrystalline tin dioxide electrodes. *Bioelectrochemistry* **2004,** *63* *14* (1-2), 55-59.

7. FUJISHIMA, A.; Honda, K. Electrochemical photolysis of water at a semiconductor electrode. *Nature* **1972,** *238* (5358), 37.

8. Li, L.; Duan, L.; Xu, Y.; Gorlov, M.; Hagfeldt, A.; Sun, L. A photoelectrochemical device for visible light driven water splitting by a molecular ruthenium catalyst assembled on dye-sensitized nanostructured TiO2. *Chemical Communications* **2010,** *46* (39), 7307-7309.

9. Li, X.; Green, A. N. M.; Haque, S. A.; Mills, A.; Durrant, J. R. Light-driven oxygen scavenging by titania/polymer nanocomposite films. *Journal of Photochemistry and Photobiology A: Chemistry* **2004,** *162* (2-3), 253-259.

10. Jolivet, J. P.; Henry, M.; Livage, J. *Metal Oxide Chemistry and Synthesis from solution to solid state;* John Wiley & Sons, Ltd: 2000.

11. Palomares, E.; Clifford, J. N.; Haque, S. A.; Lutz, T.; Durrant, J. R. Control of charge recombination dynamics in dye sensitized solar cells by the use of conformally deposited metal oxide blocking layers. *Journal of the American Chemical Society* **2003,** *125* (2), 475-482.

12. Bradley, R. Recent Developments in the Physical Adsorption of Toxic Organic Vapours by Activated Carbons. *Adsorption science & technology* **2011,** *29* (1), 1-28.

13. Gratzel, M. Sol-Gel Processed TiO2 Films for Photovoltaic Applications. *Journal of sol-gel science and technology* **2001,** *22* (1), 7-13.

14. Hagfeldt, A.; Gratzel, M. Light-Induced Redox Reactions in Nanocrystalline Systems. *Chem. Rev.* **1995,** *95*, 49-68.

15. Nazeeruddin, Md. K.; Humphry-Baker, R.; Liska, P.; Grätzel, M. Investigation of Sensitizer Adsorption and the Influence of Protons on Current and Voltage of a Dye-Sensitized Nanocrystalline TiO2 Solar Cell. *J. Phys. Chem. B* **2003,** *107* (14), 8981-8987.

16. Papageorgiou, N.; Gratzel, M.; Enger, O.; Bonifazi, D.; Diederich, F. Lateral electron transport inside a monolayer of derivatized fullerenes anchored on nanocrystalline metal oxide films. *Journal of Physical Chemistry B* **2002,** *106* (15), 3813-3822.

17. Bonhote, P.; Gogniat, E.; Tingry, S.; Barbe, C.; Vlachopoulos, N.; Lenzmann, F.; Comte, P.; Gratzel, M. Efficient lateral electron transport inside a monolayer of aromatic amines anchored on nanocrystalline metal oxide films. *Journal of Physical Chemistry B* **1998,** *102* (9), 1498-1507.

18. Palomares, E.; Vilar, R.; Green, A.; Durrant, J. R. Alizarin Complexone on nanocrystalline TiO2: a heterogeneous approach to anion sensing. *Adv. Funct. Mater.* **2004,** *14* (10), 111-115.

19. Galoppini, E. Linkers for anchoring sensitizers to semiconductor nanoparticles. *Coordination Chemistry Reviews* **2004,** *248* (13-14), 1283-1297.

20. Ogawa, H.; Chihara, T.; Taya, K. Selective monomethyl esterification of dicarboxylic acids by use of monocarboxylate chemisorption on alumina. *Journal of the American Chemical Society* **1985,** *107* (5), 1365-1369.

21. Allara, D.; Nuzzo, R. Spontaneously Organized Molecular Assemblies. 1.Formation, Dynamics, and Physical Properties of *n* -Alkanoic Acids Adsorbed from Solution on an Oxidized Aluminum Surface. *Langmuir* **1985,** *14* (1), 45-52.

22. Hagfeldt, A.; Boschloo, G.; Sun, L.; Kloo, L.; Pettersson, H. Dye-Sensitized Solar Cells. *Chemical reviews* **2010,** *110* (11), 6595-6663.

23. Durrant, J. R.; Haque, S. A.; Palomares, E. Photochemical energy conversion: from molecular dyads to solar cells. *Chemical Communications* **2006,** (31).

24. Haque, S. A.; Palomares, E.; Upadhyaya, H. M.; Otley, L.; Potter, R. J.; Holmes, A. B.; Durrant, J. R. Flexible dye sensitised nanocrystalline semiconductor solar cells. *Chemical Communications* **2003,** (24), 3008-3009.

25. Nazeeruddin, M. K.; De Angelis, F.; Fantacci, S.; Selloni, A.; Viscardi, G.; Liska, P.; Ito, S.; Takeru, B.; Gratzel, M. Combined Experimental and DFT-TDDFT Computational Study of Photoelectrochemical Cell Ruthenium Sensitizers. *Journal of the American Chemical Society* **2005,** *127* (48), 16835-16847.

26. Gao, F. F.; Wang, Y.; Shi, D.; Zhang, J.; Wang, M. K.; Jing, X. Y.; Humphry-Baker, R.; Wang, P.; Zakeeruddin, S. M.; Gra¦êtzel, M. Enhance the Optical Absorptivity of Nanocrystalline TiO2 Film with High Molar Extinction Coefficient Ruthenium Sensitizers for High Performance Dye-Sensitized Solar Cells. *Journal of the American Chemical Society* **2008,** *130* (32), 10720-10728.

27. Matar, F.; Ghaddar, T. H.; Walley, K.; Dos Santos, T.; Durrant, J. R.; O'Regan, B. A new ruthenium polypyridyl dye, TG6, whose performance in dye-sensitized solar

cells is surprisingly close to that of N719, the dye to beat for 17 years. *J. Mater. Chem.* **2008,** *18*, 4246-4253.

28. Santos, T. D.; Morandeira, A.; Koops, S.; Mozer, A. J.; Tsekouras, G.; Dong, Y.; Wagner, P.; Wallace, G.; Earles, J. C.; Gordon, K. C.; Officer, D.; Durrant, J. R. Injection Limitations in a Series of Porphyrin Dye-Sensitized Solar Cells. *The Journal of Physical Chemistry C* **2010,** *114* (7), 3276-3279.

29. O'Regan, B.; Lopez-Duarte, I.; Martinez-Diaz, M. V.; Forneli, A.; Albero, J.; Morandeira, A.; Palomares, E.; Torres, T.; Durrant, J. R. Catalysis of Recombination and Its Limitation on Open Circuit Voltage for Dye Sensitized Photovoltaic Cells Using Phthalocyanine Dyes. *J. Am. Chem. Soc.* **2008,** *130* (10), 2906-2907.

30. Hara, K.; Sato, T.; Katoh, R.; Furube, A.; Yoshihara, T.; Murai, M.; Kurashige, M.; Ito, S.; Shinpo, A.; Suga, S.; Arakawa, H. Novel conjugated organic dyes for efficient dye-sensitized solar cells. *Advanced Functional Materials* **2005,** *15* (2), 246-252.

31. Chen, R. K.; Yang, X. C.; Tian, H. N.; Sun, L. C. Tetrahydroquinoline dyes with different spacers for organic dye-sensitized solar cells. *Journal of Photochemistry and Photobiology A-Chemistry* **2007,** *189* (2-3), 295-300.

32. Kim, J.; Kim, Y.; Kim, Y. Indoline dyes with various acceptors for dye-sensitized solar cells. *Current Applied Physics* **2011,** *11* (1, Supplement 1), S117-S121.

33. Koops, S.; O'Regan, B.; Barnes P.; Durrant, J. R. Parameters Influencing the Efficiency of Electron Injection in Dye-Sensitized Solar Cells. *Journal of the American Chemical Society* **2009,** *131* (13), 4808-4818.

34. Law, C. H.; Pathirana, S. C.; Li, X.; Anderson, A. Y.; Barnes, P.; Listorti, A.; Ghaddar, T. H.; O'Regan, B. C. Water-Based Electrolytes for Dye-Sensitized Solar Cells. *Adv. Mater.* **2010,** *22* (40), 4505-4509.

35. Clifford, J. N.; Martinez-Ferrero, E.; Viterisi, A.; Palomares, E. Sensitizer molecular structure-device efficiency relationship in dye sensitized solar cells. *Chem. Soc. Rev.* **2011,** *40* (3), 1635-1646.

36. Wolden, C. A.; Kurtin, J.; Baxter, B.; Repins, I.; Shaheen, S. E.; Torvik, J. T.; Rockett, A. A.; Fthenakis, V.; Aydil, E. S. Photovoltaic manufacturing: Present status, future prospects, and research needs. *Journal of vacuum science & technology A* **2011,** *29* (3), 1-16.

37. O'Regan, B. C.; Durrant, J. R. Kinetic and Energetic Paradigms for Dye-Sensitized Solar Cells: Moving from the Ideal to the Real. *Accounts of chemical research* **2009,** *42* (11), 1799-1808.

38. Nelson, I. V.; Iwamoto, R. T. Voltammetric evaluation of the stability of trichloride, tribromide, and triiodide ions in nitromethane, acetone, and acetonitrile. *Journal of Electroanalytical Chemistry* **1964,** *7* (3), 218-221.

39. Grgur, B. N.; Gvozdenovic, M. M.; Stevanovic, J. S.; Jugovic, B. Z.; Trisovic, L. Electrochemical oxidation of iodide in aqueous solution. *Chemical Engineering Journal* **2006,** *124* (1-3), 47-54.

40. Morandeira, A.; Lopez-Duarte, I.; O'Regan, B.; Martinez-Diaz, M. V.; Forneli, A.; Palomares, E.; Torres, T.; Durrant, J. R. Ru(II)-phthalocyanine sensitized solar cells: the influence of co-adsorbents upon interfacial electron transfer kinetics. *Journal of Materials Chemistry* **2009,** *19* (28), 5016-5026.

41. McCall, K. L.; Jennings, J. R.; Wang, H.; Morandeira, A.; Peter, L. M.; Durrant, J. R.; Yellowlees, L. J.; Woollins, J. D.; Robertson, N. Novel ruthenium bipyridyl dyes with S-donor ligands and their application in dye-sensitized solar cells. *Journal of Photochemistry and Photobiology A: Chemistry* **2009,** *202* (2-3), 196-204.

42. Yella, A.; Lee, H.; Tsao, H.; Yi, C.; Chandiran, A.; Nazeeruddin, Md.; Diau, E.; Yeh, C.; Zakeeruddin, Sh.; Gratzel, M. Porphyrin-Sensitized Solar Cells with Cobalt (II/III) Based Redox Electrolyte Exceed 12 Percent Efficiency. *Science* **2011,** *334* (6056), 629-634.

43. Hore, S.; Vetter, C.; Kern, R.; Smit, H.; Hinsch, A. Influence of scattering layers on efficiency of dye-sensitized solar cells. *Solar Energy Materials & Solar Cells* **2006,** *90*, 1176-1188.

44. Ito, S.; Liska, P.; Comte, P.; Charvet, R.; Pechy, P.; Bach, U.; Schmidt-Mende, L.; Zakeeruddin, S. M.; Kay, A.; Nazeeruddin, M. K.; Gratzel, M. Control of dark current in photoelectrochemical (TiO2/I--I3-) and dye-sensitized solar cells. *Chemical Communications* **2005,** (34), 4351-4353.

45. Palomares, E.; Clifford, J. N.; Haque, S. A.; Lutz, T.; Durrant, J. R. Control of charge recombination dynamics in dye sensitized solar cells by the use of conformally deposited metal oxide blocking layers. *Journal of the American Chemical Society* **2003,** *125* (2), 475-482.

46. Cattrall, R. W. *Chemical Sensors;* Oxford Chemistry Primers: 1997.

47. Eggins, B. R. *Chemical Sensors and Biosensors ;* John Wiley & Sons, LTD: 2002.

48. Zhang, S.; Cardona, C.; Echegoyen, L. Ion recognition properties of self-assembled monolayers (SAMs). *Chemical Communications* **2006,** (43), 4461.

49. Lee, S. J.; Lee, J. E.; Seo, J.; Jeong, I. Y.; Lee, S. S.; Jung, J. H. Optical sensor based on nanomaterial for the selective detection of toxic metal ions. *Advanced Functional Materials* **2007,** *17* (17), 3441-3446.

50. Kim, E.; Seo, S.; Seo, M.; Jung, J. Functionalized monolayers on mesoporous silica and on titania nanoparticles for mercuric sensing. *Analyst* **2010,** *135* (1), 149-156.

51. Goldenberg, L. M.; Bryce, M. R.; Petty, M. C. Chemosensor devices: voltammetric molecular recognition at solid interfaces. *Journal of Materials Chemistry* **1999,** *9* (9), 1957.

52. Mohr, G. J.; Murkovic, I.; Lehmann, F.; Haider, C.; Wolfbeis, O. S. Application of potential-sensitive fluorescent dyes in anion- and cation-sensitive polymer membranes. *Sensors and Actuators B-Chemical* **1997,** *39* (1-3), 239-245.

53. Poland, K.; Topoglidis, E.; Durrant, J. R.; Palomares, E. Optical sensing of cyanide using hybrid biomolecular films. *Inorganic Chemistry Communications* **2006,** *9* (12), 1239-1242.

54. Beer, P. D.; Gale, P. A.; Smith, D. K. *Supramolecular Chemistry;* Oxford University Press: 1999.

55. Beer, P. D.; Gale, P. A. Anion Recognition and Sensing: The State of the Art and Future Perspectives. *Angew. Chem. , Int. Ed.* **2001,** *40* (10), 486-516.

56. Smith, D. W. Ionic hydration enthalpies. *J. Chem. Educ.* **1977,** *54* (9), 540.

57. Vilar, R. Anion Recognition and Templation in Coordination Chemistry. *Eur. J. Inorg. Chem.* **2008,** 357-367.

58. Suksai, C.; Tuntulani, T. Chromogenic Anion Sensors. *Top. Curr. Chem.* **2005,** *255*, 163-198.

59. Valeur, B.; Leray, I. Design principles of fluorescent molecular sensors for cation recognition. *Coordination Chemistry Reviews* **2000,** *205* (1), 3-40.

60. Martinez-Manez, R.; Sancenon, F. Fluorogenic and Chromogenic Chemosensors and Reagents for Anions. *Chemical reviews* **2003,** *103* (11), 4419-4476.

61. Lee, S.; Lee, J. E.; Seo, J.; Jeong, I. Y.; Lee, S.; Jung, J. Optical sensor based on nanomaterial for the selective detection of toxic metal ions. *Advanced Functional Materials* **2007,** *17* (17), 3441-3446.

62. Evans, L. S.; Gale, P. A.; Light, M.; Quesada, R. Anion binding vs. deprotonation in colorimetric pyrrolylamidothiourea based anion sensors. *Chem. Commun.* **2008,** (10), 965-967.

63. Zakeeruddin, S. M.; Nazeeruddin, M. K.; Pechy, P.; Rotzinger, F. P.; Humphry-Baker, R.; Kalyanasundaram, K.; Gr+ñtzel, M.; Shklover, V.; Haibach, T. Molecular Engineering of Photosensitizers for Nanocrystalline Solar Cells: Synthesis and Characterization of Ru Dyes Based on Phosphonated Terpyridines. *Inorganic chemistry* **1997,** *36* (25), 5937-5946.

64. Kim, Y. J.; Johnson, R. C.; Hupp, J. T. Gold nanoparticle-based sensing of "spectroscopically silent" heavy metal ions. *Nano Letters* **2001,** *1* (4), 165-167.

65. Wu, J.; Liu, W.; Ge, J.; Zhang, H.; Wang, P. New sensing mechanisms for design of fluorescent chemosensors emerging in recent years. *Chem. Soc. Rev.* **2011,** *40* (7), 3483-3495.

66. Xue, H.; Tang, X.; Wu, L.; Zhang, L.; Tung, C. Highly Selective Colorimetric and Electrochemical Pb2+ Detection Based on TTF-pi-Pyridine Derivatives. *J. Org. Chem.* **2005,** *70* (24), 9727-9734.

67. Rose, N. J.; Drago, R. S. Molecular Addition Compounds of Iodine. I. An Absolute Method for the Spectroscopic Determination of Equilibrium Constants. *Journal of the American Chemical Society* **1959,** *81* (23), 6138-6141.

68. Benesi.H.A.; Hildebrand, J. H. A Spectrophotometric Investigation of the Interaction of Iodine with Aromatic Hydrocarbons. *Journal of the American Chemical Society* **1949,** *71* (8), 2703-2707.

69. Atkins, P.; Paula, J. d. *Physical Chemistry;* 7th ed.; Oxford University Press, Oxford, U. K.: 2002.

70. Davis, F.; Collyer, S.; Higson, S. The Construction and Operation of Anion Sensors: Current Status and Future Perspectives. *Top Curr Chem* **2005,** *255* (10), 97-124.

71. Gunnlaugsson, T.; Kruger, P. E.; Jensen, P.; Tierney, J.; Ali, H.; Hussey, G. Colorimetric "Naked Eye" Sensing of Anions in Aqueous Solution. *J. Org. Chem.* **2005,** *70* (10), 10875-10878.

72. Fergus, J. W. Materials for high temperature electrochemical NOx gas sensors. *Sensors and Actuators B: Chemical* **2007,** *121* (2), 652-663.

73. Stetter, J.; Penrose, W. R.; Maclay, G. J.; Buttner, W. J.; Findlay, M. W.; Cao, Z.; Luskus, L. J.; Mulik, J. D. The electrochemical sensor: one solution for pollution. *ACS symposium series* **1992,** *508* (Pollut), 103.

74. Zhao, Q. A Highly Selective and Multisignaling Optical-Electrochemical Sensor for Hg2+ Based on a Phosphorescent Iridium(III) Complex. *Organometallics* **2007,** *26* (8), 2077.

75. Wassana, Y. Nanostructured electrochemical sensors based on functionalized nanoporous silica for voltammetric analysis of lead, mercury, and copper. *Journal of Nanoscience and Nanotechnology* **2005,** *5* (9), 1537.

76. Kachoosangi, R.; Banks, C.; Ji, X.; Compton, R. Electroanalytical Determination of Cadmium(II) and Lead(II) Using an *in-situ* Bismuth Film Modified Edge Plane Pyrolytic Graphite Electrode. *Analytical Sciences* **2007,** *23*, 283-289.

77. Topoglidis, E.; Astuti, Y.; Duriaux, F.; Gratzel, M.; Durrant, J. R. Direct Electrochemistry and Nitric Oxide Interaction of Heme Proteins Adsorbed on Nanocrystalline Tin Oxide Electrodes. *Langmuir* **2003,** *19* (17), 6894-6900.

78. Solanki, P.; Patel, M.; Kaushik, A.; Pandey, M.; Kotnala, R.; Malhotra, B. Sol-Gel Derived Nanostructured Metal Oxide Platform for Bacterial Detection. *Electroanalysis* **2011,** *23* (11), 2699-2708.

79. Kumar, S.; Lo, P.; Chen, S. Electrochemical synthesis and characterization of TiO2 nanoparticles and their use as a platform for flavin adenine dinucleotide immobilization and efficient electrocatalysis. *Nanotechnology* **2008,** *19* (25), 255501-255507.

80. Rui, Q.; Komori, K.; Tian, Y.; Liu, H.; Luo, Y.; Sakai, Y. Electrochemical biosensor for the detection of H(2)O(2) from living cancer cells based on ZnO nanosheets. *Analytica Chimica Acta* **2010,** *670* (1-2), 57-62.

81. Marritt, S. J.; Kemp, G. L.; Li, X.; Durrant, J. R.; Cheesman, M. R.; Butt, J. N. Spectroelectrochemical Characterization of a Pentaheme Cytochrome in Solution and

as Electrocatalytically Active Films on Nanocrystalline Metal-Oxide Electrodes. *J. Am. Chem. Soc.* **2008,** *130*, 8588-8589.

82. Kemp, G. L.; Marritt, S. J.; Li, X.; Durrant, J. R.; Cheesman, M. R.; Butt, J. N. Opportunities for mesoporous nanocrystalline SnO2 electrodes in kinetic and catalytic analyses of redox proteins. *Biochem. Soc. Trans.* **2009,** *37*, 368-372.

83. Topoglidis, E.; Lutz, T.; Willis, R. L.; Barnett, C. J.; Cass, A. E. G.; Durrant, J. R. Protein adsorption on nanoporous TiO2 films: a novel approach to studying photoinduced protein/electrode transfer reactions. *Faraday Discussions* **2000,** *14* (116), 35-46.

84. Topoglidis, E. Biosensors based on nanoporous TiO_2 films. Imperial College London, 2001.

85. Li, X.; Nazeeruddin, M. K.; Thelakkat, M.; Barnes, P. R. F.; Vilar, R.; Durrant, J. R. Spectroelectrochemical studies of hole percolation on functionalised nanocrystalline TiO2 films: a comparison of two different ruthenium complexes. *Phys. Chem. Chem. Phys.* **2011,** *13* (4), 1575-1584.

86. Wang, Q.; Evans, N.; Zakeeruddin, S. M.; Exnar, I.; Gratzel, M. Molecular Wiring of Insulators: Charging and Discharging Electrode Materials for High-Energy Lithium-Ion Batteries by Molecular Charge Transport Layers. *Journal of the American Chemical Society* **2007,** *129* (11), 3163-3167.

87. Drury, C.; Mutsaers, C.; Hart, C.; Matters, M.; Leeuw, D. Low-cost all-polymer integrated circuits. *Applied physics letters* **1998,** *73* (1), 108.

88. Coronado, E.; Galan-Mascaros, J. R.; Marti-Gastaldo, C.; Palomares, E.; Durrant, J. R.; Vilar, R.; Gratzel, M.; Nazeeruddin, M. K. Reversible colorimetric probes for mercury sensing. *Journal of the American Chemical Society* **2005,** *127* (35), 12351-12356.

89. Barbe, C. J.; Arendse, F.; Comte, P.; Jirousek, M.; Lenzmann, F.; Shklover, V.; Grätzel, M. Nanocrystalline Titanium Oxide Electrodes for Photovoltaic Applications. *J. Am. Ceram. Soc.* **1997,** *80* *14* (12), 3157-3171.

90. Pal, D.; Chakraborty, A. K.; Sen, S.; Sen, S. K. The synthesis, characterization and sintering of sol-gel derived cordierite ceramics for electronic applications. *Journal of materias science* **1996,** *31*, 3995-4005.

91. Anderson, M.; Gieselmann, M.; Xu, Q. Titania and alumina ceramic membranes. *Journal of Membrane Science* **1988,** *39*, 243-258.

92. Boschloo, G.; Fitzmaurice, D. Spectroelectrochemical Investigation of Surface States in Nanostructured TiO2 Electrodes. *The Journal of Physical Chemistry B* **1999,** *103* (12), 2228-2231.

93. Nazeeruddin, M. K.; Di Censo, D.; Humphry-Baker, R.; Gratzel, M. Highly selective and reversible optical, colorimetric, and electrochemical detection of mercury(II) by amphiphilic ruthenium complexes anchored onto mesoporous oxide films. *Advanced Functional Materials* **2006,** *16* (2), 189-194.

94. Bancroft, E. E.; Sidwell, J. S.; Blount, H. N. Derivative Linear Sweep and Derivative Cyclic Voltabsorptometry. *Analytical Chemistry* **1981,** *53* (9), 1390-1394.

95. Alpatova, N.; Rotenberg, Z.; Ovsyannikova, E.; Topolev, V.; Grosheva, M.; Kirchmeyer, S.; Jonas, F. Poly(3,4-ethylenedioxythiophene) Heterogeneity: A Differential Cyclic Voltabsorptometry Study. *Russian Journal of Electrochemistry* **2004,** *40* (9), 917-923.

96. Huang, L.; Wen, T.; Gopalan, A. Electrochemical and spectroelectrochemical monitoring of supercapacitance and electrochromic properties of hydrous ruthenium oxide embedded poly(3,4-ethylenedioxythiophene)-poly(styrenesulfonic acid) composite. **2006**, 51(17):3469-3476. *Electrochimica Acta* **2006,** *51* (17), 3469-3476.

97. Barnes, P.; Anderson, A. Y.; Koops, S. E.; Durrant, J. R.; O'Regan, B. C. Electron Injection Efficiency and Diffusion Length in Dye-Sensitised Solar Cells Derived from Incident Photon Conversion Efficiency Measurements (vol 113, pg 1126, 2009). *The journal of physical chemistry. C* **2009,** *113* (28), 12615.

98. Barnes, P. R. F.; Anderson, A. Y.; Juozapavicius, M.; Liu, L.; Li, X.; Palomares, E.; Forneli, A.; O'Regan, B. C. Factors controlling charge recombination under dark and light conditions in dye sensitised solar cells. *Phys. Chem. Chem. Phys.* **2011,** *13* (8), 3547-3558.

99. Barnes P. Interpretation of optoelectronic transient and charge extraction measurements in dye sensitised solar cells. *J. Phys. Chem. C*, in press.

100. Esteban-Gomez, D.; Fabbrizzi, L.; Licchelli, M. Why, on Interaction of Urea-Based Receptors with Fluoride, Beautiful Colors Develop. *J. Org. Chem.* **2005,** *70* (10), 5717-5720.

101. Nishizawa, S.; Kato, R.; Hayashita, T.; Teramae, N. Anion Sensing by a Thiourea Based Chromoionophore via Hydrogen Bonding. *Anal. Sci.* **1998,** *14*, 595-597.

102. Jones, D. A. Why are so many food plants cyanogenic? *Phytochemistry* **1998,** *47* (2), 155-162.

103. Rubo, A.; Kellens, R.; Reddy, J.; Steier, N.; Hasenpusch, W. Alkali Metal Cyanides. In *Ullmann's Encyclopedia of Industrial Chemistry*, Wiley-VCH Verlag GmbH & Co. KGaA: 2000.

104. Tomasulo, M.; Sortino, S.; White, A.; Raymo, F. Chromogenic Oxazines for Cyanide Detection. *J. Org. Chem.* **2006,** *71* (10), 744-753.

105. *http://www. dartmouth. edu/~rpsmith/cyanide. jpg*

106. *http://www. epa. gov/safewater/contaminants/index. html#mcls*

107. Snowden, T. S.; Anslyn, E. V. Anion recognition: synthetic receptors for anions and their application in sensors. *Current Opinion in Chemical Biology* **1999,** *3* (10), 740-746.

108. Gimeno, N.; Li, X.; Durrant, J. R.; Vilar, R. Cyanide sensing with organic dyes: Studies in solution and on nanostructured Al2O3 surfaces. *Chemistry-A European Journal* **2008,** *14* (10), 3006-3012.

109. McNamee, C. E.; Tsujii, Y.; Matsumoto, M. Physicochemical Characterization of an Anatase TiO2 Surface and the Adsorption of a Nonionic Surfactant: An Atomic Force Microscopy Study. *Langmuir* **2005,** *21* (24), 11283-11288.

110. Omura, N.; Hotta, Y.; Sato, K.; Kinemuchi, Y.; Kume, S.; Watari, K. Fabrication of Stable Al2O3 Slurries and Dense Green Bodies Using Wet Jet Milling. *J. Am. Ceram. Soc.* **2006,** *89* (9), 2738-2743.

111. Amendola, V.; Esteban-Gomez, D.; Fabbrizzi, L.; Licchelli, M. What Anions Do to N-H-Containing Receptors. *Acc. Chem. Res.* **2006,** *39* (10), 343-353.

112. Miura, K. Neurotoxic mechanisms of methylmercury. *Japanese Journal of Toxicology and Environmental Health* **1998,** *44* (6), 393-412.

113. Sanfeliu, C.; Sebastia, J.; Cristofol, R.; Rodriguez-Farre, E. Neurotoxicity of organomercurial compounds. *Neurotoxicity Research* **2003,** *5* (4), 283.

114. Cheung, S. M.; han, W. H. Hg2+ sensing in aqueous solutions: an intramolecular charge transfer emission quenching fluorescent chemosensors. *Tetrahedron* **2006,** *62*, 8379-8383.

115. Zhang, X. B.; Guo, C. C.; Li, Z. Z.; Shen, G. L.; Yu, R. Q. An optical fiber chemical sensor for mercury ions based on a porphyrin dimer. *Analytical Chemistry* **2002,** *74* (4), 821-825.

116. Feng, X.; Fryxell, G.; Wang, L.; Kim, A.; Liu, J.; Kemner, K. Functionalized Monolayers on Ordered Mesoporous Supports. *Science* **1997,** *276*, 923-926.

117. Senel, S.; Kara, A.; Karabakan, A.; Denizli, A. Alanine Containing Porous Beads for Mercury Removal from Artificial Solutions. *Journal of Applied Polymer Science* **2006,** *100* (2), 1222-1228.

118. Lockwood, R.; Chen, K. Adsorption of mercury(II) by hydrous manganese oxides. *Environmental science & technology* **1973,** *7* (11), 1028-1034.

119. Ou, S.; Gao, K.; Li, Y. An in Vitro Study of Wheat Bran Binding Capacity for Hg, Cd, and Pb. *Journal of agricultural and food chemistry* **1999,** *47* (11), 4714-4717.

120. Marchant, W. Modified cellulose adsorbent for removal of mercury from aqueous solutions. *Environmental science & technology* **1974,** *8* (12), 993-996.

121. Skubal, L.; Meshkov, N. Reduction and removal of mercury from water using arginine-modified TiO2. *Journal of Photochemistry and Photobiology A: Chemistry* **2002,** *148* (211), 214.

122. Lahoutifard, N.; Poissant, L.; Scott, S. Heterogeneous scavenging of atmospheric mercury by snow spiked with hydrogen peroxide. *J. Phys. IV France* **2003,** *107* (711), 714.

123. Vitolo, S.; Seggiani, M. Mercury removal from geothermal exhaust gas by sulfur-impregnated and virgin activated carbons. *Geothermics* **2002,** *31* (431), 442.

124. Saricaa, J.; Amyotb, M.; Harea, L.; Blanchfieldc, P.; Bodalyc, R.; Hintelmannd, H.; Lucotte, M. Mercury transfer from fish carcasses to scavengers in boreal lakes: the use of stable isotopes of mercury. *Environmental Pollution* **2005,** *134*, 13-22.

125. *http://www. epa. gov/safewater/mcl. html#inorganic*

126. Llobet, J.; Falco, G.; Casas, C.; Teixido, A.; Domingo, J. Concentrations of Arsenic, Cadmium, Mercury, and Lead in Common Foods and Estimated Daily Intake by Children, Adolescents, Adults, and Seniors of Catalonia, Spain. *Journal of agricultural and food chemistry* **2003,** *51* (3), 838-842.

127. Wang, Q.; Zakeeruddin, S. M.; Nazeeruddin, M. K.; Humphry-Baker, R.; Gratzel, M. Molecular wiring of nanocrystals: NCS-Enhanced cross-surface charge transfer in self-assembled Ru-complex monolayer on mesoscopic oxide films. *Journal of the American Chemical Society* **2006,** *128* (13), 4446-4452.

128. Trammell, S. A.; Meyer, T. J. Diffusional Mediation of Surface Electron Transfer on TiO_2 . *J. Phys. Chem. B,* **1999,** *103*, 104-107.

129. Fillinger, A.; Parkinson, B. A. The Adsorption Behavior of a Ruthenium-Based Sensitizing Dye to Nanocrystalline TiO2 Coverage Effects on the External and Internal Sensitization Quantum Yields. *Journal of the Electrochemical Society* **1999,** *146* (12), 4559-4564.

130. Fattori, A.; Peter, L. M.; Wang, H.; Miura, H.; Marken, F. Fast Hole Surface Conduction Observed for Indoline Sensitizer Dyes Immobilized at Fluorine-Doped Tin Oxide-TiO2 Surfaces. *J. Phys. Chem. C* **2010,** *114* (27), 11822-11828.

131. Bard, A.; Faulkner, L. *Electrochemical methods, fundamentals and applications.;* 2nd ed.; Wiley.: 2001.

132. Karthikeyan, C.; Wietasch, H.; Thelakkat, M. Highly Efficient Solid-State Dye-Sensitized TiO2 Solar Cells Using Donor-Antenna Dyes Capable of Multistep Charge-Transfer Cascades. *Adv. Mater.* **2007,** *19*, 1091-1095.

133. Haque, S. A.; Handa, S.; Peter, K.; Palomares, E.; Thelakkat, M.; Durrant, J. R. Supermolecular Control of Charge Transfer in Dye-Sensitized Nanocrystalline TiO2 Films: Towards a Quantitative Structure–Function Relationship. *Angew. Chem. Int. Ed.* **2005,** *44*, 5740-5744.

134. Handa, S.; Wietasch, H.; Thelakkat, M.; Durrant, J. R.; Haque, S. A. Reducing charge recombination losses in solid state dye sensitized solar cells: the use of donor–acceptor sensitizer dyes. *Chem. Commun.* **2007,** 1725-1727.

135. Ana, e. a. Unusually Slow Regeneration Dynamics on a Highly Efficient Dye-Sensitized Solar Cell. *Chem. Comm* **2008**.

136. Laviron, E. General expression of the linear potential sweep voltammogram in the case of diffusionless electrochemical systems. *J. Electroanal. Chem.* **1979,** (101), 19-28.

137. He, J. B.; Wang, Y.; Deng, N.; Zha, Z. G.; Lin, X. Q. Cyclic voltammograms obtained from the optical signals: Study of the successive electro-oxidations of rutin. *Electrochimica Acta* **2007,** *52* (24), 6665-6672.

138. Nekrasov, A. A.; Ivanov, V. E.; Gribkova, O. L.; Vannikov, A. Voltabsorptometric study of "structural memory" effects in polyaniline. *Electrochimica Acta* **2005,** *50* (7-8), 1605-1613.

139. Nekrasov, A. A.; Ivanov, V. F.; Vannikov, A. V. A comparative voltabsorptometric study of polyaniline films prepared by different methods. *Electrochimica Acta* **2001,** *46* (20-21), 3301-3307.

140. Huang, L. M.; Wen, T. C.; Gopalan, A. Electrochemical and spectroelectrochemical monitoring of supercapacitance and electrochromic properties of hydrous ruthenium oxide embedded poly(3,4-ethylenedioxythiophene)-poly(styrenesulfonic acid) composite. *Electrochimica Acta* **2006,** *51* (17), 3469-3476.

141. Szkurlat, A.; Palys, B.; Mieczkowski, J.; Skompska, M. Electrosynthesis and spectroelectrochemical characterization of poly(3,4-dimethoxythiophene), poly(3,4-dipropyloxythiophene) and poly(3,4-dioctyloxythiophene) films. *Electrochim. Acta* **2003,** *48* (24), 3665-3676.

142. Morandeira, A. Unusually slow regeneration dynamics on a highly efficient dye-sensitized solar cell. *Chem. Comm.* **2012**.

143. Nazeeruddin, M.; Zakeeruddin, S. M.; Humphry-Baker, R.; Jirousek, M.; Liska, P.; Vlachopoulos, N.; Shklover, V.; Fischer, C. H.; Gr+ñtzel, M. Acid-Base Equilibria of (2,2'-Bipyridyl-4,4'-dicarboxylic acid)ruthenium(II) Complexes and the Effect of Protonation on Charge-Transfer Sensitization of Nanocrystalline Titania. *Inorganic chemistry* **1999,** *38* (26), 6298-6305.

144. Zukalova, M.; Prochazka, J.; Zukal, A.; Yum, J. H.; Kavan, L. Structural parameters controlling the performance of organized mesoporous TiO2 films in dye sensitized solar cells. *Inorganica Chimica Acta* **2008,** *361* (3), 656-662.

145. Moser, J. E.; Noukakis, D.; Bach, U.; Tachibana, Y.; Klug, D.; Durrant, J.; Baker, R.; Gratzel, M. Comment on "Measurement of Ultrafast Photoinduced Electron Transfer from Chemically Anchored Ru-Dye Molecules into Empty Electronic States in a Colloidal Anatase TiO2 Film". *The journal of physical chemistry. B, Condensed matter, materials, surfaces, interfaces & biophysical* **1998,** *102* (18), 3649-3650.

146. Zabri, H.; Gillaizeau, I.; Bignozzi, C.; Caramori, S.; Charlot, M.; Cano-Boquera, J.; Odobel, F. Synthesis and comprehensive characterizations of new cis-RuL2X2 (X = Cl, CN, and NCS) sensitizers for nanocrystalline TiO2 solar cell using bis-phosphonated bipyridine ligands (L). *Inorganic chemistry* **2003,** *42* (21), 6655-6666.

147. Leng, W. H.; Barnes, P. R. F.; Juozapavicius, M.; O'Regan, B.; Durrant, J. R. Diffusion Length in Mesoporous Nanocrystalline TiO_2 Photoelectrodes during Water Oxidation. *J. Phys. Chem. Lett.* **2010,** *1* (6), 967-972.

148. Kroeze, J. E.; Hirata, N.; Koops, S.; Nazeeruddin, M.; Schmidt-Mende, L.; Gratzel, M.; Durrant, J. R. Alkyl Chain Barriers for Kinetic Optimization in Dye-Sensitized Solar Cells. *Journal of the American Chemical Society* **2006,** *128* (50), 16376-16383.

149. Handa, S.; Wietasch, H.; Thelakkat, M.; Durrant, J. R.; Haque, S. A. Reducing charge recombination losses in solid state dye sensitized solar cells: the use of donor-acceptor sensitizer dyes. *Chemical Communications* **2007,** (17), 1725-1727.

150. Rao, C. N. R.; Bhat, S. N.; Dwedi, P. C. Spectroscopy of electron donor-acceptor systems. *Applied Spectroscopy Reviews* **1972,** *5* (1), 1-170.

151. Rao, N. A spectroscopic study of the iodine complexes of donors-pyridines, phenanthrolines, bipyridines and diazines. *Transactions of the Faraday Society* **1990,** *46A* (7), 1107.

152. Kebede, Z.; Lindquist, S. E. Donor-acceptor interaction between non-aqueous solvents and I_2 to generate I_3^-, and its implication in dye sensitized solar cells. *Solar energy materials and solar cells* **1999,** *57* (3), 259-275.

153. Yarwood, J.; Person, W. B. Far-infrared intensity studies of iodine complexes. *Journal of the American Chemical Society* **1968,** *90*, 594-600.

154. Klaeboe, P. The Raman spectra of some iodine, bromine, and iodine monochloride charge-transfer coomplexes in solution. *Journal of the American Chemical Society* **1967,** *89*, 3667-3676.

155. Kebede, Z.; Lindquist, S. E. The obstructed diffusion of the I3- ion in mesoscopic TiO2 membranes. *Solar energy materials and solar cells* **1998,** *51* (3-4), 291-303.

156. Anderson, A. Y.; Barnes, P. R. F.; Durrant, J. R.; O'Regan, B. C. Quantifying Regeneration in Dye-Sensitized Solar Cells. *The Journal of Physical Chemistry C* **2011,** *115* (5), 2439-2447.

157. Popov, A. I.; Swensen, R. F. Studies on the Chemistry of Halogens and of Polyhalides. V. Spectrophotometric Study of Polyhalogen Complexes in Acetonitrile and in Ethylene Dichloride. *Journal of the American Chemical Society* **1955,** *77* (14), 3724-3726.

158. Nour, E. M. Spectroscopic studies of the reaction of iodine with the mixed oxygen--nitrogen cyclic base 1,4,10,13-tetraoxa-7,16-diazacyclooctadecane. *Spectrochimica Acta Part A: Molecular Spectroscopy* **1991,** *47* (6), 743-747.

159. Pelet, S.; Moser, J. E.; Gratzel, M. Cooperative Effect of Adsorbed Cations and Iodide on the Interception of Back Electron Transfer in the Dye Sensitization of Nanocrystalline TiO2. *The Journal of Physical Chemistry B* **2000,** *104* (8), 1791-1795.

160. Haque, S. A.; Palomares, E.; Cho, B. M.; Green, A. N. M.; Hirata, N.; Klug, D. R.; Durrant, J. R. Charge separation versus recombination in dye-sensitized nanocrystalline solar cells: the minimization of kinetic redundancy. *Journal of the American Chemical Society* **2005,** *127* (10), 3456-3462.

161. Mueller, R.; Kammler, H. K.; Wegner, K.; Pratsinis, S. E. OH Surface Density of SiO2 and TiO2 by Thermogravimetric Analysis. *Langmuir* **2002,** *19* (1), 160-165.

162. Jackson, S. D.; Hargreaves, S. J. *Metal oxide catalysis;* WILEY-VCH: 2009; Vol. 2.

163. Lu, G. Q.; Zhao, X. S. *Nanoporous Materials Science and Engineering;* Imperial College Press: London, 2004; Vol. 4.

164. Hassel, O.; Hope, H. Structure of the solid compound formed by addition of two molecules of iodine to one molecule of pyridine. *Acta Chem. Scand.* **1961,** *15*, 407-416.

165. Ma, S.; Wu, G. Surface enhanced Raman study of the pyridine-iodine charge transfer complex on the silver electrode. *Transactions of the Faraday Society* **1995,** *372* (2-3), 127-130.

166. Plahte, E.; Grundnes, J.; Klaeboe, P. Spectroscopic studies of charge transfer complexes. XIV. Ethyl Isothiocyanate and Allyl Isothiocyanate with Iodine. *Acta Chem. Scand.* **1965,** *19*, 1897-1905.

167. Greijer, H.; Lindgren, J.; Hagfeldt, A. Resonance Raman Scattering of a Dye-Sensitized Solar Cell: Mechanism of Thiocyanato Ligand Exchange. *The Journal of Physical Chemistry B* **2001,** *105* (27), 6314-6320.

168. Orszagh, I.; Bazsa, G.; Beck, M. T. Spectrophotometric study of the reversible iodine-thiocyanate interaction. *Inorganica Chimica Acta* **1972,** *6*, 271-274.

169. Splan, K. S.; Massari, A. M.; Hupp, J. T. A Porous Multilayer Dye-Based Photoelectrochemical Cell That Unexpectedly Runs in Reverse. *The journal of physical chemistry. B* **2004,** *108*, 4111-4115.

170. O'Regan, B.; Walley, K.; Juozapavicius, M.; Anderson, A. Y.; Matar, F.; Ghaddar, T. H.; Zakeeruddin, S. M.; Klein, C.; Durrant, J. R. Structure/Function Relationships in Dyes for Solar Energy Conversion: A Two-Atom Change in Dye Structure and the Mechanism for Its Effect on Cell Voltage. *Journal of the American Chemical Society* **2009,** *131* (10), 3541-3548.

171. Zhang, M.; Liu, J.; Wang, Y.; Zhou, D.; Wang, P. Redox couple related influences of ð-conjugation extension in organic dye-sensitized mesoscopic solar cells. *Chem. Sci.* **2011,** (2), 1401-1406.

172. Barnes, P.; Liu, L.; Li, X.; Anderson, A. Y.; Kisserwan, H.; Ghaddar, T. H.; Durrant, J. R.; O'Regan, B. Re-evaluation of Recombination Losses in Dye-Sensitized Cells: The Failure of Dynamic Relaxation Methods to Correctly Predict Diffusion Length in Nanoporous Photoelectrodes. *Nano Letters* **2009,** *9* (10), 3532-3538.

173. Reynal, A.; Forneli, A.; Martinez-Ferrero, E.; Sa´nchez-Dý´az, A.; Vidal-Ferran, A.; O'Regan, B.; Palomares, E. Interfacial Charge Recombination Between e^--TiO_2 and the I^-/I_3^- Electrolyte in Ruthenium Heteroleptic Complexes: Dye Molecular Structure-Open Circuit Voltage Relationship. *Journal of the American Chemical Society* **2008,** *130* (41), 13558-13567.

174. Liu, Y.; Jennings, J. R.; Huang, Y.; Wang, Q.; Zakeeruddin, S. M.; Gratzel, M. Cobalt Redox Mediators for Ruthenium-Based Dye-Sensitized Solar Cells: A Combined Impedance Spectroscopy and Near-IR Transmittance Study. *The Journal of Physical Chemistry C* **2011,** *115* (38), 18847-18855.

175. Lang, R. P. Molecular Complexes and their Spectra. XV. Iodine Complexes with Thiophene, 2-Methylfuran and N-Methylpyrrole. *Journal of the American Chemical Society* **1962,** *84* (23), 4438-4441.

176. Hirschmann, R. P.; Kniseley, R. N.; Fassel, V. A. The infrared spectra of alkyl thiocyanates. *Spectrochimica Acta* **1964,** *20* (5), 809-817.

177. Cao, Y. M.; Bai, Y.; Yu, Q. J.; Cheng, Y. M.; Liu, S.; Shi, D.; Gao, F. F.; Wang, P. Dye-Sensitized Solar Cells with a High Absorptivity Ruthenium Sensitizer Featuring a 2-(Hexylthio)thiophene Conjugated Bipyridine. *The Journal of Physical Chemistry C* **2009,** *113* (15), 6290-6297.

178. Dai, F.; Wu, W.; Wang, Q.; Tian, H.; Wong, W. Heteroleptic ruthenium complexes containing uncommon 5,5[prime or minute]-disubstituted-2,2[prime or minute]-bipyridine chromophores for dye-sensitized solar cells. *Dalton Trans.* **2011,** *40* (10), 2314-2323.

179. Bessho, T.; Yoneda, E.; Yum, J.; Guglielmi, M.; Tavernelli, I.; Imai, H.; Rothlisberger, U.; Nazeeruddin, M. K.; Gratzel, M. New Paradigm in Molecular Engineering of Sensitizers for Solar Cell Applications. *Journal of the American Chemical Society* **2009,** *131* (16), 5930-5934.

180. Wu, K.; Hsu, H.; Chen, K.; Chi, Y.; Chung, M.; Liu, W.; Chou, P. Development of thiocyanate-free, charge-neutral Ru(ii) sensitizers for dye-sensitized solar cells. *Chemical Communications* **2010,** *46* (28), 5124-5126.

181. Feldt, S. M.; Gibson, E. A.; Gabrielsson, E.; Sun, L.; Boschloo, G.; Hagfeldt, A. Design of Organic Dyes and Cobalt Polypyridine Redox Mediators for High-Efficiency Dye-Sensitized Solar Cells. *Journal of the American Chemical Society* **2010,** *132* (46), 16714-16724.

182. Zhou, D.; Yu, Q.; Cai, N.; Bai, Y.; Wang, Y.; Wang, P. Efficient organic dye-sensitized thin-film solar cells based on the tris(1,10-phenanthroline)cobalt(II/III) redox shuttle. *Energy Environ. Sci.* **2011,** *4* (6), 2030-2034.

183. Daeneke, T.; Kwon, T. H.; Holmes, A. B.; Duffy, N. W.; Bach, U.; Spiccia, L. High-efficiency dye-sensitized solar cells with ferrocene-based electrolytes. *Nat. Chem.* **2011,** *3* (3), 213-217.